Universidade Estadual de Campinas
Instituto de Física Gleb Wataghin

Murilo Barbosa Alves

Linear optics and coupling corrections applied to Sirius commissioning

Correções de ótica linear e acoplamento aplicadas ao comissionamento do Sirius

Campinas

2021

Murilo Barbosa Alves

Linear optics and coupling corrections applied to Sirius commissioning

Dissertação apresentada ao Instituto de Física "Gleb Wataghin" (IFGW) da Universidade Estadual de Campinas (UNICAMP) como parte dos requisitos exigidos para a obtenção do título de Mestre em Física, na área de Física.

Dissertation submitted to the "Gleb Wataghin" Institute of Physics (IFGW) in the University of Campinas (UNICAMP) in partial fulfillment of the requirements for the degree of Master in Physics, in the area of Physics.

Supervisor/Orientador: Prof. Dr. Antonio Rubens Britto de Castro

Este exemplar corresponde à versão final da dissertação defendida pelo aluno Murilo Barbosa Alves, e orientada pelo Prof. Dr. Antonio Rubens Britto de Castro

Campinas

2021

Ficha catalográfica
Universidade Estadual de Campinas
Biblioteca do Instituto de Física Gleb Wataghin
Lucimeire de Oliveira Silva da Rocha - CRB 8/9174

Alves, Murilo Barbosa, 1996-
AL87L Linear optics and coupling corrections applied to Sirius commissioning / Murilo Barbosa Alves. – Campinas, SP : [s.n.], 2021.

Orientador: Antonio Rubens Britto de Castro.
Dissertação (mestrado) – Universidade Estadual de Campinas, Instituto de Física Gleb Wataghin.

1. Projeto Sirius. 2. Fonte de luz síncrotron. 3. Método de ótica linear por órbitas fechadas. 4. Comissionamento. 5. Ótica linear. 6. Acoplamento bétatron. I. Castro, Antonio Rubens Britto de, 1940-. II. Universidade Estadual de Campinas. Instituto de Física Gleb Wataghin. III. Título.

Informações para Biblioteca Digital

Título em outro idioma: Correções de ótica linear e acoplamento aplicadas ao comissionamento do Sirius
Palavras-chave em inglês:
Sirius Project
Synchrotron light source
Linear optics from closed orbits method
Commissioning
Linear optics
Betatron coupling
Área de concentração: Física
Titulação: Mestre em Física
Banca examinadora:
Antonio Rubens Britto de Castro [Orientador]
Tiago Fiorini da Silva
Júlio Criginski Cezar
Data de defesa: 05-03-2021
Programa de Pós-Graduação: Física

Identificação e informações acadêmicas do(a) aluno(a)
- ORCID do autor: https://orcid.org/0000-0003-4356-8248
- Currículo Lattes do autor: http://lattes.cnpq.br/4778579260807817

MEMBROS DA COMISSÃO JULGADORA DA DISSERTAÇÃO DE MESTRADO DE **MURILO BARBOSA ALVES** RA: **230336** APRESENTADA E APROVADA AO INSTITUTO DE FÍSICA “GLEB WATAGHIN”, DA UNIVERSIDADE ESTADUAL DE CAMPINAS, EM 05/03/2021.

COMISSÃO JULGADORA:

- Prof. Dr. Antonio Rubens Britto de Castro - (Presidente) - IFGW/UNICAMP
- Prof. Dr. Tiago Fiorini da Silva – IF/USP
- Prof. Dr. Júlio Criginski Cezar - LNLS/CNPEM

A Ata de Defesa, assinada pelos membros da Comissão Examinadora, consta no processo de vida acadêmica do aluno.

CAMPINAS
2021

Agradecimentos

Agradeço e dedico este trabalho aos meus pais, Elaine e Luciano, que sempre acreditaram em mim em todas etapas da minha vida e sempre fizeram de tudo para que nunca me faltasse nada. Agradeço à minha irmã Mirela pela curiosidade e interesse nas suas perguntas e pela amizade que estamos desenvolvendo ao longo dos anos.

Agradeço ao Grupo de Física de Aceleradores do LNLS por todo suporte. Fundamentalmente tudo que sei nesta área, aprendi com vocês. Tenho muito orgulho e sou grato por compartilhar dias e noites de muito trabalho, discussões e cafés com vocês.

Agradeço à Liu por todas as oportunidades, sobretudo a de trabalhar com este tema, e também por sempre estar aberta a discussões e a compartilhar seu conhecimento e experiência. Agradeço ao Fernando por ser um grande companheiro de trabalho desde o início, com sua didática e empolgação para conversar sobre tudo, especialmente ciência. Agradeço ao Ximenes pelas discussões, companhia nas aulas e pela ajuda na organização dos códigos no ínicio das implementações. Agradeço à Ana pela ajuda e atenção, além de suas excelentes interfaces gráficas que muito facilitam a operação e estudos de máquina no Sirius.

Agradeço ao Prof. Rubens por ter aceitado ser meu orientador, pelo incentivo e sugestões ao longo do trabalho.

Agradeço à Ana Clara por todo companheirismo e amor de todos esses anos. Desde a época dos vestibulares até à pós-graduação, você sempre esteve comigo em cada momento e os fez muito mais felizes. Sua companhia alegra e torna essa jornada mais leve.

Agradeço ao programa de pós-graduação do IFGW/UNICAMP, aos professores e funcionários que realizam seus trabalhos de forma competente e exemplar, contribuindo enormemente para o desenvolvimento da Física no Brasil.

Finalmente, agradeço ao LNLS/CNPEM e aos seus membros, por toda infraestrutura disponibilizada e todo trabalho coletivo de alto nível que resultou no Sirius, o maior complexo científico brasileiro que possibilitou a existência deste mestrado.

Resumo

Sirius é a nova fonte de luz síncrotron de 4ª geração e baixa emitância do Laboratório Nacional de Luz Síncrotron (LNLS), onde elétrons de 3 GeV são mantidos em condições estáveis, em ultra-alto vácuo ao longo de um anel de armazenamento de 518 m de circunferência sob a ação de campos eletromagnéticos. A matriz resposta de órbita devido a variações de campos dipolares localizados pode ser usada para ajustar a ótica linear e termos de acoplamento bétatron de uma rede magnética a partir de um modelo, usando o método chamado Linear Optics from Closed Orbits (LOCO). Neste trabalho, o método LOCO foi estudado e implementado no anel de armazenamento do Sirius, a fim de calibrar e corrigir ótica linear e acoplamento durante o comissionamento. Vários testes foram realizados com o código implementado usando dados simulados e medidos, obtendo resultados que verificaram a robustez do método. A escolha do algoritmo de minimização e a inclusão de vínculos nas variações de gradientes nos quadrupolos foram fatores importantes para a aplicação do método no Sirius. Os ajustes LOCO foram aplicados iterativamente no anel de armazenamento, onde foi possível reduzir os erros entre a matriz resposta medida e a matriz nominal para um décimo dos valores iniciais. Medidas independentes foram realizadas a fim de comprovar os efeitos positivos das correções aplicadas: as funções óticas medidas foram melhores ajustadas aos valores nominais, recuperando parcialmente a simetria da máquina, o acoplamento bétatron global foi praticamente eliminado, houve aumentos substanciais de abertura dinâmica horizontal e de eficiência de injeção. Os efeitos dos erros de alinhamento e distorções de órbita na ótica e acoplamento do Sirius foram estudados e verificou-se que estes erros influenciam fortemente o desempenho do anel. Além disso, foi concluído que o nível das correções obtidas neste trabalho está próximo do limite imposto pelas perturbações de ótica geradas pela órbita residual presente no anel de armazenamento do Sirius.

Palavras-chaves: Sirius; LNLS; fonte de luz síncrotron; comissionamento; anel de armazenamento; ótica linear; acoplamento bétatron; matriz resposta de órbita; LOCO; física de aceleradores.

Abstract

Sirius is the new 4^{th} generation low emittance synchrotron light source of Brazilian Synchrotron Light Laboratory (LNLS), where 3 GeV electrons are kept in stable conditions in ultra-high vacuum along a 518 m storage ring under the action of electromagnetic fields. The orbit response matrix due to variations of localized dipolar fields can be used to adjust the linear optics and coupling terms in the magnetic lattice from a model, using the method called Linear Optics from Closed Orbits (LOCO). In this work, LOCO method was studied and implemented in the Sirius storage ring, in order to calibrate and correct linear optics and coupling during commissioning. Several tests were performed with the implemented code using simulated and measured data, obtaining results that verified the method's robustness. The minimization algorithm choice and the inclusion of constraints in gradient variations on quadrupoles were important factors for the method application on Sirius. LOCO fittings were iteratively applied on the storage ring, where it was possible to reduce the errors between the measured response matrix and the nominal matrix to one-tenth of its initial values. Beam-based independent measurements were performed to prove the positive effects of the applied corrections: the measured lattice functions were better adjusted to the nominal values, partially restoring the machine symmetry, the global betatron coupling was practically eliminated, substantial improvements in horizontal dynamic aperture and injection efficiency were obtained. The effects of orbit distortions on Sirius optics and coupling were studied and it was found that these errors strongly influence the storage ring performance. Besides, it was concluded that the level of corrections obtained in this work is close to the limit imposed by the disturbances generated by the residual orbit present in the Sirius storage ring.

Keywords: Sirius; LNLS; synchrotron light source; commissioning; storage ring; linear optics; betatron coupling; orbit response matrix; LOCO; accelerator physics.

List of Figures

List of Tables

Acronyms

4GSR 4^{th} Generation Storage Ring.

APG Accelerator Physics Group.

APU Adjustable Phase Undulator.

BBA Beam-Based Alignment.

BPM Beam Position Monitor.

CNPEM Brazilian Center for Research in Energy and Materials.

GN Gauss-Newton.

ID Insertion Device.

LINAC Linear Accelerator.

LM Levenberg-Marquardt.

LNLS Brazilian Synchrotron Light Laboratory.

LOCO Linear Optics from Closed Orbits.

MBA Multi-Bend-Achromat.

NLK Non-Linear Kicker.

ORM Orbit Response Matrix.

PCA Principal Component Analysis.

RF Radiofrequency.

rms root-mean-square.

SOFB Slow Orbit Feedback System.

std standard deviation.

SVD Singular Value Decomposition.

TbT Turn-by-Turn.

Contents

1 Introduction

The Brazilian Synchrotron Light Laboratory (LNLS) is a National Laboratory, located in Campinas-SP, responsible for the operation of the only synchrotron light source in Latin America. The LNLS was created in 1986 to design and build a synchrotron light source in Brazil. This goal was successfully achieved, resulting in the UVX, a second-generation synchrotron light source designed and built in-house, open to users in 1997. The idealization of LNLS as a National Laboratory represents a mark in the institutional design of scientific research in Brazil, which enabled the construction and the implementation of an open use research facility [5].

Currently, the LNLS is part of Brazilian Center for Research in Energy and Materials (CNPEM), a research and development center that operates under contract with the Brazilian Ministry of Science, Technology and Innovations (MCTI). The CNPEM gathers four open National Laboratories: LNLS, the Brazilian Nanotechnology National Laboratory (LNNano), the Brazilian Biosciences National Laboratory (LNBio), and the Brazilian Biorenewables National Laboratory (LNBR) [6].

After more than 20 years, the UVX experimental hall was completely filled with 17 beamlines that served more than a thousand Brazilian and foreign researchers per year with more than 97% availability [7]. During these years, the community of LNLS users and their scientific demands has grown, and the discussions related to a more competitive machine started about 2008. After years of intense research and development in accelerator technology and engineering, the discussions in LNLS evolved to a well-established project in 2012, a 4^{th} Generation Storage Ring (4GSR) named Sirius. During the Sirius construction, most of the Sirius components were contracted from the local Brazilian industry, with a nationalization index larger than 86% [7].

A new era for synchrotron light sources in Brazil has begun with the transition between the end of UVX operation for user research activities on August 2^{nd}, 2019 and the commissioning of Sirius. Sirius is the most complex scientific infrastructure ever built in Brazil, planned to put the country among the worldwide leadership in the field of synchrotron light sources. This new synchrotron was designed to be the brightest one in its energy class and to accommodate up to 40 beamlines, allowing for new researches in many areas such as material science, nanotechnology, biotechnology and environmental sciences [6]. At the time of this writing, Sirius is the only 4GSR in the southern hemisphere and one of the three 4GSRs in operation in the world[1].

[1] The other two operating 4GSRs are located in Europe: MAX-IV in Lund/Sweden and ESRF-EBS in Grenoble/France

1.1 Dissertation Outline

This work is focused on the studies, measurements and corrections of linear optics and betatron coupling applied during Sirius storage ring commissioning. The content of this dissertation is the following:

- Chapter 1: an introduction to the general concepts related to synchrotron light sources, the Sirius Project, the scientific background and main objectives.
- Chapter 2: the basic accelerator physics theory that is necessary for the development of the work.
- Chapter 3: the theory related to the Linear Optics from Closed Orbits (LOCO) method and the code implementation for Sirius.
- Chapter 4: the application of LOCO method with data obtained in Sirius storage ring during commissioning, presenting and discussing the linear optics and coupling measurements and its corrections.

In this chapter, general concepts and the terminology regarding synchrotron light sources will be introduced in Section 1.2. The main information about the Sirius project will be presented in Section 1.3. The scientific background related to the studies conducted in this work is discussed in Section 1.4 and the goals are exhibited in the final Section 1.5.

1.2 Synchrotron Light Sources

Charged particles at relativistic speeds radiate synchrotron light when accelerated perpendicularly to its direction of motion [8]. Synchrotron light sources are scientific facilities where this effect is ultimately exploited in order to produce light with high brightness and covering a broad energy range, with a spectrum from infrared light up to hard X-rays. The synchrotron light sources are high quality and versatile scientific tools that allow for a great diversity of high resolution experiments in several research areas, such as materials sciences, condensed matter physics, nanotechnology and many others.

Generally a synchrotron light source is composed by three main systems[2]: the injection system, the storage ring and the beamlines. Typically the charged particles used in these facilities are electrons. A brief description of each subsystem can be made:

Injection system: composed by an electron source, a Linear Accelerator (LINAC), a synchrotron, generally called booster, and transport lines connecting the accelera-

[2] Throughout this dissertation the set of the accelerator systems in the synchrotron also may be referred as the “machine”.

tors. The electrons are emitted from an electron gun and accelerated by Radiofrequency (RF) structures along the LINAC. Then the electrons are injected in the first circular accelerator, the booster, where their energy is ramped up to the storage ring's energy[3].

Storage ring: after beam extraction from the booster ring, the ultra-relativistic electrons are injected in the second circular accelerator, the storage ring, where electromagnetic fields are used to confine the electrons in stable closed orbits for many hours inside a vacuum chamber with ultra-high vacuum. In this approximated circular orbits the electrons produce synchrotron light that is supplied to the beamlines.

Beamlines: experimental stations installed tangentially to the storage ring, where the generated synchrotron light is used in a wide variety of scientific studies based on the radiation-matter interactions.

Typical values for the "low" energy obtained in the LINAC are hundreds of MeV and the "high" nominal energy in the storage ring are usually few GeV. The whole injection process occurs with a repetition rate of a few Hz until the storage ring is filled with electrons, reaching the operation current. The injection events might occur only in specific times of the day and in this case the storage ring operates in the so-called decay mode. The injection system may also fill the storage ring more frequently to keep the stored current almost constant during operation, this is called top-up mode.

The quality of the radiation produced in synchrotron light sources can be measured by the quantity called brightness. It is a measure of the radiation intensity, source size and collimation for a given energy and can be defined as [9]:

$$B(\omega) = \frac{F(\omega)}{\Sigma_x \Sigma_{x'} \Sigma_y \Sigma_{y'} \left(\Delta\omega/\omega\right)}. \tag{1.1}$$

The photon frequency ω and the photon energy are related by $E = \hbar\omega$. The photon flux is represented by $F(\omega)$ and it is the number of photons per second. The products $\Sigma_x \Sigma_{x'}$ and $\Sigma_y \Sigma_{y'}$ are the photon beam volumes in the horizontal and vertical phase space, respectively. The frequency bandwidth $\Delta\omega/\omega$ considered in the brightness calculation is typically 0.1%. The photon beam volume in phase space depends both on the photon and the electron distributions. The electron beam volume in phase space is called beam emittance and it is a property derived from the storage ring magnetic lattice.

In order to achieve high brightness for a synchrotron light source, one must increase the photon flux by increasing the electron current and also minimizing the electron beam emittance. Constant advances both in the theoretical and technological aspects have been

[3] In some facilities, the beam is injected from the LINAC directly to the storage ring, where the energy ramp is performed.

made in the accelerator community in the last decades, allowing for tremendous gains in brightness of synchrotron light sources [10, 11].

Such great increments in brightness scales have made it possible to classify the synchrotron light sources in generations. The 1st synchrotron light source generation appeared in the early 1960's as a parasitic effect from the bending magnets in particle colliders. The 2nd generation in the 1980's were dedicated light sources built for the production of synchrotron radiation, generated mainly by bending magnets. The 3th generation light sources in the 1990's were optimized to produce synchrotron radiation with Insertion Devices (IDs) installed in long straight sections in the storage ring [11]. The IDs are arrays of magnetic blocks organized in an alternated manner such that the electron beam follows a transversely undulating path when it passes through the device. The sequence of transverse accelerations induce the electrons to radiate synchrotron light, which may interfere to produce a photon beam with very high intensity and a sharp spectrum, as compared to the light emitted at the dipoles. Depending on the magnetic fields in the ID, the polarization of the emitted radiation can also be varied. The IDs types commonly used in 3th synchrotrons are wigglers and undulators.

In 4GSRs, recent developments in the accelerator field have been applied to reduce the electron beam emittance by orders of magnitude as compared to the previous generation, thus increasing the brightness accordingly. Modern undulators are also used as IDs in the storage ring long straight sections. The beginning of the 4th generation of synchrotron storage rings was marked by the commissioning of MAX-IV in 2015 [12], the first 4GSR implemented. A brief overview about the main ideas applied in 4GSRs will be given in Subsection 1.2.2.

1.2.1 Main Devices in a Storage Ring

Magnetic fields are used to deflect and focus the electron beam in the storage ring. Each type of magnetic field is used for a certain purpose and is created by different types of magnets installed around the ring, which form the so-called magnetic lattice. Typically the magnetic lattice is composed by electromagnets with coils fed by power supplies but it is also possible to use permanent magnets. The main magnets types and their functions are:

Dipoles: bending magnets that create an approximated constant magnetic fields which are used to radially deflect the electrons in curved paths, totalling a 2π rad deflection in one turn and allowing for a closed orbit motion.

Quadrupoles: focusing magnets that provide magnetic fields whose intensity is linearly dependent on the electron transverse deviations. These magnetic fields create a deflection with a strength determined by the deviation from the reference orbit. From

the Lorentz force expression it can be obtained that if a quadrupolar field is focusing in one direction it is necessarily defocusing in the perpendicular direction. Thus, to obtain a net focusing in both directions, an alternated focusing scheme must be used with two types of quadrupoles: focusing and defocusing. The electron dynamics in the presence of dipolar and quadrupolar fields is linear, then the magnetic lattice constituted only by dipoles and quadrupoles is also denominated as a linear lattice.

Sextupoles: electrons with energy deviations from the storage ring nominal energy are differently focused in a linear magnetic lattice. Since the electrons in a beam have an energy distribution, chromatic aberrations effects may disturb the electrons stability. The sextupoles create magnetic fields that depend quadratically on the electron tranverse deviations, therefore it introduces focusing forces that depends on the transverse displacements and allows for the correction of these chromatic aberrations. However, the non-linear fields introduced by the sextupoles also change the beam dynamics to a non-linear regime and the motion of electrons with sufficiently large deviations may be unstable. The largest deviations that still produce a stable motion define a region in the electron phase space called dynamic aperture. Hence, more sextupoles must be included in the lattice in order to increase the stability region, i.e., increase the storage ring dynamic aperture. For the same reason as for the quadrupoles, two types of sextupoles, focusing and defocusing, are needed to correct the chromatic effects in both transverse planes.

Figure 1 shows a schematic representation of the magnet blocks and the corresponding field lines for each type of magnet. In these examples, the electron path points inwards the paper (or screen), the radial positive direction is pointing to the left and the vertical positive direction to the upper side. In this way, the exemplified quadrupoles and sextupoles are defined as focusing (it focus the beam in the radial direction) and the corresponding defocusing types are obtained by a $\pi/2\,\mathrm{rad}$ rotation for quadrupoles and $\pi/3\,\mathrm{rad}$ for sextupoles.

The electron beam centroid positions can be measured by devices called Beam Position Monitors (BPMs), installed in the vacuum chamber at many locations around the storage ring. The measurements can be performed in a turn-by-turn basis to access the beam trajectories and also averaging the data over many turns to obtain the information about the beam orbit. A simple scheme for a typical BPM device is shown in Figure 2, where the electron path points outwards the paper.

The electron beam excites electromagnetic signals in the four BPM antennas. The values of these four intensities measured at the antennas can be manipulated to calculate

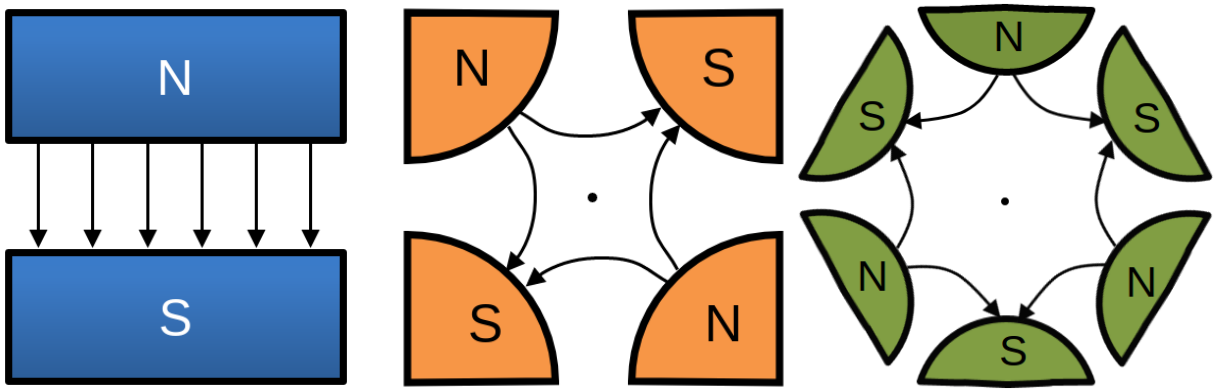

(a) Dipole (b) Quadrupole (c) Sextupole

Figure 1 – Schematic examples of magnets used in storage rings.

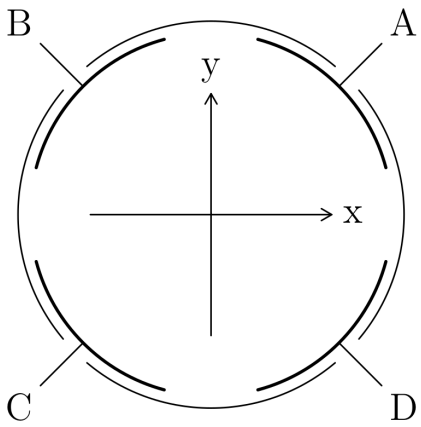

Figure 2 – BPM scheme. The A, B, C, D lines represent the device antennas. Adapted from [1].

the transverse positions for the beam centroid:

$$x = K_x \frac{(A+D)-(B+C)}{\Sigma_{\text{BPM}}} \tag{1.2}$$

$$y = K_y \frac{(A+B)-(C+D)}{\Sigma_{\text{BPM}}}, \tag{1.3}$$

where $\Sigma_{\text{BPM}} = A+B+C+D$ is the sum signal from all BPM antennas and it is directly proportional to the electron beam current. K_x and K_y are calibration factors dependent of BPM geometry and the distances between antennas. This method of calculation is called Δ/Σ and other methods are available [13].

The orbit distortions can be corrected by applying localized dipolar fields, called dipolar kicks, to steer the beam at each turn and then steer the orbit towards a target. Short dipoles, called orbit correctors or simply correctors, are added in the lattice to produce the kicks that steer the orbit. There are two types of corretors: horizontal and vertical. The horizontal correctors create vertical dipolar fields to deflect the beam in the horizontal plane and the vertical correctors produce a horizontal dipolar fields to vertically deflect the beam.

The orbit correction can be performed by measuring the orbit distortions with the BPMs and, based on these measurements, one can calculate and apply in the correctors the corresponding kicks variations that produce an orbit change that minimizes the measured distortion, thus steering the electron beam towards a target orbit.

Since the electrons lose energy by synchrotron radiation emission in every turn around the storage ring, an energy gain process must occur to maintain the electrons in stable motion. Ressonant cavities are used in storage rings to confine oscillating electromagnetic fields with a frequency in the RF range. These devices are called RF cavities and they provide the energy gain to the electrons with longitudinal electric fields. There is a fundamental principle, called phase stability, that ensures the synchronization between the fields oscillation inside the cavity and the circulating periodic motion of the electrons. This fundamental mechanism, that is further discussed on Chapter 2, is the origin for the name "synchrotron".

1.2.2 4^{th} Generation Storage Rings

A magnetic lattice is composed by a sequence of magnets, called unit cells, that are repeated around the storage ring. The unit cells are connected by straight sections, without magnets. These straight sections are used for the installation of IDs. At the ends of each unit cell there are quadrupoles for the optics functions matching in the straight sections.

A new generation of synchrotron light sources emerged from the realization of innovative magnetic lattices where very small emittances can be achieved. These magnetic lattices are named Multi-Bend-Achromat (MBA), where dipoles are interspersed with quadrupoles and sextupoles, forming the arc sections, without much drift spaces between magnets. In the previous generation, the number of dipoles in a unit cell was less than four, being usually Double or Triple-Bend-Achromat lattices. For MBA lattices there are more than four dipoles per unit cell, which explains the term "Multi-Bend". Since the dipoles can be viewed as spectrometers as well, they introduce a dependence of electron position with its energy. The focusing strengths in a MBA lattice are adjusted to locally correct this dispersion effects, allowing for independence on position with energy in the straight sections and this is what the term "Achromat" refers to.

The natural emittance of a storage ring depends on the electron energy and the number of dipoles in the lattice roughly as $\epsilon \propto \gamma^2/N_b^3$. For a fixed circumference, more dipoles in a magnetic lattice implies that the individual bending angles may be reduced, therefore reducing the energy dispersion errors created by these magnets. The equilibrium emittance depends on the dispersion effects at dipoles, so minimizing the dependence on electron position with energy at the bending magnets is one of the key factors to reduce

the natural emittance.

The seemingly simple idea related to the MBA magnetic lattice was proposed in the early 1990's [14] but it took more than 20 years to be implemented in practice due to the related accelerator technology and engineering challenges that needed to be overcome [15]. The technical problems appear in a cascade-effect fashion. Quadrupoles with strong focusing strengths are required in order to locally correct the energy dispersion errors created by several dipoles in a compact arc section. With strong focusing strengths comes large chromatic errors and to correct this geometric aberration, sextupoles with strong fields are needed as well. However, strong sextupoles introduce strong non-linearities in the beam dynamics that spoil the dynamic aperture, thus other strong sextupoles (even octupoles in some cases) must be used to increase the beam stability region. To apply strong magnetic fields in the electron beam, the magnetic poles must be close to the beam, i.e., the magnet gaps must be small. Consequently this limits the vacuum chamber radius. The traditional approaches for local vacuum pumping are not sufficient for such small vacuum chambers, so new approaches must be used such as Non-Evaporable Getter (NEG) [16] coating inside the chambers for distributed vacuum pumping. The beam dynamics in the presence of strong fields is also more sensitive to perturbations, such as field and alignments errors, so the related error tolerances for the devices fabrication, installation and alignment must be very low to guarantee the beam stability.

The aforementioned topics are just a subset of a much larger set of scientific and engineering challenges related to the 4^{th} generation that justifies the time gap between the theoretical proposal and the practical realization of MBA lattices [15, 17]. At the end of 2020, when this dissertation was written, there were only three 4GSRs in operation around the world: MAX-IV in Lund/Sweden [18], Sirius in Campinas/Brazil [19], two greenfield projects, and ESRF-EBS in Grenoble/France [20], an upgrade of a 3^{th} generation synchrotron.

1.3 The Sirius Project

The LNLS is one of the four national laboratories gathered in the CNPEM. The first brazilian synchrotron light source was UVX, a 2^{nd} generation light source with a natural emittance of 100 nm rad at 1.37 GeV, designed and built by LNLS. UVX was inaugurated in 1997 and it was the first synchrotron in the southern hemisphere. With the increase of synchrotron users and new scientific demands in UVX and also with the rise of new generations of light sources, around 2008 LNLS started the studies for a new machine, which after a great amount of development and discussions[4] resulted in Sirius,

[4] For more detailed historical aspects of LNLS and Sirius, the author recommends the references [7, 21, 22].

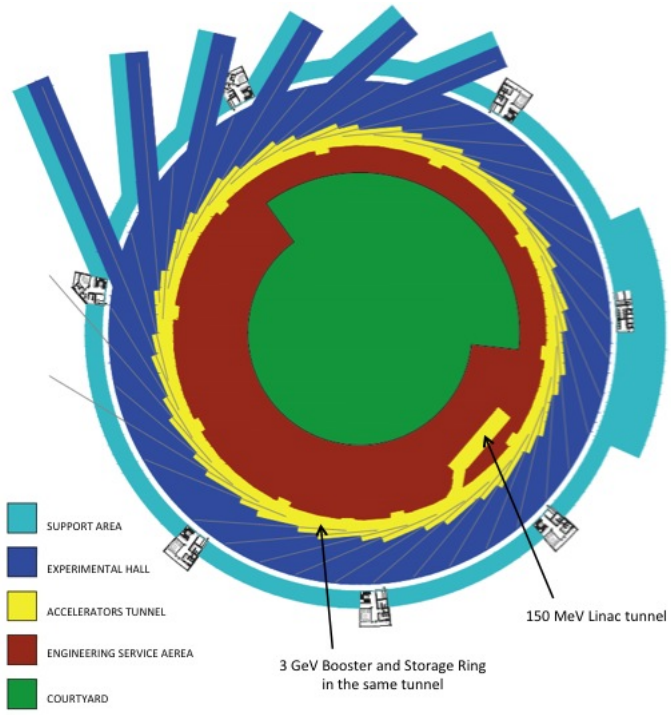

Figure 3 – Sirius building layout [2].

a 4^{th} generation light source [19]. The UVX shutdown occurred in August 2019, while the Sirius commissioning was in progress.

The Sirius facility building layout is schematically shown in Figure 3. The injection system is composed by a 150 MeV LINAC and a full-energy booster ring ramping from 150 MeV to 3 GeV. The injection frequency is 2 Hz and the planned injection mode for Sirius is top-up. The booster shares the same tunnel with the storage ring and it has an emittance of 3.5 nm rad at 3 GeV, which is a low emittance for a booster ring [23] and this is required to optimize the off-axis injection efficiency in the storage ring with a Non-Linear Kicker (NLK) [24]. The Sirius storage ring will be further detailed in the next subsection.

1.3.1 Magnetic Lattice and Basic Parameters

The final design for Sirius magnetic lattice is represented in Figure 4. It is a 5BA lattice with a natural emittance of 0.25 nm rad at 3 GeV for the bare lattice (without IDs). With the installation of the planned IDs, the emittance is expected to be reduced as low as 0.15 nm rad.

The optical lattice functions for one superperiod of the Sirius magnetic lattice are plotted in Figure 5. The small values for the dispersion and betatron functions, especially at the central bending magnet, are fundamental factors to obtain the low emittance in Sirius storage ring. The zero dispersion and the low beta functions in the straight sections,

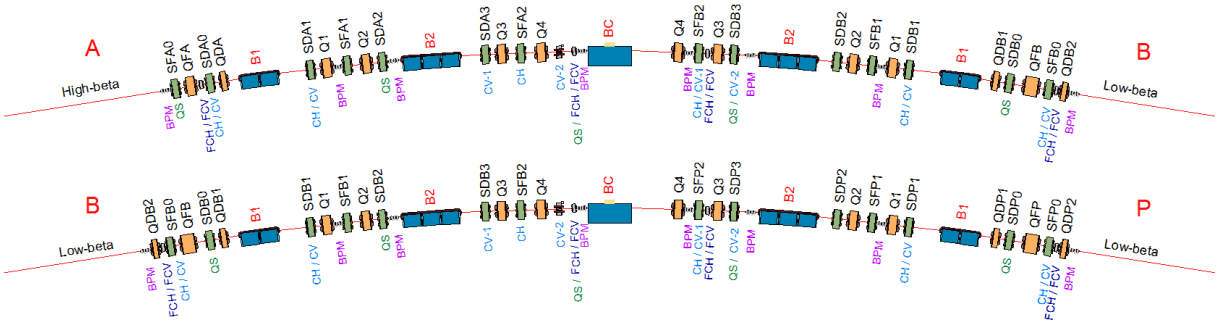

Figure 4 – Sirius 5BA magnetic lattice cells. The magnets are represented by colored blocks. Dipoles (B) are in blue, quadrupoles (Q) in orange and sextupoles (S) in green. The cells are characterized by their straight sections types: high-beta (A) or low-beta (B, P). The Sirius storage ring is composed by 5 super-periods, each one composed by the four cells sequence A-B-P-B [2].

combined with the low emittance, are essential to obtain small beam sizes at beamlines. The zero dispersion also is required to the possibility of emittance reduction after IDs installation.

The Sirius magnetic lattice counts with 20 straight sections, being 5 with high horizontal betatron fuction (A type) and 15 with low horizontal and vertical betatron functions (B and P types). One of the main differentials of Sirius is having that many low-beta straight sections around the storage ring. Regarding the linear lattice elements, the B and P sections are identical and the difference is related to the sextupoles, i.e., second order elements. 17 out of 20 straight sections are available for IDs installation, 2 will be used for machine installations and 1 will be shared between a small ID and machine installation [21].

The central dipole BC is a permanent magnet with a strong peak field of 3.2 T and longitudinal gradient. In the storage ring there are 20 of such superbends providing X-rays with critical energy of 19.2 keV [25] and allowing for additional 20 beamlines. The remaining four dipoles per arc, two B1 and two B2, are electromagnets with peak fields of 0.58 T. The total number of dipoles in the Sirius magnetic lattice is $5 \times 20 = 100$, being 20 permanent magnets (BC) and 80 electromagnets (B1 and B2).

The high-beta straight sections count with a quadrupole doublet (QFA, QDA) for the optics matching. In low-beta straight sections quadrupole triplets are used for the matching (QFB, QDB1, QDB2) for B-type section and other triplet (QFP, QDP1, QDP2) for P-type sections. The quadrupoles in the arc sections are labeled as Q1, Q2, Q3 and Q4. Thus, there are 12 families of quadrupoles in the Sirius magnetic lattice. Notice that the quadrupole and dipole magnets in the arc have a mirror symmetry around the BC magnet. The total number of quadrupoles in Sirius storage ring is 270.

In the Sirius lattice there are 21 families of sextupoles, whose names can be checked

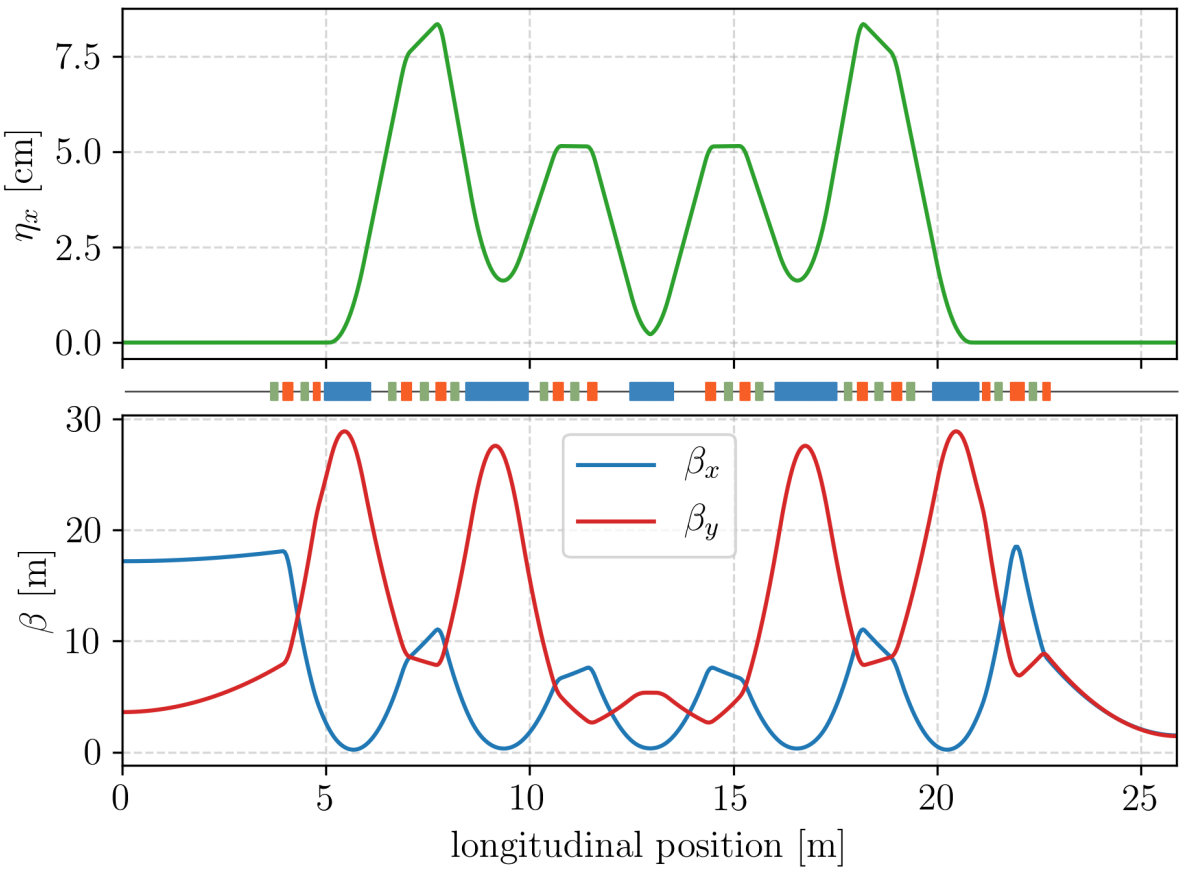

Figure 5 – Lattice functions for one 5BA cell for the Sirius storage ring with a high-beta straight section in the left and a low-beta in the right.

in Figure 4. Sextupoles are used for the correction of chromatic errors and non-linear dynamics optimization. The number of sextupole magnets in Sirius is 280.

For the slow orbit correction system, there are 8 BPMs per arc section, thus totalling $8 \times 20 = 160$ BPMs in the storage ring. There are 6 horizontal correctors (CH) and 7 vertical correctors (CV) per section, both types installed in sextupole magnets. There is also 1 additional vertical corrector magnet installed per arc, then there are $6 \times 20 = 120$ CHs and $(7+1) \times 20 = 160$ CVs in the storage ring. The orbit correction is presently controlled by the in-house implemented system called Slow Orbit Feedback System (SOFB).

For the fast orbit correction system, there are 4 horizontal and 4 vertical fast correctors (FCH and FCV, respectively) per sector, so 80 FCH and 80 FCV in total (there are 2 FCH and 2 FCV per source point). The fast orbit correction will be controlled by the Fast Orbit Feedback (FOFB) system.

The coupling control system counts with 4 skew quadrupoles[5] (QS) per arc that are achieve as additional coils in sextupole magnets and 1 additional QS in one fast corrector per section. Hence, there are $(4+1) \times 20 = 100$ QS in the storage ring. The 80

[5] A skew quadrupole is basically a normal quadrupole rotated by a $\pi/4$ rad angle.

Table 1 – Number of elements for each type in Sirius storage ring.

Element Type	# of Elements
Dipole	100
Quadrupole	270
Sextupole	280
BPM	160
H. Slow Corrector	120
V. Slow Corrector	160
Skew Quadrupole	100
H. Fast Corrector	80
V. Fast Corrector	80

skew quadrupoles in sextupole magnets are already sufficient for coupling control and the remaining 20 QS in the fast correctors are used for the process of Beam-Based Alignment (BBA), where the electron beam is used to measure the center offsets between the BPMs and the quadrupoles, in order to correct the orbit towards the magnets centers as close as possible. The skew quadrupoles in fast correctors are useful for BBA since they are positioned very close to the BPM right next the BC magnet.

Table 1 summarizes the number of elements for each type that are installed in the Sirius storage ring. The main global parameters for the Sirius storage ring can be found in Table 2, where the relevant parameters for each planned operation phase are presented as well. Much more technical information about Sirius can be accessed in the open website [2].

1.3.2 Commissioning

Between the assembly of the synchrotron light source components and the regular operation of the facility there is a gap where a lot of parameters tuning and measurements are made. The final goal is providing the conditions to reliably execute the electron beam journey (from the electron gun at LINAC until the storage ring) and then to push the machine performance and the electron beam properties to meet the design specifications, reaching the ideal operation conditions. This gap is the commissioning[6]. The commissioning also can be divided in stages: commissioning of the sub-systems, machine and beamlines.

The realization of 4GSRs imposes challenges in its commissioning as well. For the reasons discussed in Subsection 1.2.2, a MBA lattice rigorously limits the conditions to store an electron beam. Therefore, studying the commissioning steps beforehand with

[6] Actually, the stages of a synchrotron light source history usually have some overlaps and are not as linear as expected.

Table 2 – Main parameters of the Sirius storage ring. Adapted from [4].

Parameter	Symbol	Operation Phases			Unit
		Commiss.	Phase 1	Phase 2	
Energy	E_0	3.0			GeV
Gamma factor	γ	5871			
Circumference	L_0	518.396			m
Revolution period	T_0	1.729			µs
Revolution frequency	f_0	578			kHz
Harmonic number	h	864			
Momentum compaction	α	$1.636 \cdot 10^{-4}$			
Transverse tunes (H/V)	$\nu_{x/y}$	49.096/14.152			
Energy loss per turn	U_0	471			keV
Natural emittance	ε_0	251			pm rad
Natural energy spread	σ_δ	$8.5 \cdot 10^{-4}$			
Nominal total current	I_0	30	100	350	mA
RF cavity		1 7-Cell	2 SC-RF		
Gap voltage	$\hat{V}_{\mathrm{rf}}$	1.8	3.0		MV
Natural bunch length	σ_z	3.2 (10.7)	2.5 (8.2)		mm (ps)
Synchrotron tune	ν_z	$3.56 \cdot 10^{-3}$	$4.6 \cdot 10^{-3}$		

simulations has become a standard practice at the design stage of 4GSRs [26–30], so the challenges and its solutions can be foreseen.

The author contributed to the Sirius commissioning simulations studies, where simulations for the commissioning procedures with realistic errors were developed and applied both for Sirius booster and storage ring lattice models [31]. The studies results served as guidelines and procedures that were successfully applied on Sirius commissioning to accumulate a 10 mA electron beam at 3 GeV in the Sirius storage ring for the very first time in February 20, 2020. The author had the singular opportunity to participate in the commissioning stages that led to this achievement.

The commissioning phase in which coarse adjustments are made allowing the electron beam to reach its final condition in the storage ring for the first time is often called early commissioning. At this stage, typically the machine performance optimization is not a major concern, since the feasibility of each process is being proven in first place. Therefore, it can be stated that the Sirius early commissioning has ended in February 20, 2020, proving that were no severe conceptual design errors or problems in the machine assembly that made impossible the electron beam accumulation in the storage ring. However, the commissioning after that is not finished yet, since the errors that move away the actual machine performance and beam properties from the expected and designed values are still present and uncorrected at this stage.

In order to optimize the machine performance, a second stage of the commissioning is needed. At this phase, the electron beam is available for measurements. These machine studies have been carried out by the Sirius commissioning team during the 2020 year. At the time of writing the machine commissioning is currently in progress alongside with the commissioning of 6 beamlines, 5 of them using non-definitive Adjustable Phase Undulators (APUs) as the synchrotron radiation source, which were specifically installed in these beamlines for the commissioning stage, and the remaining beamline uses a superbend BC as the light source. Until the end of 2020, the Sirius operation shifts were alternating between machine and beamline commissioning, where for the latter the storage ring was delivering a 40 mA electron beam in decay-mode for the beamlines.

1.4 Scientific Background

The storage ring linear optics is fundamental to determine the electron beam equilibrium distribution, then the beam size and divergence depends directly on the linear optics. It also has an effect on the beam stability. Large deviations in the linear optics compared to the nominal optics move away the beam properties from the design values or, more drastically, these errors might preclude to store an electron beam. Typically, most of the optics errors are found in the first commissioning stages of a new storage ring.

Linear optics errors can be caused by various sources. Strength errors in the quadrupole magnets, horizontal orbit offsets in sextupoles, changing the effective focusing on the beam, gradient errors in dipoles, errors in the magnets excitation curves – the calibration between the current setting in the power supplies and corresponding magnetic fields in the electromagnets. IDs may introduce gradient errors as well. Deviations in linear optics may break the lattice symmetry, which may introduce additional resonances in the beam dynamics, thus increasing the chances of beam loss.

In a basic description of the transverse dynamics for electrons in a storage ring, the horizontal and vertical motions are uncoupled, thus the transverse planes can be regarded as independent. In this case, the theoretical vertical emittance is almost zero. However, roll errors in the dipoles and quadrupoles, vertical orbit offsets in the sextupoles, random skew gradients errors and IDs introduce coupling between the transverse planes. The roll errors may also create a vertical dispersion function, which is nominally zero. Therefore, coupling errors increase the vertical beam size and may have an effect on the injection efficiency, by transferring part of the large horizontal amplitude of the injected beam into the vertical plane.

Even if the errors sources are beforehand minimized as much as possible, with magnets characterization, installation and alignment reaching the specifications, these processes are limited by finite precision and the residual errors may still affect negatively

the electron beam. Since the electron beam in a storage ring is a very sensible probe, beam-based techniques are often used for characterization and optimization. Two approaches can be made: (i) perform beam-based measurements related to the linear optics and coupling, and guided by the accelerator physics theory, one can use the storage ring model to calculate the corrections with the design values as the final target; (ii) consider the storage ring as a black-box, then perform parameters variations with the goal to improve a figure of merit constructed with beam-based data. The approach (i) is often called beam-based corrections and the (ii) beam-based optimization [1].

Each approach has its pros and cons but their final goal is the same: improve the machine performance. The beam-based correction approach has the conceptual advantage that, based on the theory, it tries to increase the real accelerator performance by making it as close as possible to the design accelerator. On the other hand, since this method is model-dependent, i.e., it depends on the correspondence between the storage ring modeling and the real storage ring, if the model fails to accurately describe the reality, the corrections effectiveness is reduced or even worse, the intended corrections are manifested as additional perturbations. The beam-based optimizations have the advantage of being model-independent, however depending on the case, the optimization process might take too much time to converge and it also might be more susceptible to noise and variations in the measured data. Moreover, the final corrections obtained by the optimization must be interpreted and explained afterwards, which may not be a trivial task in general.

Linear Orbit from Closed Orbits (LOCO) is a beam-based correction method implemented by J. Safranek and first applied to the National Synchrotron Light Source (NSLS) storage ring [32–34]. The ideas behind LOCO method were developed in previous works at Stanford Linear Accelerator Center (SLAC) [35, 36]. The main idea of this method is to use the beam orbit response due to localized dipolar fields variations to extract information about the linear optics and coupling in the real machine. This is done by measuring the orbit response with the stored electron beam and then calibrating the model machine to the data, i.e., changing the relevant parameters in the model until the simulated orbit response matches the measured one. After this process, if the model describes reasonably the real storage ring, the actual linear optics and coupling can be derived and its deviations from the nominal values are obtained as well. Furthermore, from the calibrated model it is also possible to calculate the variations for adjustable parameters in the real machine, which allows for the correction of linear optics and coupling errors. In this way, LOCO method can be used both as a diagnostic and a correction tool.

The LOCO code was first implemented in FORTRAN language [37] and this version was used to correct the optics in the NSLS X-ray ring [34] and debug problems in the Advance Light Source (ALS) optics [38]. Several years later, LOCO code was implemented in MATLAB [39, 40] with a graphical user interface and compatible with the Accelerator

Toolbox (AT), an accelerator modelling tool in MATLAB [41].

After that, LOCO has become a tool widely applied in many accelerators around the world. UVX, the first synchrotron light source of LNLS, was amongst these facilities [42]. Other improvements in the method were made, adding options of alternative minimization methods and constraints to the fitting [43]. The author in [37] mentions that, in 2007, after a search for "LOCO" in the text of papers on the Joint Accelerator Conferences website [44], 107 papers were found. The same search made in 2020 yielded 510 results. This illustrates the impact of LOCO method in the accelerator community over the years. LOCO has already been proven to be a useful tool for 4^{th} generation light sources as well, after being applied in MAX-IV first optics studies [45].

The effects of LOCO corrections on the machine can be checked by independent beam-based measurements. It can be verified if the measured orbit response converged to the expected orbit response from the nominal lattice. Changing a quadrupole strength and measuring the corresponding shifts in the betatron tunes is a procedure to determine the beta functions at quadrupoles. The beta function at the BPMs can be determined by applying a fast dipolar impulse to the beam (for example with a pinger) and measuring the Turn-by-Turn (TbT) response in the beam trajectory over time. The dispersion function at BPMs is determined by varying the RF frequency in the cavity and measuring the variation in the beam orbit. Approximating the horizontal and vertical tunes and measuring its minimum distance allows to determine the global betatron coupling. The magnitude of the measured orbit response in one direction due to a dipolar variation in the perpendicular plane provides the information about the coupling distribution along the storage ring. The strength of the fast dipolar impulse can be increased until the electron beam is partially or completely lost, providing information about the dynamic aperture region. If a diagnostic beamline is available, beam emittance measurements can be performed. The injection efficiency in the storage ring is also a good indicative of performance improvement.

1.5 Objectives

The predominant programming language used in Sirius machine control system is Python. After the design studies that resulted in the Sirius lattice and the commissioning simulations, the Sirius models in MATLAB were not satisfactory explored by the LNLS Accelerator Physics Group (APG) in the actual commissioning, mainly due to inconveniences related to the different programming languages. Since there were accelerator modeling and simulations Python frameworks developed in-house and in advanced stages of implementation, the full migration of the Sirius to Python regarding the Accelerator Physics modeling and simulations were performed quite rapidly with only small

adjustments.

Next to this, even though LOCO code is available in MATLAB, the LNLS APG was also seeking for an expertise development related to the method proposed in LOCO for the application on Sirius commissioning and later on the machine studies shifts. Moreover, a code developed in-house is much more flexible to test new ideas and to implement new functionalities. Considering the programming language migration as well, the idea of studying LOCO method and implementing the code in Python came naturally. The author had the opportunity to conduct this task, which derived in this master's work.

The master's main goals can be organized as follows:

- Study the Linear Optics From Closed Orbits (LOCO) method.
- Implement LOCO in Python for the Sirius storage ring model.
- Test the reliability of the implemented code with simulation studies.
- Implement a measurement script for the betatron function by tune shifts.
- Realize linear optics and coupling studies in the Sirius storage ring during the commissioning, performing measurements and corrections using the implemented codes.

To summarize, the dissertation gathers the author's contributions to the Sirius storage ring commissioning regarding the first studies and results related to the linear optics and coupling measurements[7] and corrections.

[7] Some measurement scripts used in the dissertation are results from collective work of the APG, but the reported measurements were performed by the author during the Sirius commissioning.

2 Single Particle Dynamics

This chapter is dedicated to introduce the basic accelerator physics concepts and the terminology required for this dissertation. For detailed discussions about the topics presented here, the author recommends the references [46, 47].

After the storage ring coordinate system definition in Section 2.1, the dynamics of a single electron will be described in Sections 2.2 and 2.3. In Section 2.4, the perturbations on the dynamics, that are fundamental to this work, are presented and discussed.

2.1 Coordinate System

To describe the motion of electrons in a storage ring, a coordinate system definition is required and the concept of reference orbit is necessary. With proper initial conditions, an ideal electron (also called synchronous electron), which has the storage ring nominal energy E_0, follows a closed orbit and this specific periodic path is defined as the reference orbit. The motion of an arbitrary electron is then described in terms of small deviations from the reference orbit, which is taken as the coordinate system origin.

The reference orbit is curved at dipoles and straight elsewhere. Generally, storage rings are planar, i.e., they are designed so that dipoles deflect the electrons in just one direction (called radial or horizontal), therefore the ideal orbit defines an orbital plane in the storage ring. It is convenient to use a curvilinear and comoving coordinate system. The longitudinal axis s can be defined as tangent to the local orbit, the horizontal x is defined in the radial direction and the vertical y is perpendicular to the orbital plane. A graphical representation of this coordinate system can be seen in Figure 6.

Electrons in a storage ring are in the ultra-relativistic regime, where $E \approx pc$ and the major contribution to the total momentum is longitudinal $p = \sqrt{p_s^2 + p_x^2 + p_y^2} \approx p_s$. It is assumed that transverse displacements (x, y) of these electrons to the reference orbit are small, then the ratios p_x/p and p_y/p are small as well and they can be related to geometric quantities, namely angular deviations:

$$x' = \frac{\mathrm{d}x}{\mathrm{d}s} \approx \frac{p_x}{p},$$
$$y' = \frac{\mathrm{d}y}{\mathrm{d}s} \approx \frac{p_y}{p}.$$

The approximations made above are called paraxial. The coordinates (x, x', y, y') define a four dimensional (4D) phase space, where the transverse dynamics is described. Note that the displacements are functions of the longitudinal coordinate s, replacing the

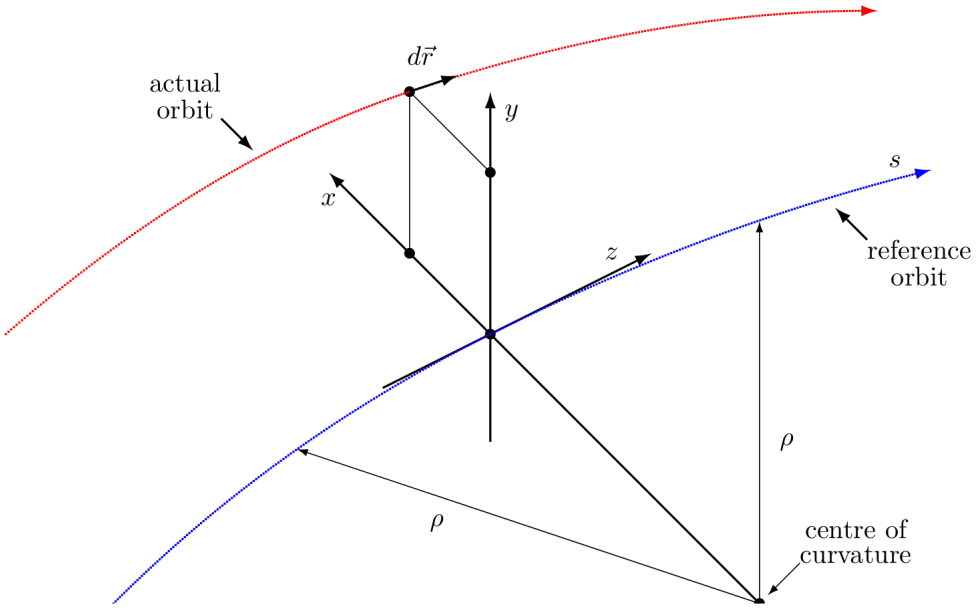

Figure 6 – Coordinate system used in storage rings [3].

time t that is commonly used to describe the dynamics of a system. This substitution is convenient since the s coordinate is periodic for a storage ring and the transverse coordinates derivatives can be interpreted geometrically.

To describe the longitudinal dynamics, one can define two more coordinates. The first is the difference of longitudinal position $s(t)$ of a generic electron relative to the position $s_{\text{sync}}(t)$ of the synchronous electron:

$$z(t) := s_{\text{sync}}(t) - s(t). \tag{2.1}$$

The variable t represents the wall-clock time. The coordinate z can be used in time units as well, represented by τ and the conversion is made by $\tau(t) = z(t)/c$.

For the last coordinate, the electron relative momentum deviation from the nominal momentum is used, which is also typically small:

$$\delta := \frac{p - p_0}{p_0} \approx \frac{E - E_0}{E_0}, \tag{2.2}$$

where the approximation follows from $E \approx pc$.

Finally, $(x, x', y, y', z, \delta)$ defines a six dimensional (6D) phase space where the transverse and longitudinal dynamics of the electrons in a storage ring can be studied.

2.2 Transverse Dynamics

The transverse dynamics describes the motion of the electrons in the 4D phase space (x, x', y, y'). In general, the typical time scale of the longitudinal dynamics is much

larger than the transverse time scale and the two dynamics can be treated independently. This is called the adiabatic approximation and is a good approximation to describe the transverse motion in storage rings. In Sirius storage ring, while it takes around 200 turns for an electron to perform one complete energy oscillation, in just one turn the same electron completes 49 and 14 oscillations in x and y planes, respectively.

2.2.1 Betatron Oscillations

A simpler version of a magnetic lattice is composed by dipoles and quadrupoles only. The dipoles bend the electrons path around the ring and define the ideal orbit. The dipole field can be seen as the zeroth-order expansion of the lattice magnetic fields. The next terms of the expansion are field gradients, mainly related to the quadrupoles. This setup composes the linear magnetic lattice, where the magnetic field expansion is up to first order.

Assuming this linear approximation and that the transverse directions are independent, i.e., there is no transverse coupling terms, the Hamiltonian of an electron in the storage ring is [1]:

$$H \approx \frac{x'^2}{2} + \frac{y'^2}{2} + \Big(K(s) - G^2(s)\Big)\frac{x^2}{2} - K(s)\frac{y^2}{2} - G(s)x\delta. \tag{2.3}$$

$G(s)$ is called curvature function and $K(s)$ is the focusing function, with the following expressions:

$$G(s) = \frac{1}{\rho(s)} = \frac{e}{p_0}B(s), \tag{2.4}$$

$$K(s) = \frac{e}{p_0}\left.\frac{\partial B(s)}{\partial x}\right|_{y=0}, \tag{2.5}$$

where p_0 is the ideal electron momentum. The dipole magnetic fields $B(s)$ must be in the vertical direction to deflect the electrons horizontally. Observe that the function $G(s)$ is the inverse of the radius of curvature of the electron path through the dipoles. $G(s)$ and $K(s)$ are defined by the magnetic lattice and they are called lattice functions. For a storage ring, these functions are periodic, i.e., $G(s) = G(s + L_0)$ and $K(s) = K(s + L_0)$, where L_0 is the storage ring circumference.

From the Hamiltonian in Eq. (2.3), the equations of motion are:

$$x'' + \Big(K(s) - G^2(s)\Big)\,x = G(s)\delta, \tag{2.6}$$

$$y'' - K(s)y = 0. \tag{2.7}$$

[1] The approximated transverse Hamiltonian is obtained from the Hamiltonian of a relativistic charged particle on magnetic fields: $H = q\phi + c\sqrt{m^2c^2 + \left(\vec{p} - q\vec{A}\right)}$.

From the adiabatic approximation, in this derivation it was considered that the energy deviation δ is constant during the transverse motion. The equation of motion for the horizontal plane contains a non-homogeneous term $G(s)\delta$ due to the dependence of position with energy created at dipoles. This term couples the horizontal and longitudinal motions.

If we consider only the homogeneous part, x and y equations can be cast in the same form:

$$u'' + K_u(s)u = 0, \tag{2.8}$$

where $u = x$ or y, $K_x(s) = K(s) - G^2(s)$ and $K_y(s) = -K(s)$. Note that $K_x \approx -K_y$ if we consider $G^2/K \ll 1$, which is a good approximation for strong-focusing magnetic lattices. This reflects the fact that a focusing quadrupole in x plane is necessarily defocusing in the y plane and vice-versa.

The homogeneous Eq. (2.8) is called Hill equation, which is similar to a simple harmonic oscillator equation, except for the important fact that the term K_u is $s-$dependent and periodic. The authors in [48] proposed a pseudo-harmonic solution for the Hill equation, given by:

$$u_\beta(s) = \sqrt{2J_u\beta_u(s)}\cos\left(\varphi_u(s) - \phi_u\right). \tag{2.9}$$

This solution describes the so-called betatron oscillations. $\beta_u(s)$ is the betatron function and $\varphi_u(s)$ is the betatron phase advance. Inserting this solution in the Hill equation, it is obtained that the $\beta_u(s)$ must satisfy the following differential equation:

$$\frac{1}{2}\beta_u\beta_u'' - \left(\frac{\beta_u'}{2}\right)^2 + K_u(s)\beta_u^2 = 1, \tag{2.10}$$

and also that the betatron function and phase advance are related by

$$\varphi_u(s) = \int_0^s \frac{1}{\beta_u(\bar{s})}\mathrm{d}\bar{s}. \tag{2.11}$$

In storage rings, the betatron function is a periodic solution for Eq. (2.10).

The parameters J_u and ϕ_u are constants defined by the electron initial conditions. One can show that the constant J_u is written in terms of (u, u') as

$$2J_u = \gamma_u u^2 + 2\alpha_u u u' + \beta_u u'^2, \tag{2.12}$$

for every longitudinal position s and using the identities $\alpha_u(s) = -\beta_u'(s)/2$ and $\gamma_u(s) = (1 + \alpha_u^2(s))/\beta_u(s)$. These three functions $\{\alpha_u(s), \beta_u(s), \gamma_u(s)\}$ are called Twiss functions and depend only on the magnetic lattice.

In Eq. (2.12) it is shown that, for each position s, the betatron oscillations performed by the electrons in the storage ring over the turns draw a ellipse in the phase

space (u, u'). The ellipse shape varies with the longitudinal position s, however the ellipse area is constant for every s. Since the assumptions made so far allow us to consider the system as conservative, the ellipse area invariance in phase space is a direct consequence of Liouville's theorem. From Eq. (2.12), the ellipse area is $A_u = 2\pi J_u$, following that J_u is an invariant of motion. It is also possible to obtain this result applying the canonical transformation of action-angle variables in the Hamiltonian of Eq. (2.3), identifying the action as J_u (in this case, it is an invariant by construction), and the phase variable as φ_u.

Once these concepts are presented, we define the particle emittance as $\varepsilon_u = 2J_u$. In this way, the particle emittance can be interpreted as the area of the ellipse that the electron follows in the 4D phase space during betatron oscillations, divided by π:

$$\varepsilon_u = \frac{A_u}{\pi}. \tag{2.13}$$

As discussed, it follows that the particle emittance is an invariant for the betatron motion. From the ellipse equation analysis, the maximum values for u and u' are:

$$u_{\beta,\max}(s) = \sqrt{\varepsilon_u \beta_u(s)}, \tag{2.14}$$

$$u'_{\beta,\max}(s) = \sqrt{\varepsilon_u \gamma_u(s)}. \tag{2.15}$$

After obtaining the single particle parameters, one can introduce the excitation and damping processes due to radiation in this description and then apply statistical methods to obtain equilibrium parameters for an ensemble of non-interacting (independent) electrons – the electron beam. The distribution of invariants ε_u leads to the natural beam emittance ε_0, which for Sirius storage ring is 251 pm rad.

In a storage ring, the betatron phase advance accumulated over one turn is related to the number of betatron oscillations completed by the electrons. This number is called tune, given by

$$\nu_u = \frac{1}{2\pi} \oint \frac{1}{\beta_u(s)} \mathrm{d}s, \tag{2.16}$$

where the closed integral represents an integration where the lower limit is an arbitrary s and the upper limit is $s + L_0$, closing one turn around the ring.

The tune has an integer part (the number of complete betatron oscillations over one turn) and a fractional part. Because of this fractional part the values of (x, x', y, y') at some s may be different for each turn. The betraton oscillations peaks and valleys are $\pm\sqrt{\varepsilon_u \beta_u(s)}$. Therefore, the single particle emittance ε_u and the $\beta_u(s)$ function defines the envelope of betatron oscillations.

The tune fractional part is closely related to resonances. If the fractional part is zero, i.e., the tune is an integer number, in every turn the particles have the same

coordinates (u, u') for every s. Then if there are dipolar field errors at the magnetic lattice, these errors distort the electrons orbit in the same way at every turn, increasing the distortion amplitude and leading to electron losses. If the fractional part is ½, the resonance is excited by quadrupolar field errors. Generally, there are resonances that can be excited if the tunes satisfy the relation

$$m\nu_x + n\nu_y = r, \tag{2.17}$$

where $m, n, r \in \mathbb{Z}$. The order of resonance is $|m| + |n|$ and the resonance strength decays with the increase of its order, thus the lower order resonances are more harmful to the beam stability. Eq. (2.17) determines resonance lines in the space (ν_x, ν_y) that must be avoided to prevent the electron beam from this type of instability. The tunes values must be carefully chosen for the machine operation point. The Sirius storage ring design tunes are $\nu_x = 49.0962$ and $\nu_y = 14.1520$.

2.2.2 Dispersion function

It can be seen from the radius of curvature created by the dipoles that an electron with energy deviation δ is more deflected if $\delta < 0$ and less deflected if $\delta > 0$, compared to the on-energy electron with $\delta = 0$. Thus this energy difference is translated in different horizontal displacements. This effect is represented by the non-homogeneous term $G(s)\delta$ in the horizontal equation of motion, which couples longitudinal and horizontal motions.

The homogeneous equation was already solved in the last section, leading to betatron oscillations x_β. Therefore the general solution to the horizontal plane is a combination of x_β and a particular solution for the non-homogeneous equation. As discussed, it is known that this particular solution must be a function of s and δ. From Eq. (2.6), it can be seen that the particular solution for the non-homogeneous equation must be linear with respect to the energy deviation δ, therefore

$$x(s, \delta) = x_\delta(s) = \eta(s)\delta, \tag{2.18}$$

where the s-dependence is retained in the function $\eta(s)$, called dispersion function. Inserting the proposed solution into the differential equation, it is obtained that $\eta(s)$ must satisfy

$$\eta'' + K_x(s)\eta = G(s). \tag{2.19}$$

For a periodic magnetic lattice as used in storage rings, $\eta(s)$ is a periodic solution to this differential equation. We finally obtained the transverse displacement solutions to the equations of motion, where $x(s) = x_\beta(s) + x_\delta(s)$ and $y(s) = y_\beta(s)$.

Imperfections such as magnet misalignment or construction errors can introduce horizontal dipolar and skew quadrupolar fields, generating a vertical dispersion function,

i.e., a dependence on vertical position with energy as well. Nevertheless, in this case the steps made to obtain the solution for x plane can be reproduced to obtain a equivalent solution to the y plane. Moreover, typically it is desired to keep $\eta_y(s)$ as low as possible and there are some strategies to achieve this goal, which will be discussed in this work.

2.3 Longitudinal dynamics

In the previous section it was considered that the electron energy remains constant during the transverse motion typical time scale, which is a good approximation. On the other hand, since electrons are charged particles and in a storage ring they are submitted to centripetal acceleration at dipoles and IDs, synchrotron radiation is generated and the electrons lose energy. The energy loss is then compensated by the accelerating fields contained in the RF cavity. During this process the electron energy oscillates and this motion is known as synchrotron oscillations.

2.3.1 Orbit Length

In dipoles, for an electron with nominal energy, the oscillations occur symmetrically about $x = 0$. In straight sections, the path length variation due to betatron oscillations is proportional to the square of the betatron amplitude. Thus, when the electron trajectory is integrated over one turn (which corresponds to several betatron cycles), the change in the path length due to the betatron motion is zero in first order. On the other hand, the horizontal energy-dependent term $x_\delta(s) = \eta(s)\delta$ has a significant first-order contribution.

The momentum compaction factor is a parameter that depends on the magnetic lattice and is fundamental to the longitudinal dynamics. This dimensionless parameter, denoted as $\alpha \in \mathbb{R}$, relates the electron energy deviation with its orbit length:

$$\frac{\Delta L}{L_0} = \alpha \frac{\Delta p}{p_0} = \alpha\delta. \tag{2.20}$$

In terms of the period of electron motion around the ring, it is obtained that

$$\frac{\Delta T}{T_0} = \left(\alpha - \frac{1}{(v/c)^2\gamma^2}\right)\delta, \tag{2.21}$$

The term $\alpha - \dfrac{1}{(v/c)^2\gamma^2}$ is known as slip factor and, for ultra-relativistic electrons, it is very close to α. For example, on Sirius storage ring $\alpha = 1.6 \times 10^{-4}$, $v/c \approx 1$ and $\gamma = 5871$, so the difference between the slip factor and α is only 3×10^{-8}. Therefore,

$$\frac{\Delta T}{T_0} \approx \alpha\delta \tag{2.22}$$

is usually a good approximation.

The momentum compaction can be obtained in terms of lattice functions as:

$$\alpha = \frac{1}{L_0} \oint G(s)\eta(s)\mathrm{d}s. \tag{2.23}$$

Typically $\alpha > 0$ in synchrotrons. In this case, from Eq. (2.20), an electron with $\delta > 0$ follows an orbit with greater length, as compared to the nominal orbit length L_0. The opposite happens for an electron with $\delta < 0$.

2.3.2 Synchrotron Oscillations

Consider the synchronous electron with the nominal energy E_0, following the ideal orbit through the storage ring. In each turn, this electron radiates synchrotron light, losing the amount U_0 of energy. U_0 is typically much lower than the electron energy E_0. An electron with energy E_0 but not following the ideal orbit performs several betatron oscillations in one turn and the transverse displacements average to zero in first order. Hence, in this case, the energy loss per turn is U_0 too.

On the other hand, the energy loss per turn has a first order difference from U_0 for an electron with energy deviation δ. This off-energy electron follows an orbit displaced horizontally by $\eta(s)\delta$ and the electron experiences different fields systematically along the ring. Furthermore, the energy loss depends on the electron energy by itself. Accounting for these two effects, the energy loss must be a function $U_{\mathrm{rad}}(\delta)$ satisfying $U(0) = U_0$. It is considered that $\delta \ll 1$ for electrons in a storage ring, so it is reasonable to keep only the linear part of $U_{\mathrm{rad}}(\delta)$:

$$U_{\mathrm{rad}}(\delta) \approx U_0 + \frac{\mathrm{d}U_{\mathrm{rad}}}{\mathrm{d}\delta}\delta. \tag{2.24}$$

The energy gain process concerns the RF accelerating system. The resonant cavity installed in the storage ring receives a RF signal, creating an oscillating electric field inside the cavity. This electric field has a longitudinal component that might accelerate the electrons and allow for the electrons energy recovery.

The RF net voltage depends on the initial phase of the field when the particle enters the cavity and can be obtained from the integral of longitudinal electric field along the electron path. Since this potential is oscillating in time, the possible electron energy gain per turn is also time dependent. In order to keep the electron energy stable, the ideal electron energy balance must be zero, i.e., the energy gained by the RF cavity must always be U_0 at each turn, for the ideal electron. To achieve this, the ideal electron circular motion must be synchronized to the RF voltage oscillation, and this is why ideal electrons are also called synchronous electrons. This is equivalent to the requirement that the RF cavity potential oscillating frequency f_{rf} must be a multiple of the ideal electron revolution frequency f_0

$$f_{\mathrm{rf}} = hf_0, \tag{2.25}$$

where the integer h is called harmonic number.

We are interested in deviations from the synchronous electron, then the absolute time dependence of $V_{\rm rf}(t)$ can be replaced by the coordinate $\tau(t) = z(t)/c$ that is the relative difference to the ideal arrival time at the cavity. In this way, an electron energy gain is given by $eV_{\rm rf}(\tau)$ and for the ideal electron we require that $eV_{\rm rf}(0) = U_0$. Since the longitudinal displacements τ are small as well, we may expand the energy gain in first order:

$$U_{\rm rf}(\tau) = eV_{\rm rf}(\tau) \approx U_0 + e\frac{{\rm d}V_{\rm rf}}{{\rm d}\tau}\tau. \tag{2.26}$$

Now we are ready to obtain the differential equation for the longitudinal motion. Observe that from Eq. (2.20) the orbit length (and the revolution time) depends on the energy deviation δ. Let the sub-index n denote the turn number. In successive turns the relative position $z(t)$ changes by $\Delta z = z_{n+1} - z_n = \alpha\delta_n L_0$. Converting it to time variables, then $\Delta\tau = \alpha\delta_n T_0$, where T_0 is the revolution period. As mentioned, the longitudinal dynamics time scale is much greater than the time involved in one turn, then longitudinal changes in consecutive turns divided by the revolution time T_0 can be regarded as derivatives. Hence

$$\frac{{\rm d}\tau}{{\rm d}t} = \alpha\delta. \tag{2.27}$$

From the electron energy balance $\Delta E = E_{n+1} - E_n = eV(\tau_n) - U_{\rm rad}(\delta_n)$. Dividing by T_0 and E_0 we obtain:

$$\frac{{\rm d}\delta}{{\rm d}t} = \frac{eV_{\rm rf}(\tau) - U_{\rm rad}(\delta)}{E_0 T_0}.. \tag{2.28}$$

The coupled differential equations Eq. (2.27) and Eq. (2.28) describe the longitudinal dynamics in the phase space (τ, δ). With the linear approximations made in equations Eq. (2.24) and Eq. (2.26), the differential equations can be cast in the following form:

$$\ddot{v} + 2\alpha_z\dot{v} + \omega_z^2 v = 0, \tag{2.29}$$

where $v = \tau$ or δ and the dot represents the time derivative. Eq. (2.29) describes a damped harmonic oscillator, with frequency $\omega_z = \sqrt{\dfrac{\alpha e}{E_0 T_0}\dfrac{{\rm d}V_{\rm rf}}{{\rm d}\tau}}$, called synchrotron frequency. The term $\alpha_z = \dfrac{1}{2T_0}\dfrac{{\rm d}U_{\rm rad}}{{\rm d}\delta}$ is positive, represents the effect of radiation damping and it is typically small.

In the small oscillation limit, the phase-space trajectories are ellipses with decreasing radius towards $\tau = \delta = 0$. In the general case of large oscillations, the longitudinal dynamics is not equivalent to a damped oscillator anymore and the dynamics is non-linear. The electrons trajectories in phase space are divided in two classes: 1) closed, limited and stable and 2) open, unlimited and unstable. The stable regions in the phase space are called RF buckets and a separatrix delimits the stable from the unstable region, where the limit is the stable trajectory with largest amplitudes.

It is important to observe that to keep electrons oscillating longitudinally, it is required that $\left.\frac{\mathrm{d}V_{\mathrm{rf}}}{\mathrm{d}\tau}\right|_{\tau=0} > 0$, otherwise the synchrotron frequency would be an imaginary number and the motion would be unstable. Note that while the "restoring force" for the betatron oscillation comes from the focusing function (basically the field gradients), the equivalent for the synchrotron oscillations comes from the RF potential derivative.

The typical RF potential is sinusoidal $V_{\mathrm{rf}}(\tau) = \hat{V}_{\mathrm{rf}} \sin(\omega_{\mathrm{rf}}\tau + \phi_s)$ where $\hat{V}_{\mathrm{rf}}$ is the peak RF potential. From the energy balance $eV_{\mathrm{rf}}(0) = U_0$ we obtain that $\sin(\phi_s) = U_0/e\hat{V}_{\mathrm{rf}}$ and ϕ_s is called, as expected, the synchronous phase.

Since $\omega_{\mathrm{rf}} = h\omega_0$, where ω_0 is the angular revolution frequency, there are $2h$ occurrences of $eV_{\mathrm{rf}}(0) = U_0$ during one revolution period but only in half of them the stability condition $\left.\frac{\mathrm{d}V_{\mathrm{rf}}}{\mathrm{d}\tau}\right|_{\tau=0} > 0$ is satisfied. Hence, there are h RF buckets in the longitudinal phase space, where electrons can be stored in bunches. For the Sirius storage ring, it is possible to accumulate electrons in 864 bunches.

2.3.3 Phase Stability

The principle of phase stability is a fundamental concept to the realization of synchrotrons. It establishes a mechanism that guarantees that electrons with energy or longitudinal phase deviations are forced towards the synchronous condition.

Suppose an electron with energy deviation $\delta > 0$ in a storage ring. From Eq. (2.22), it takes more time to this electron perform one turn, to reach the RF cavity and from the convention used to the coordinate definition, $\tau < 0$ for this electron. Since the RF potential derivative must be positive at $\tau = 0$, the energy gain U_{rf} for $\tau < 0$ is lower than U_0; moreover, $U_{\mathrm{rad}} > U_0$ for electrons with $\delta > 0$. Thus, the energy balance for this electron is negative, leading it to lower values of δ and also τ.

The analysis is basically the same for electrons initially with $\delta < 0$. These electrons perform each turn faster than the synchronous electron, having $\tau > 0$ and gaining more energy from the cavity than is lost by radiation. This positive energy balance increases the values of δ and τ.

The phase stability principle ensures that the electrons oscillate around the longitudinal fixed point $(\tau = 0, \delta = 0)$. The radiation damping effect makes it possible to the longitudinal deviations be damped to this fixed point. On the counterpart, the quantum nature of radiation emission produces an excitation effect and the balance between damping and excitation creates an equilibrium configuration.

Since the synchronous condition must be satisfied, from Eq. (2.22) it is obtained

that:

$$\frac{\Delta f_{\mathrm{rf}}}{f_{\mathrm{rf}}} = -\frac{\Delta T}{T_0} \approx -\alpha\delta. \tag{2.30}$$

From this equation it can be seen that a change in the RF frequency forces the electrons to follow an off-energy orbit. This principle also allows for increasing the electron energy in synchrotrons. Increasing the magnetic fields forces the electrons to reach new synchronous conditions related to higher energies. To achieve that, the electrons must gain more energy from the RF cavity, and the phase stability principle drives this process automatically. In Sirius booster, the electron energy ramp is performed from 150 MeV to 3 GeV.

2.4 Perturbations

The effects of magnets and field errors in the electron beam can be minimized with increasingly advanced techniques for magnets construction and alignment. Nevertheless, the errors are impossible to be completely eliminated in practice. Furthermore, the magnets parameters are measured by bench devices that are less sensitive to errors than the electron beam. Hence, deviations from ideal conditions must be considered in the accelerator physics studies in order to develop methods for their diagnostics and corrections. In this section we will present the perturbations on the electron beam properties caused by low-order errors that are found in storage rings.

2.4.1 Orbit

The first natural error type to be studied is the dipolar. Dipolar errors disturb the closed orbit for the electron motion. Depending on the distribution and magnitude of these errors, a closed orbit solution may not even exist, then, without corrections, it would be impossible to keep electrons in stable conditions in the storage ring. Typically, even considering that all the specifications regarding the magnets fabrication and alignment were met, the dipolar errors might provide a closed orbit solution with large distortions around the ring. Despite this, the orbit distortions can be measured by the BPMs and minimized with dipolar correctors (or steering magnets).

The typical sources of dipolar errors are:

- dipolar fields from transverse alignment errors in quadrupoles. An electron with the deviation x passing through a focusing quadrupole perfectly aligned to the reference orbit receives a force $-Kx$ in the horizontal plane. If the quadrupole center is misplaced from the center by x_0, the focusing force is $-K(x - x_0)$, therefore the misalignment introduces an additional dipolar term Kx_0 every time the electrons

pass through this quadrupole. This is called feed-down effect[2], in which alignment errors in n-order fields produce $(n-1)$-order fields contributions;

- differences between ideal and real dipolar fields in dipole magnets, due to fabrication errors or remnant fields. In the case of electromagnets, the excitation curve that relates the applied current on the power supply and the magnetic fields in the magnet must be well calibrated, otherwise the actual field in the magnets differ from the expected;
- horizontal dipolar fields, which should be ideally zero, due to rotation errors in dipole magnets;
- non-zero field integrals from IDs;
- spurious magnetic sources along the ring, such as current ripple from magnet power supplies, ion pumps, leak fields from injection pulsed magnets, building and ground position drifts due to temperature or ground settlement, girder vibration (due to water flow, crane, pumps, etc), electromagnetic noise.

We will study how a dipolar error ΔG_u (where $u = x, y$), localized in a small longitudinal region Δs, affects the closed orbit solution. The additional term ΔG_u can be regarded as a perturbation in the Hamiltonian of Eq. (2.3) for the transverse dynamics. An approximation can be made to consider the dipolar error as a localized "kick":

$$\lim_{\Delta s \to 0} \Delta G_u(s) \Delta s = \theta_{s_0} \delta(s - s_0),$$

where $\delta(s - s_0)$ is the Dirac delta distribution centered at s_0, so in this way the quantity $\Delta G_u(s)\Delta s$ is finite in the limit $\Delta s \to 0$. This dipolar kick adds a sudden change in the angle of the electron trajectory when it reaches s_0, given by:

$$\begin{aligned} \Delta u'(s_0) &= \Delta G_v(s) \Delta s \\ &= -\oint \theta_{s_0} \delta(s - s_0) \mathrm{d}s = -\theta_{s_0}. \end{aligned}$$

If the dipolar field error is vertical, $v = y$, the angle change is horizontal, $u = x$ and the dipolar kick is also named as horizontal. If the field error is horizontal, $v = x$, the angle change is vertical, $u = y$ and the kick is called vertical. The sign follows from the angle coordinate definition, if $\Delta G_y > 0$ then $\Delta x' < 0$ and if $\Delta G_x > 0$, then $\Delta y' > 0$.

The angle change produces betatron oscillations in the electron motion, arriving at the dipolar error in each turn with different positions and angles. After some time, the transverse motion is damped to a distorted closed orbit.

[2] The Appendix A is dedicated to brief discussions and derivations related to this effect.

In the presence of this dipolar kick, the transverse equations of motion are:

$$x'' + K_x(s)x = G_y(s)\delta - \Delta G_y(s), \tag{2.31}$$

$$y'' + K_y(s)y = \Delta G_x(s). \tag{2.32}$$

Remember that $u'' = \frac{\Delta u'}{\Delta s}$, then writing the above equations as $\Delta u' + K_u(s)u\Delta s = \Delta G_v(s)\Delta s$ and taking the limit $\Delta s \to 0$, $\Delta u' = \theta^u_{s_0}$ is recovered.

With the kick approximation, the dipolar error can be viewed as an impulse term in the linear differential equations for the transverse motion. Hence, the theory of Green's function can be applied. The solution obtained from this analysis is [47]:

$$\Delta u(s) = \frac{\sqrt{\beta_u(s)\beta_u(s_0)}}{2\sin(\pi\nu_u)}\Delta G_v(s_0)\Delta s\cos\left(|\varphi_u(s) - \varphi_u(s_0)| - \pi\nu_u\right), \tag{2.33}$$

and this is the orbit distortion for a dipolar error localized in the position s_0. The generalization for a distribution of errors $\theta_u(s)$ is quite direct:

$$\Delta u(s) = \oint \frac{\sqrt{\beta_u(s)\beta_u(\bar{s})}}{2\sin(\pi\nu_u)}\theta_u(\bar{s})\cos\left(|\varphi_u(s) - \varphi_u(\bar{s})| - \pi\nu_u\right)\mathrm{d}\bar{s}. \tag{2.34}$$

Note that the orbit distortion diverges if the tune is an integer. Here the connection between dipolar fields errors and integer resonances becomes explicit. Moreover, it is very important to point out that the orbit distortion depends on the betatron functions and the betatron phase advances, i.e., it depends on the optics parameters of the magnetic lattice.

2.4.2 Optics

Quadrupolar (or gradient) errors disturb the focusing functions in the magnetic lattice, therefore perturb the storage ring linear optics. The typical sources of quadrupolar errors are:

- differences between ideal and real gradient fields in the quadrupoles magnets, due to fabrication errors or remnant fields. The excitation curve must be well calibrated too, otherwise the actual field in the magnets differs from the expected;
- gradient fields in dipoles magnets that are not expected in the magnets field characterization;
- feed-down effects from horizontal alignment errors in sextupoles magnets. An electron with the deviation x passing through a focusing sextupole perfectly aligned to the reference orbit receives a force $-Sx^2$ in the horizontal plane. If the sextupole center is misplaced from the center by x_0, the force is $-S(x - x_0)^2$, therefore the

misalignment introduces an additional horizontal focusing term Sx_0x, where the focusing strength is given by Sx_0, and a dipolar term $-Sx_0^2$, that influence the electrons every time they pass through this sextupole.

A gradient error ΔK_u (where $u = x, y$), localized in a small longitudinal region Δs, changes the conditions that the betatron function must satisfy in Eq. (2.10). Therefore this error disturbs the betatron function solution, consequently the betatron phase advance and the betatron tunes.

An approximation can be made to consider the single gradient error as a thin lens. The focal length added in this case is $1/f_u = \Delta K_u \Delta s$. If the gradient error is on a quadrupole with length L, the focal length is then obtained from the integrated field along the quadrupole, $1/f_u = \Delta K_u L$. With this approximation the gradient error effect can be regarded as an impulse $\delta K_u(s) = \Delta K_u L \delta(s - s_0)$ located at s_0.

Assuming the error ΔK_u is small, then only first order terms can be kept. The correspondent change in the betatron tunes for a integrated gradient error $\Delta K_u L$ located at s_0 can be obtained as

$$\Delta\nu_u = \frac{1}{4\pi}\beta_u(s_0)\Delta K_u L. \tag{2.35}$$

For a quadrupole, $\Delta K_x = -\Delta K_y$, then a positive error in the focusing strength increases ν_x and decreases ν_y. Note that the tune change depends on the non-perturbed betatron function value at the error location.

For a general gradient error distribution around the ring, the tune change is:

$$\Delta\nu_u = \frac{1}{4\pi}\oint \beta_u(s)\delta K_u(s)\mathrm{d}s. \tag{2.36}$$

The solution for Eq. (2.10) in the presence of a distribution of gradient errors provides the relative change in the betatron function given by

$$\frac{\Delta\beta_u(s)}{\beta_u(s)} = \frac{1}{2\sin(2\pi\nu_u)}\oint \delta K_u(\bar{s})\beta_u(\bar{s})\cos\left(2\left(|\varphi_u(s) - \varphi_u(\bar{s})| - \pi\nu_u\right)\right)\mathrm{d}\bar{s}. \tag{2.37}$$

The ratio $\Delta\beta/\beta$ is called beta-beating and it is a measure of the betatron function distortion. The beta-beating in a storage ring must be as low as possible, indicating that the betatron function for the real machine is close to the nominal one. Observe that the beta-beating diverges if the tune fractional part is a half-integer. Thus, the association between gradient fields errors and half-integer resonances can be seen.

The dispersion function $\eta(s)$ may be changed in the presence of dipolar and quadrupolar errors as well, since it must satisfy the differential Eq. (2.19), which depends on the lattice functions $G(s)$ and $K(s)$. An analytical expression for the dispersion variation in the presence of these errors is not very insightful to be presented here, but it

is important to keep in mind that lattice imperfections may disturb the $\eta(s)$ function and the most direct parameter that may be affected by these errors is the beam emittance.

2.4.3 Linear Coupling

There are some types of errors that couple the dynamics in the transverse planes. The rotated quadrupolar fields are called skew gradients (the previous gradients introduced are called normal). In this subsection we will study the effects of linear coupling on the dynamics. Typical coupling sources are:

- rotation errors in the quadrupoles. These errors add skew gradients to the lattice: focusing forces in the x plane which are dependent on the y displacements and vice-versa;
- feed-down effects due to vertical alignment errors in sextupoles magnets. An electron with the deviation x and y passing through a focusing sextupole perfectly aligned to the reference orbit receives a force $S(x^2 - y^2)$ in the horizontal and Sxy in the vertical plane. If the sextupole center is misplaced from the center by y_0, the terms Sy_0y and $-Sy_0^2$ are added in the horizontal, and the force Sy_0x is added in the vertical plane. Hence, there are focusing forces, with strength Sy_0, in one transverse plane that depends on position deviations in the perpendicular plane, i.e., skew gradients;

We may consider the skew gradients distribution around the storage ring as small perturbations to the electron dynamics. Suppose that this distribution is represented by the lattice function $K_S(s)$, namely skew-focusing function, generated by rotated quadrupoles, for example. The homogeneous equations of motion with these new fields are changed by

$$x'' + K_x(s)x + K_S(s)y = 0, \tag{2.38}$$

$$y'' - K_y(s)y + K_S(s)x = 0. \tag{2.39}$$

Let the transverse Hamiltonian, without the energy dependent term, be

$$H_0 = \frac{x'^2}{2} + \frac{y'^2}{2} + K_x(s)\frac{x^2}{2} - K_y(s)\frac{y^2}{2},$$

then the Hamiltonian for the linearly coupled motion is

$$H = H_0 + K_S(s)xy,$$

and the term $H_1 = K_S(s)xy$ can be treated as a perturbation Hamiltonian.

Applying a convenient canonical transformation with the action-angle variables (a, ϕ) in H_1, it assumes the form [47]:

$$H_1 = \frac{K_S(s)}{2}\sqrt{\beta_x(s)\beta_y(s)}\sqrt{a_x a_y}\sum_{lx,ly\in(-1,1)} e^{i[l_x(\varphi_x+\phi_x)+ly(\varphi_y+\phi_y)]}.$$

From this expression, we are able to separate constants and slowly varying terms from fast oscillating terms. Using periodic properties for the functions in a storage ring, we rewrite the Hamiltonian as:

$$H_1 = \frac{\sqrt{a_x a_y}}{2}\sum_{lx,ly\in(-1,1)} A_{l_x,l_y}(s)e^{i[(l_x\nu_x+l_y\nu_y)2\pi s/L_0+l_x\phi_x+l_y\phi_y]},$$

where the factor $A_{l_x,l_y}(s)$ contains the periodic functions:

$$A_{l_x,l_y}(s) = K_S(s)\sqrt{\beta_x(s)\beta_y(s)}e^{i[l_x\varphi_x+l_y\varphi_y-(l_x\nu_x+l_y\nu_y)2\pi s/L_0]}.$$

Since $A_{l_x,l_y}(s)$ is periodic in L_0, we are able to expand it in terms of Fourier series:

$$A_{l_x,l_y}(\varphi) = \frac{2\pi}{L_0}\sum_q \kappa_{q,l_x,l_y}e^{iqN2\pi s/L_0}.$$

The coupling coefficients are obtained as:

$$\kappa_{q,l} = \frac{1}{2\pi}\oint K_S(s)\sqrt{\beta_x(s)\beta_y(s)}e^{i[\varphi_x+l\varphi_y-(\nu_x+l\nu_y-qN)2\pi s/L_0]}\mathrm{d}s, \tag{2.40}$$

where l is an integer number that satisfy $-1 \leq l \leq 1$ and it was used to substitute l_x, l_y. Generally the coupling coefficient is a complex number. This indicates that there are two orthogonal and independent contributions, then two orthogonal and independent knobs are necessary to correct the coupling. The corrections can be made by adding skew (rotated) quadrupoles in the storage ring to compensate the unwanted skew gradients.

The linear coupling resonances occur when $l = \pm 1$ and $\nu_x \pm \nu_y \approx qN$, q and N integers. These two resonances are called sum and difference coupling resonances. It can be shown that in the difference resonance the sum of the resonance amplitudes $a_x + a_y$ is constant, therefore this coupled motion is stable.

In this coupled motion there are two normal modes of oscillation, which defines new betatron frequencies (or tunes), given by:

$$\nu_{1,2} = \nu_{x,y} \pm \frac{1}{2}\sqrt{\Delta_{q,l}^2 + |\kappa_{q,l}|^2} \mp \frac{1}{2}\Delta_{q,l}^2, \tag{2.41}$$

where $\Delta_{q,l} = \nu_x + l\nu_y - qN$.

On the difference resonance, $\Delta_{q,-1} \approx 0$, we obtain that $\nu_1 = \nu_x + |\kappa_{q,-1}|/2$ and $\nu_2 = \nu_y - |\kappa_{q,-1}|/2$. Since the difference resonance is stable, we are able to approximate the tunes $\nu_x \approx \nu_y$, but there is a stop-band between the normal tunes given by

$$(\nu_1 - \nu_2)_{\min} = |\kappa_{q,-1}|. \tag{2.42}$$

Therefore, measuring the minimum difference between the tunes is a direct measurement of the coupling coefficient modulus, which is also called global betatron coupling.

Assuming that $\nu_x < \nu_y$ as an example, the tunes approximation can be performed by increasing a focusing quadrupole strength, in order to increase ν_x and decrease ν_y. Note that away from the coupling resonances, $\Delta_{q,l} \gg |\kappa_{q,l}|$ and from this we see that $\nu_1 \approx \nu_x$ and $\nu_2 \approx \nu_y$. Thus, while the tunes are away from each other, the normal and betatron tunes are basically the same. When ν_x is close to ν_y the measured oscillating frequencies are ν_1 and ν_2 which, in the presence of coupling, do not cross each other.

3 Linear Optics from Closed Orbits Method

Linear Optics from Closed Orbits (LOCO), is a model-dependent algorithm with the main objective of calibrating the accelerator model in order to reproduce an orbit response matrix measured in the real machine. Once this correspondence is achieved, it is considered that the calibrated model is a representation of the real machine in terms of the linear response of the magnetic lattice. Therefore, one can access the information from the real accelerator by analysing the model. The principal information that is studied in this process is related to the linear optics functions (betatron and dispersion functions), allowing for disturbances detection and, more importantly, to obtain the corrections that bring the real machine parameters closer to the nominal.

This method has been applied to several synchrotrons over the years and has been proven to be efficient both to detect optics perturbations and to correct the machine linear optics [34, 49, 50]. Besides that, with the realization of 4^{th} generation light sources, which use innovative and very compact magnetic lattices and optics, some details and subtleties of LOCO should be revisited to successfully apply the method in modern machines such as the Sirius storage ring. This chapter is dedicated to present LOCO method and to discuss the aforementioned details.

3.1 Orbit Response Matrix Analysis

If a j-th dipolar corrector strength is locally varied by the amount $\Delta\theta_j$, the electron closed orbit is distorted. The horizontal and vertical distortions (Δx and Δy) can be measured by the BPMs. With the distortions measured by the i-th BPM, the following quantities can be calculated in this process:

$$M_{ij}^{uv} = \frac{\Delta u_i}{\Delta \theta_j^v}. \tag{3.1}$$

If the corrector magnet is horizontal, $v = x$ and if it is vertical, $v = y$. For each corrector varied, one can measure the corresponding positions variations at every BPM, horizontally $u = x$ and vertically $u = y$. These values can be cast in an array $\mathbf{M}$, called Orbit Response Matrix (ORM). Usually the element ordering in this matrix is the following:

$$\mathbf{M} = \begin{bmatrix} \mathbf{M}^{xx} & \mathbf{M}^{xy} \\ \mathbf{M}^{yx} & \mathbf{M}^{yy} \end{bmatrix}. \tag{3.2}$$

The sub-matrices $\mathbf{M}^{xx}$ and $\mathbf{M}^{yy}$ in the diagonal blocks are the elements with larger values in the ORM. In a magnetic lattice with zero transverse coupling (such as

the nominal magnetic lattice for Sirius storage ring) the sub-matrices $\mathbf{M}^{xy}$ and $\mathbf{M}^{yx}$ in the off-diagonal blocks are zero. The order of magnitude of the elements in off-diagonal blocks compared to the diagonal blocks is smaller by the same order of magnitude of the transverse coupling, typically a few percent without corrections.

For the uncoupled case, it is possible to obtain an analytical expression for the ORM elements in the diagonal blocks. In Eq. (2.34), the orbit distortion in the presence of a given dipolar kick distribution $\theta_u(s)$ was shown. For the special case that the kick distribution is discrete, localized in the dipolar correctors positions s_j, with values $\Delta\theta_j^u$, Eq. (2.34) is rewritten in the form:

$$\Delta u(s_i) = \sum_j \frac{\sqrt{\beta_u(s_i)\beta_u(s_j)}}{2\sin(\pi\nu_u)} \Delta\theta_j^u \cos\left(|\varphi_u(s_i) - \varphi_u(s_j)| - \pi\nu_u\right). \tag{3.3}$$

The orbit distortions $\Delta u(s_i)$ are also measured in discrete and localized positions s_i, where the BPMs are installed. The above equation can be cast in the form $\Delta u_i = \sum_j M_{ij}^{uu}\Delta\theta_j^u$, therefore the ORM elements can be recognized as:

$$M_{ij}^{uu} = \frac{\sqrt{\beta_u(s_i)\beta_u(s_j)}}{2\sin(\pi\nu_u)} \cos\left(|\varphi_u(s_i) - \varphi_u(s_j)| - \pi\nu_u\right). \tag{3.4}$$

Note that the ORM elements contain information about the local betatron function at BPMs and correctors positions. It also encodes the relative betatron phase advance between each pair of BPM and steering magnet and the ORM also depends on the betatron tune, a global parameter.

Following the sorting used in the ORM, the orbit distortions and the dipolar kick variations can be arranged in vectors

$$\Delta\vec{u} = (\Delta x_1, \ldots, \Delta x_{\mathrm{N_{BPM}}}, \Delta y_1, \ldots, \Delta y_{\mathrm{N_{BPM}}}),$$
$$\Delta\vec{\theta} = \left(\Delta\theta_1^x, \ldots, \Delta\theta_{\mathrm{N_{CH}}}^x, \Delta\theta_1^y, \ldots, \Delta\theta_{\mathrm{N_{CV}}}^y\right).$$

$\mathrm{N_{BPM}}$ is the number of BPMs, $\mathrm{N_{CH}}$ is the number of horizontal correctors (CH) and $\mathrm{N_{CV}}$ is the number of vertical correctors (CV). The orbit correction system for Sirius storage ring has $\mathrm{N_{BPM}} = 160$, $\mathrm{N_{CH}} = 120$ and $\mathrm{N_{CV}} = 160$. In this vectorial form, Eq. (3.3) is $\Delta\vec{u} = \mathbf{M}\Delta\vec{\theta}$, so the ORM has dimension $2\mathrm{N_{BPM}} \times (\mathrm{N_{CH}} + \mathrm{N_{CV}})$.

Suppose that the BPMs measure the orbit distortion $\vec{u}_\mathrm{d}$. With the dipolar correctors it is possible to produce an orbit variation that minimizes the 2-norm of the residual orbit. From the minimization of $||\vec{u}_\mathrm{d} - \mathbf{M}\Delta\vec{\theta}||^2$ with respect to $\Delta\vec{\theta}$, the required kick variations are $\Delta\vec{\theta} = -\left(\mathbf{M}^\mathsf{T}\mathbf{M}\right)^{-1}\mathbf{M}^\mathsf{T}\vec{u}_\mathrm{d}$. Since the actual problem is non-linear, the corrections must be calculated and applied iteratively until convergence.

The pseudo-inverse of $\mathbf{M}^\mathsf{T}\mathbf{M}$ can be obtained with the method of Singular Value Decomposition (SVD) pseudo-inversion which is described in Appendix B. Using this

method and, depending on the number of fit parameters compared to the number of data points, it is also possible to minimize the correctors strengths required to minimize the figure of merit, in this case, the orbit distortion 2-norm.

It is common to also include the RF frequency as a knob in the orbit correction system. This can be done by adding in the last column of the ORM the orbit distortion vector produced by a variation in the RF frequency. From Eq. (2.30) and using $\Delta u_i = \eta_u(s_i)\delta$, we obtain:

$$\frac{\Delta u_i}{\Delta f_{\mathrm{rf}}} = -\frac{\eta_u(s_i)}{\alpha f_{\mathrm{rf}}}. \tag{3.5}$$

Adding this extra knob to the orbit correction system is very important to correct beam energy variations through orbit length, which can be generated by thermal drifts of the storage ring tunnel, tidal effects, etc. It is important to observe that the RF signature in the orbit distortion is very different from the signature created by the correctors, since the first depends on the dispersion function and the latter on the betatron function.

The ORM with the RF frequency column added is then a matrix with dimension $2\mathrm{N_{BPM}} \times (\mathrm{N_{CH}} + \mathrm{N_{CV}} + 1)$. For the Sirius storage ring, the ORM is a 320×281 matrix. Beyond the function of calculating the corrections for orbit distortions, the ORM contains a lot of information about the uncoupled linear optics (betatron function, phase advance and horizontal dispersion function) and the coupled linear optics (betatron coupling and vertical dispersion function). LOCO method explores extensively the information contained in the ORM.

3.2 Minimization Problem

To implement LOCO method, a storage ring model is required. In this model, it is possible to calculate the nominal ORM. That can be done by simulating numerically the measurement process which consists in varying the correctors strength and getting the corresponding orbit distortion in all BPMs, for every corrector in the lattice. The nominal ORM calculation can be perfomed also using the transfer matrices of the lattice. In this formalism, which is much faster computationally, the ORM elements can be obtained by the composition of the transfer matrices of the elements between the correctors and the BPMs. If non-linear effects in the orbit distortion can be disregarded (for example using small kicks variations), the two calculation methods produce very similar ORMs, thus, for the sake of sparing computation time, the transfer matrices approach is often used.

The LOCO method can be viewed as a model-dependent minimization problem. The main goal is to find a set of parameters in the computational model that best reproduce the measured ORM. Equivalently, it seeks for the global minimum of the square

differences:

$$\chi^2 = \sum_{i,j} \left(M_{ij}^{\text{measured}} - M_{ij}^{\text{model}} \right)^2 =: \sum_{k=(i,j)} V_k^2. \tag{3.6}$$

The residue vector $\vec{V}$ has $2 \times \text{N}_{\text{BPM}} \times (\text{N}_{\text{CH}} + \text{N}_{\text{CV}} + 1)$ elements and it is obtained by the vectorization transformation applied in the difference of ORMs. For example, the vectorization of a 2×2 matrix is:

$$\mathbf{A} = \begin{bmatrix} a_{11} & a_{12} \\ a_{21} & a_{22} \end{bmatrix} \Rightarrow \text{vec}\,(\mathbf{A}) = \begin{bmatrix} a_{11} \\ a_{12} \\ a_{21} \\ a_{22} \end{bmatrix}. \tag{3.7}$$

Let the dimension of $\vec{V}$ be denoted by N_{data}. For the Sirius storage ring, $\text{N}_{\text{data}} = 2 \times 160 \times 281 = 89920$. Note that $\chi^2 = \vec{V}^{\intercal}\vec{V}$.

If the relative orbit response due to the RF frequency variation $\dfrac{\Delta u_i}{\Delta f_{\text{rf}}}$ is included as a ORM column, from Eq. (3.5), the minimization problem can be factored as

$$\chi_\eta^2 = \sum_{i,j} \left(M_{ij}^{\text{measured}} - M_{ij}^{\text{model}} \right)^2 + \left(\frac{c_{f_{\text{rf}},\theta}}{\alpha f_{\text{rf}}} \right)^2 \sum_i \left(\eta_i^{\text{measured}} - \eta_i^{\text{model}} \right)^2, \tag{3.8}$$

where $c_{f_{\text{rf}},\theta}$ is a conversion factor used to match the units of χ_η terms, α is the momentum compaction factor and f_{rf} is the RF frequency.

The BPM index i covers the horizontal dispersion function for $1 \leq i \leq \text{N}_{\text{BPM}}$ and the range $\text{N}_{\text{BPM}} + 1 \leq i \leq 2\text{N}_{\text{BPM}}$ refers to the vertical dispersion. Therefore, in this way the dispersion functions are also included in the fitting.

The minimization is performed by changing some parameters in the ring model, so the model ORM $\mathbf{M}^{\text{model}}$ is also changed and the square difference χ^2, i.e., the 2-norm of the residue vector $\vec{V}$, might be reduced. Two minimization algorithms are commonly used to calculate the parameters variations that minimizes χ^2: Gauss-Newton (GN) and Levenberg-Marquardt (LM).

Suppose that each element V_k of the vector is a function of several parameters $\vec{P} = \left(P_1, \ldots, P_{\text{N}_{\text{param.}}} \right)$. The number of fit parameters is represented by $\text{N}_{\text{param.}}$. Then it is possible to calculate the linear response of the vector elements for a given change in the parameters:

$$\Delta V_k = \sum_l \frac{\partial V_k}{\partial P_l} \Delta P_l. \tag{3.9}$$

The above equation can be cast in a vectorial form as well, with $\Delta\vec{V} = \mathbf{J}\Delta\vec{P}$, where the matrix $\mathbf{J}$ is called LOCO jacobian and its elements are

$$J_{kl} = \frac{\partial V_k}{\partial P_l}. \tag{3.10}$$

The ORM can be interpreted as a jacobian as well, if the orbit distortions are viewed as a function of the dipolar kicks. So, if $u_i = u_i(\theta_1, \ldots, \theta_{\mathrm{N_{corrs}}})$, the ORM elements are $M_{ij} = \dfrac{\partial u_i}{\partial \theta_j}$. The LOCO jacobian is the derivative of the ORM relative to the parameters $\vec{P}$, thus it is actually the second order derivative of the orbit distortion relative to the dipolar kicks and the parameters, which can be written as a rank-3 tensor with elements given by:

$$J_{ijl} = \frac{\partial^2 u_i}{\partial P_l \partial \theta_j}. \tag{3.11}$$

The vectorization uses the indices (i, j) of this rank-3 tensor to convert them in one index $k = i \otimes j$ and build a rank-2 tensor J_{kl}, which is the LOCO jacobian matrix.

Depending on the parameter type, it is possible to calculate the LOCO jacobian matrix analytically or numerically. The numerical jacobian calculation typically dominates the running time for LOCO method.

3.2.1 Gauss-Newton Algorithm

The GN algorithm was already briefly presented in Section 3.1 while discussing the calculation of kicks to correct the orbit distortion. This algorithm is generally used to solve non-linear least squares problems [51].

Suppose that an ORM was measured in the real storage ring and the initial model ORM is calculated with the initial parameters $\vec{P}_0$, so the initial residue vector $\vec{V}_0$ is obtained. The goal is to apply variations in the residues such that $||\vec{V}_0 - \mathbf{J}\Delta\vec{P}||^2$ is minimized with respect to $\Delta\vec{P}$. We obtain the solution $\Delta\vec{P}_0 = -\left(\mathbf{J}^\mathsf{T}\mathbf{J}\right)^{-1}\mathbf{J}^\mathsf{T}\vec{V}_0$, so changing the parameters by $\vec{P}_1 = \vec{P}_0 + \Delta\vec{P}_0$ might reduce the 2-norm of the new residue vector $\vec{V}_1$. Since the problem is typically non-linear, proceeding in that manner iteratively, in principle the algorithm converges to the minimum of χ^2.

The LOCO jacobian matrix $\mathbf{J}$ dimension is $\mathrm{N_{data}} \times \mathrm{N_{param.}}$. The number of data points $\mathrm{N_{data}}$ is much greater than the typical number of parameters $\mathrm{N_{param.}}$. Hence, $\mathbf{J}$ is a rectangular matrix with much more rows than columns and the problem is highly over-constrained. For Sirius $\mathrm{N_{data}} = 89920$ and $\mathrm{N_{param}} \approx 1000$ for typical LOCO fittings. As discussed in Appendix B, in this overdetermined case it is not possible to solve the linear problem exactly, but the SVD method provides an approximate solution called least squares solution.

The GN method seeks for the minimum of χ^2 by iteratively applying the parameters variations, calculated in each step by

$$\Delta\vec{P} = -\left(\mathbf{J}^\mathsf{T}\mathbf{J}\right)^{-1}\mathbf{J}^\mathsf{T}\vec{V}. \tag{3.12}$$

where $\vec{V}$ is the residue vector.

It is important to mention that if the initial model ORM is far from the measured ORM, i.e., the actual and the model linear optics are very different, the algorithm may not converge due to nonlinearities. Therefore, the Gauss-Newton convergence requires a good initial model in order for the linear approximations to be valid. For the cases that a good initial guess is not available, the Levenberg-Marquardt is then introduced as a fitting option that is less dependent on the initial model.

3.2.2 Levenberg-Marquardt Algorithm

The LM algorithm is a damped least squares method. It is a combination between the GN algorithm and the gradient descent, being more robust than GN since it converges to the solution even if the initial guess is far from the final values [51].

While GN method solves the linear algebra problem given by $\mathbf{J}^{\mathsf{T}}\mathbf{J}\Delta\vec{P} = -\mathbf{J}^{\mathsf{T}}\vec{V}$ for a given residue vector $\vec{V}$, the LM method solves the modified equation[1]:

$$\left(\mathbf{J}^{\mathsf{T}}\mathbf{J} + \lambda \mathrm{diag}\left(\mathbf{J}^{\mathsf{T}}\mathbf{J}\right)\right)\Delta\vec{P} = -\mathbf{J}^{\mathsf{T}}\vec{V}, \tag{3.13}$$

where $\lambda > 0$ is a constant. The diagonal operator acts on a 2×2 matrix, for example, as:

$$\mathbf{A} = \begin{bmatrix} a_{11} & a_{12} \\ a_{21} & a_{22} \end{bmatrix} \Rightarrow \mathrm{diag}\left(\mathbf{A}\right) = \begin{bmatrix} a_{11} & 0 \\ 0 & a_{22} \end{bmatrix}. \tag{3.14}$$

Note that the diagonal elements of the matrix $\mathbf{J}^{\mathsf{T}}\mathbf{J}$ are increased by the scale $1+\lambda$. The interpolation between the GN algorithm and the gradient descent is controlled with the parameter λ. In the limit $\lambda \ll 1$, Eq. (3.13) approaches the equation used in the GN method. If $\lambda \gg 1$, Eq. (3.13) describes the gradient descent method, where the changes are made only in the direction of maximum variation of the function.

The parameter λ may be chosen in a heuristic manner for a specific problem. It also can be changed during the fitting. The typical procedure used in LOCO algorithm [1, 43] is to begin with small values for λ, around 10^{-3}, decrease λ by a factor (for example, by 10) if the iteration reduces χ^2 and increase λ by a scale if χ^2 is increased and keep increasing this parameter until χ^2 is reduced or λ reaches a maximum threshold. In this way, the methods GN and LM proceed basically in the same manner initially and in the cases that GN fails to converge, the LM may continue the convergence by changing the fitting method, making it closer to the gradient descent by increasing the value of λ. One disadvantage of the LM algorithm is that for large values of λ, the algorithm convergence is typically very slow. Therefore, once the fitting is reasonably close to the minimum, it may be helpful to decrease the value of λ for the sake of increasing the convergence speed.

[1] The method was proposed by K. Levenberg in the paper [52] originally as $\left(\mathbf{J}^{\mathsf{T}}\mathbf{J} + \lambda\mathbf{I}\right)\Delta\vec{P} = -\mathbf{J}^{\mathsf{T}}\vec{V}$. Later D. Marquardt in [53] replaced the identity matrix $\mathbf{I}$ by $\mathrm{diag}\left(\mathbf{J}^{\mathsf{T}}\mathbf{J}\right)$, making the method scale-independent.

3.3 Functionalities

LOCO can be configured for two purposes: to find the error sources or to calculate linear optics and coupling corrections. Therefore, it can be used as a diagnostic or a correction tool. In this section it will be discussed the common parameters types used and how to setup LOCO for each purpose.

3.3.1 Fit Parameters

In order to determine the type of parameters to be included in the ORM fitting it is useful to consult the sources of perturbations described in Section 2.4. The common parameters that can be varied to fit the ORM are:

- Diagonal blocks $\mathbf{M}^{xx}$ and $\mathbf{M}^{yy}$
  - quadrupolar gradients in quadrupole magnets;
  - quadrupolar gradients in dipole magnets;
  - quadrupolar gradients in sextupole magnets;
  - BPMs gains;
  - steering magnets gains.
- Off-diagonal blocks $\mathbf{M}^{xy}$ and $\mathbf{M}^{yx}$
  - skew quadrupolar gradients in skew quadrupole magnets;
  - skew quadrupolar gradients in quadrupole magnets;
  - skew quadrupolar gradients in dipole magnets;
  - skew quadrupolar gradients in sextupole magnets;
  - BPMs roll angles.

The LOCO jacobian matrix for BPMs and corrector gains, and also for BPMs roll errors, are the columns that can be calculated analytically, as shown in Appendix C. The columns related to the other parameters are typically calculated by numerical derivatives with the simulated storage ring model.

BPMs gains and rolls can be viewed as adjustments to the measurements given by these devices, mapped with a linear transformation. Suppose that the actual orbit positions in the i-th BPM are $(x_{i,\text{real}}, y_{i,\text{real}})$ but the BPM measures the values $(x_{\text{i,meas.}}, y_{\text{i,meas.}})$. The real values can be obtained by the linear transformation:

$$\begin{bmatrix} x_{i,\text{real}} \\ y_{i,\text{real}} \end{bmatrix} = \begin{bmatrix} \cos\alpha_i & \sin\alpha_i \\ -\sin\alpha_i & \cos\alpha_i \end{bmatrix} \begin{bmatrix} g_{i,x}^{\text{BPM}} & 0 \\ 0 & g_{i,y}^{\text{BPM}} \end{bmatrix} \begin{bmatrix} x_{i,\text{meas.}} \\ y_{i,\text{meas.}} \end{bmatrix}, \tag{3.15}$$

where $g_{i,x}$ are the horizontal gains, $g_{i,y}$ the vertical gains for the i-th BPM and α_i is the roll for this BPM. In that way, the BPM measurements $\vec{u}_{i,\text{meas.}}$ are adjusted to $\vec{u}_{i,\text{real}}$, rewriting Eq. (3.15) as:

$$\vec{u}_{i,\text{real}} = \mathbf{R}^{\text{BPM}}(\alpha_i)\,\mathbf{G}_i^{\text{BPM}}\vec{u}_{i,\text{meas.}}, \tag{3.16}$$

where $\mathbf{R}(\alpha_i)$ is a rotation matrix and $\mathbf{G}_i^{\text{BPM}}$ the BPM gain matrix. Eq. (3.16) allows for the jacobian matrix analytical calculation for the BPM gains and rolls, which is done in details in Appendix C.

For the steering magnets the discussion is similar. Suppose that the j-th corrector kick set in the storage ring control system is $\theta^u_{j,\text{applied}}$, $u = x$ for horizontal kicks and $u = y$ for vertical. Let $\theta^u_{j,\text{real}}$ be the actual kick applied in the electron beam. These two values may be different and can be related by a gain factor

$$\theta^u_{j,\text{applied}} = g^{\text{corr}}_{j,u}\theta^u_{j,\text{real}}. \tag{3.17}$$

The gain definition for correctors and BPMs was different in order to obtain linear analytical expressions for both jacobian matrices. Eq. (3.17) also allows for the jacobian matrix analytical calculation for the steering magnets gains, which is also done in details in Appendix C.

The jacobian matrix for the remaining parameters are calculated by numerical derivatives:

$$J_{kl} = \frac{V_k(P_l + \Delta P_l) - V_k(P_l)}{\Delta P_l}. \tag{3.18}$$

The residue vector is $\vec{V} = \text{vec}\left(\mathbf{M}^{\text{meas.}} - \mathbf{M}^{\text{model}}\right)$. For these parameters, the dependence of P_l is contained only in the model ORM: $\mathbf{M}^{\text{model}}$. The matrix $\mathbf{M}^{\text{meas.}}$ contains the data measured in the real storage ring, thus $\frac{\partial \mathbf{M}^{\text{meas.}}}{\partial P_l} = 0$. In that way, the jacobian elements are obtained by

$$J_{kl} = -\text{vec}\left(\frac{M^{\text{model}}_{ij}(P_l + \Delta P_l) - M^{\text{model}}_{ij}(P_l)}{\Delta P_l}\right), \tag{3.19}$$

remembering that the vectorization transforms the (i, j) indices in the k index.

This numerical calculation dominates the running time for LOCO, whereas for each individual parameters that is varied, the model ORM must be calculated to obtain the residue vector. The total jacobian calculation time is approximately $\Delta t_{\mathsf{ORM}} \times \text{N}_{\text{param.}}$, where Δt_{ORM} is the time required to calculate the ORM. Thus, optimizing the ORM calculation directly reduces LOCO running time.

By default, the BPMs and steering magnets gains are always included as fit parameters, both for finding errors or calculating the corrections. The reason for this is that the gains calibrations have a specific signature in the residue vector and not including the

gains would force the other parameters to compensate these systematic errors. In this case, even if the measured ORM is perfectly fitted, the adjusted parameters are unrealistic.

3.3.2 Finding Errors

The fit parameters to be included in LOCO method and its interpretation are directly related to method's goal. As discussed in Section 2.4, there are various sources of errors that perturbs the storage ring linear optics: the betatron and dispersion functions. The ORM depends on these functions, so fitting the measured ORM is fundamentally equivalent to obtain a model that represents the linear response of the real machine on the optics functions subject.

If the measured ORM is adjusted by varying in the model all the available fit parameters, then the final values of these parameters are interpreted as the deviations from ideal conditions represented by the nominal lattice, i.e., they represent the errors sources.

Let's use the fit parameters described in the previous subsection 3.3.1 as an example for discussion. If all these parameters are adjusted, their variations may be interpreted as:

- quadrupolar gradients in dipole and quadrupole magnets: differences between the expected gradients in the magnet models in the simulated magnetic lattice and the actual gradients affecting the beam;
- quadrupolar gradients in sextupole magnets: the major contribution is due to horizontal transverse alignment errors or horizontal orbit distortions in the sextupoles, leading to feed-down effects that produce normal gradients;
- skew quadrupolar gradients in quadrupole and dipole magnets: rotation errors the corresponding magnets;
- skew quadrupolar gradients in sextupole magnets: the main contribution is due to vertical transverse alignment errors or vertical orbit distortions in the sextupoles, leading to feed-down effects that produce skew gradients.

The BPM gains, rolls and the steering magnets gains interpretation is the same for the two purposes of the method. There is a question about the degeneracy between obtaining the absolute BPM and correctors gains that is addressed in section 3.4, so in principle it is only possible to obtain the relative gains. The BPMs roll angles are related to electrical coupling between the device channels and cables and rotation errors in the devices installation.

3.3.3 Correcting Errors

Finding the errors sources with LOCO method is a strategy to obtain a model representation in the computer for the real storage ring. This LOCO functionality can be used as a diagnostic tool, for example, after a machine shutdown in which there was some interventions in the storage ring. Running LOCO after a shutdown including all parameters in the fitting might show non-trivial problems in the machine that might perturb the beam. Thus LOCO analysis may point out specific errors and facilitate targeted interventions to correct them.

Among the fit parameters described in section 3.3.1, there are some parameters that cannot be directly varied in the real machine. In that way, even though the errors sources are obtained, their corrections cannot be made by simply applying the opposite variations in the machine. Therefore, to effectively correct the errors, a subset with adjustable fit parameters in the real storage ring must be used. This subset of adjustable parameters are commonly called knobs.

The knobs final variations obtained with this LOCO setup are interpreted as the effective corrections that restores the real storage ring to the nominal linear optics and symmetry. The knobs used for correction of the linear optics are the quadrupoles trim coils and the knobs used to correct the betatron coupling are the skew quadrupoles.

Suppose that LOCO provides the final values for the knobs

$$\vec{P}_{\text{final}}^{\text{model}} = \vec{P}_{\text{initial}}^{\text{model}} + \Delta\vec{P}_{\text{LOCO}}. \tag{3.20}$$

For LOCO method, the initial parameters $\vec{P}_{\mathsf{initial}}$ produce the nominal and symmetric optics functions. The final parameters $\vec{P}_{\mathsf{final}}$ correspond to the distorted linear optics, a representation to the actual optics functions in the real storage ring. To correct the actual optics function the process is inverted: the initial linear optics is distorted and, ideally, the final situation is the nominal symmetric optics functions. Therefore, the variations calculated by LOCO method is applied as corrections in the real machine with the opposite sign

$$\vec{P}_{\text{final}}^{\text{real}} = \vec{P}_{\text{initial}}^{\text{real}} - \Delta\vec{P}_{\text{LOCO}}. \tag{3.21}$$

3.4 Degeneracies

Suppose that there are two fit parameters with the same signature in the ORM, i.e., two degenerated parameters. Let P_1 and P_2 be these parameters, then the linear change in the residue vector can be written as

$$\Delta\vec{V} = \frac{\partial\vec{V}}{\partial P_1}\Delta P_1 + \frac{\partial\vec{V}}{\partial P_2}\Delta P_2 + \sum_{l\neq\{1,2\}} \frac{\partial\vec{V}}{\partial P_l}\Delta P_l. \tag{3.22}$$

If P_1 and P_2 are degenerate with respect to $\vec{V}$, in the LOCO jacobian matrix this can be seen as two columns that are linearly dependent. For example, in the extreme case that $\dfrac{\partial \vec{V}}{\partial P_2} = \rho \dfrac{\partial \vec{V}}{\partial P_1}$, where $\rho \in \mathbb{R}$ is a constant, then

$$\Delta \vec{V} = \frac{\partial \vec{V}}{\partial P_1} \Delta P_1 \left(1 + \rho \frac{\Delta P_2}{\Delta P_1}\right) + \sum_{l \neq \{1,2\}} \frac{\partial \vec{V}}{\partial P_l} \Delta P_l. \tag{3.23}$$

From Eq. (3.23) we observe that no matter how much the parameters P_1 and P_2 change, if the variations satisfy $\Delta P_1 = -\rho \Delta P_2$, the variation $\Delta \vec{V}$ is the same. If the summation part keeps generating variations that reduce the residue vector, this allows for large changes on the parameter P_1 and consequently on the parameter P_2, in the opposite direction given by $-\rho$, without increasing χ^2.

The degeneracy problem may lead to non-physical fit parameters. The effect may still be problematic to the fitting for quasi-degenerate parameters, since it may be susceptible to noise in the measured data. For the exact degeneracy case, as exemplified in the parameters P_1 and P_2, the LOCO jacobian matrix is rank deficient. In this case, as discussed in the Appendix B, the SVD provides a null singular value. For quasi-degenerate parameters, the SVD provides very small singular values, compared to the first one (the maximum). These small singular values represent directions in the parameter space where the parameters may be varied and there is no significant variation in the residue vector.

A common strategy to avoid the negative effect of degeneracies is the singular value selection. This can be done by explicitly removing the singular values in the singular matrix in the pseudo-inversion process. Alternatively, one can use a criteria that the singular values that satisfy $\dfrac{\sigma_i}{\max(\sigma_i)} < \Delta$ may be removed, for a minimum threshold Δ. Another strategy to circumvent the degeneracy problems is including constraints in the minimization problem. This will be discussed in the next section.

There is a well-known degeneracy related to the BPM and steering magnets gains. The transformation that applies the gains in the measured ORM is given by

$$\mathbf{M}^{\text{real}} = \mathbf{G}^{\text{BPM}} \mathbf{M}^{\text{meas.}} \mathbf{G}_{\text{corr}}^{-1}. \tag{3.24}$$

This transformation changes the ORM elements by $M_{ij} \rightarrow g_i^{\text{BPM}} g_j^{\text{corr}} M_{ij}$. Therefore, if the BPM gain is scaled up by $g_i^{\text{BPM}} \rightarrow \rho g_i^{\text{BPM}}$, and the corrector gain is scale down by $g_j^{\text{corr}} \rightarrow g_j^{\text{corr}}/\rho$, the ORM remains the same. That degeneracy limits LOCO to determine only the relative gains for BPMs and steering magnets. The degeneracy between BPM and correctors gains is manifested as two very small singular values in LOCO jacobian matrix SVD, one for each plane, horizontal and vertical.

Including the orbit response due to a variation in the RF frequency as a column in the ORM matrix may break the gain degeneracy. The variation in the RF frequency in

storage rings is extremely precise, so the correspondent measured orbit response contains basically only the errors related to the BPM gains. This additional column depends on the dispersion function $\eta(s)$, as can be seen in Eq. (3.5). Since ideally the vertical dispersion function is zero, including this column in the ORM may break the degeneracy between horizontal BPM and correctors gains and its absolute values may be determined. In the case that there is a substantial vertical dispersion function $\eta_y(s)$, it may be possible to determine the absolute gains for vertical BPMs and correctors as well. Actually, increasing intentionally the vertical dispersion function and performing LOCO analysis is a possible strategy to determine the absolute gains for both planes.

3.5 Constraints and Weights

The first common example where the degeneracy becomes a problem is when the fit parameters are quadrupoles. The trims coils in quadrupoles are used to correct the storage ring linear optics and the expected strengths variations required to achieve that goal are typically less than a few percent. This expectation is commonly based on magnetic measurements and alignment specifications. Thus, the fit quadrupoles variations obtained from LOCO method must be compatible to this range of values.

For compact magnetic lattices, as can be found in 4^{th} generation synchrotron light sources, some adjacent quadrupoles may be very close to each other. If the betatron phase advance between these quadrupoles is small, a localized error in one quadrupole perturbs the linear optics with a signature that is very similar to the signature generated by its neighbor. Hence, these fit parameters may be quasi-degenerate and LOCO method may fit the measured ORM by the cost of finding large variations for quadrupole's trim coils. Typically these large variations are unrealistic.

As discussed, singular values selection may be a strategy to circumvent the degeneracy problem. However, finding the best set of selected singular values may be a very heuristic and time consuming process [49]. A more effective approach is including the quadrupoles variations in the minimization problem as a constraint. In that way, the LOCO goal is fitting the measured ORM with a solution that also minimizes the quadrupoles variations.

Let the fit parameters that represents the quadrupole variation be K_q, where q is the sub-index satisfying $1 \leq q \leq \mathrm{N_{quads}}$. The constraints are included in the minimization problem by:

$$\chi_c^2 = \chi^2 + \frac{1}{\sigma_{\Delta K}^2} \sum_q \left(w_q \Delta K_q\right)^2 =: \sum_{k=(i,j,q)} V_k^2, \tag{3.25}$$

where $\sigma_{\Delta K}$ is a normalization constant, w_q are individual weights factors and χ^2 is defined in Eq. (3.6). If the dispersion function is included in the fitting, it is used χ_η^2 from Eq. (3.8)

instead. One can control the constraint on specific quadrupole variations ΔK_q by adjusting the individual weights w_q.

Let $\vec{K} = \left(K_1, \ldots, K_{\mathrm{N_{quads}}}\right)$ be the vector that represents the quadrupoles parameters. The constraint may be implemented by extending the residue vector and the LOCO jacobian matrix:

$$\vec{V}_c = \begin{bmatrix} \vec{V} \\ \vec{V}_{\Delta K} \end{bmatrix}, \tag{3.26}$$

$$\mathbf{J}_c = \begin{bmatrix} \mathbf{J} \\ \mathbf{J}_{\Delta K} \end{bmatrix}, \tag{3.27}$$

where $V_{\Delta K,q} = \dfrac{w_q}{\sigma_{\Delta K}} \Delta K_q$. From the relation $J^{\Delta K}_{q,q} = \dfrac{\partial V_{\Delta K,q}}{\partial\left(\Delta K_q\right)}$ it is obtained the matrix elements $J^{\Delta K}_{q,q} = \dfrac{w_q}{\sigma_{\Delta K}}$. Note that $\mathbf{J}_{\Delta K}$ is a block-diagonal $\mathrm{N_{quads}} \times \mathrm{N_{params.}}$ matrix, where the elements are all zero except for the $\mathrm{N_{quads}} \times \mathrm{N_{quads}}$ diagonal block.

The constrained residue vector dimension is $\mathrm{N_{data}} + \mathrm{N_{quads}}$ and new LOCO jacobian matrix dimension is $(\mathrm{N_{data}} + \mathrm{N_{quads}}) \times \mathrm{N_{param.}}$. Observe that the figure of merit can be factored as

$$\begin{aligned} \chi^2_c = \vec{V}_c^{\mathsf{T}} \vec{V}_c &= \vec{V}^{\mathsf{T}} \vec{V} + \vec{V}^{\mathsf{T}}_{\Delta K} \vec{V}_{\Delta K} \\ &= \chi^2 + \chi^2_{\Delta K}. \end{aligned}$$

It is important to mention that the vector $\Delta\vec{K}$ contains the predicted quadrupoles variations and satisfies $\vec{K}_{n+1} = \vec{K}_n + \Delta\vec{K}$, where $\vec{K}_n$ quadrupole strengths in the iteration n and $\vec{K}_{n+1}$ in the next step $n+1$. In that sense the constrained fitting problem calculates, at each iteration step, the quadrupoles changes that produce a better fit to the measured ORM and also minimize the changes themselves.

For non-zeros w_q and finite $\sigma_{\Delta K}$, the solution for $\dfrac{\partial \chi^2_{\Delta K}}{\partial\left(\Delta K_q\right)} = 0$ is $\Delta K_q = 0$ for every q, therefore the additional elements $\vec{V}_{\Delta K}$ for the residue vector must be zeros. The additional jacobian $J_{\Delta K}$ must be kept in the calculation, since it is independent of $\Delta\vec{K}$. This allows us to conclude that the ΔK constraint does not change the global minimum, since $\chi^2_c = \chi^2$ and the problem dimension is unchanged. On the other hand, the constraint does change the convergence path, allowing for a convergence with smaller step sizes.

The constrained version for the GN method calculates the parameters variations $\Delta\vec{P}$ by solving

$$\mathbf{J}_c^{\mathsf{T}} \mathbf{J}_c \Delta\vec{P} = -\mathbf{J}_c^{\mathsf{T}} \vec{V}_c, \tag{3.28}$$

since $\mathbf{J}^{\mathsf{T}}_{\Delta K} \mathbf{J}_{\Delta K}$ is diagonal and $\vec{V}_{\Delta K} = \vec{0}$, it is obtained that

$$\left(\mathbf{J}^{\mathsf{T}}\mathbf{J} + \mathrm{diag}\left(\mathbf{J}^{\mathsf{T}}_{\Delta K}\mathbf{J}_{\Delta K}\right)\right) \Delta\vec{P} = -\mathbf{J}^{\mathsf{T}}\vec{V}. \tag{3.29}$$

Observe that the ΔK constraints modify the GN method with the same mathematical structure used in the LM method. The main difference is that the constraints include a gradient-descent component in the parameters ΔK, while the LM method inclues that component in all directions given by the columns of $\mathbf{J}$. The importance of the constraint component to the fitting is controlled by the magnitude of $\mathbf{J}_{\Delta K}$, i.e., by the constraint weights w_q and the normalization factor $\sigma_{\Delta K}$.

The diagonal elements added in $\mathbf{J}^\mathsf{T}\mathbf{J}$ by the constraints and by the LM contribution are manifested as a regularization for small singular values in the SVD decomposition [1], which is necessary for the pseudo-inversion of $\mathbf{J}^\mathsf{T}\mathbf{J}$. The pseudo-inversion in the GN method calculates parameters variations that depends on terms $1/\sigma_i$, where σ_i is a singular value. If $\mathbf{J}^\mathsf{T}\mathbf{J}$ is rank deficient, there are null or very small singular values, thus $1/\sigma_i$ may be a very large number and the parameters calculation may be problematic. The singular values regularization substitutes $1/\sigma_i$ by $\sigma_i/\left(\sigma_i^2+\lambda_i^2\right)$, thus it may prevent the small singular values damage by an appropriated choice for the factors λ_i. When $\lambda_i=\sqrt{\lambda}$ for every i, the regularization is related to the non-scaled LM factor λ, where $\mathbf{J}^\mathsf{T}\mathbf{J}$ is modified to $\mathbf{J}^\mathsf{T}\mathbf{J}+\lambda\mathbf{I}$.

From Eq. (3.29), it can be seen that the constraints can be implemented by keeping unchanged the jacobian matrix $\mathbf{J}$ and the residue vector $\vec{V}$, but adding only the contribution $\mathbf{J}_{\Delta K}^\mathsf{T}\mathbf{J}_{\Delta K}$ to the parameters calculations. Since the constraints do not change the minimization problem dimension, maintain the jacobian and the residue vector dimensions while applying the constraint is conceptually more appropriated. In that way, the LM method with constraints determines $\Delta\vec{P}$ solving the following problem

$$\left(\mathbf{J}^\mathsf{T}\mathbf{J}+\lambda\mathrm{diag}\left(\mathbf{J}^\mathsf{T}\mathbf{J}\right)+\mathrm{diag}\left(\mathbf{J}_{\Delta K}^\mathsf{T}\mathbf{J}_{\Delta K}\right)\right)\Delta\vec{P}=-\mathbf{J}^\mathsf{T}\vec{V}, \tag{3.30}$$

and in the limit $\lambda=0$, the LM and GN methods coincide again.

Adding constraints on the parameters variations and using the LM method provide a convergence path with small step sizes, but for different reasons. The constraints limit the step sizes by construction and the LM method calculates variations in the direction that reliably minimizes χ^2 (the negative gradient direction), which also are typically small changes.

The minimization problem in LOCO method can be adapted to use other types of weights factors too. The weights in BPMs and steering magnets are applied in the same manner that the gains. Let $\vec{W}^{\mathrm{BPM}}$ and $\vec{W}_{\mathrm{corr}}$ be the weight vectors, whose elements are w_i^{BPM} and w_j^{corr}, respectively, where $1\leq i\leq 2\mathrm{N_{BPM}}$ and $1\leq j\leq \mathrm{N_{CH}}+\mathrm{N_{CV}}+1$. The weights are inserted in the minimization problem by the transformation

$$M_{ij}\rightarrow w_i^{\mathrm{BPM}}M_{ij}w_j^{\mathrm{corr}}, \tag{3.31}$$

applied in the model and measured ORMs. The weights change the residue vector and consequently the LOCO jacobian matrix as well, as derived in Appendix C.

A common weight used for the BPMs is the following. Suppose that $w_i^{\mathrm{BPM}} = 1/\sigma_i^{\mathrm{BPM}}$, where σ_i^{BPM} is the measured noise level for the i-th BPM. With this weight, the minimization problem is:

$$\chi^2 = \sum_{i,j} \left(\frac{M_{ij}^{\mathrm{measured}} - M_{ij}^{\mathrm{model}}}{\sigma_i^{\mathrm{BPM}}} \right)^2 . \tag{3.32}$$

This was the original figure of merit proposed by the author in [34]. The ideia behind including these weights is that data obtained with BPMs with larger measurement noises should be less important to the fitting.

The correctors weights can be used mainly to control the importance of the dispersion function in the fitting. This is done by changing the value of the last element of $\vec{W}^{\mathrm{corr}}$. Since the last column in the ORM corresponds to the RF frequency orbit response, changing the last corrector weight denoted by w_η changes the minimization problem in Eq. (3.8), where the dispersion contribution to the figure of merit is then multiplied by the factor w_η.

One can use a combination of BPM and correctors weights to prioritize the certain parts of the ORM. For example, if the first $\mathrm{N_{BPM}}$ weights in $\vec{W}^{\mathrm{BPM}}$ and the first $\mathrm{N_{CH}}$ weights in $\vec{W}_{\mathrm{corr}}$ are set to be larger than the remaining weights, the horizontal block $\mathbf{M}^{xx}$ dominates the LOCO fitting. Other three independent combinations of weights can be performed to increase the importance of each block $\mathbf{M}^{yy}$, $\mathbf{M}^{xy}$ or $\mathbf{M}^{yx}$.

3.6 Code Implementation for Sirius

This section is dedicated to the discussion about LOCO method implementation for Sirius storage ring, using Python as the programming language. Some tests were performed to check the reliability of the implemented code and also to understand the particularities related to the application on Sirius. The results are presented in Appendix D.

3.6.1 Accelerator Physics Codes

The Python frameworks mentioned in Section 1.5 for the accelerator physics studies are related to the accelerator modelling, the so-called tracking simulations and optics calculations. The corresponding packages developed and currently used by the LNLS APG are described as follows.

PyModels: Python modelling for the accelerator where each element is defined with several properties: device type (magnet, diagnostic, etc), length, strength, pass method, etc. The element pass method is the rule that the tracking code uses to evolve in time the particle's phase-space coordinates. The code access is open and it contains

versions for the models of Sirius accelerators: LINAC, transport lines, booster and storage. ring [54]

TrackCpp: tracking code implemented in C++ language. Together with the accelerator model, this library can be used to study the single particle dynamics numerically. Each lattice element can be represented by the on-linear map $\mathcal{T}(s|s_0)$ that affects the particle coordinates $\vec{r}_0 = (x_0, x'_0, y_0, y'_0, z_0, \delta_0)$ at s_0 by changing the coordinates to $\vec{r} = \mathcal{T}(s|s_0)\vec{r}_0$. The map approach[2] is extremely useful for numerical calculations and its linearized form takes advantage on linear algebra conveniences, for example the fact that the transformation compositions are translated simply as matrix multiplications. For circular accelerators, the whole lattice transformation, called the one-turn map, is very useful for deriving global lattice properties, verify long-term stability conditions, obtain fixed points for the map, etc. The one-turn map may include only the linear contributions or non-linear effects. In TrackCpp, explicit symplectic integrators are applied to approximate the solutions of the equations of motions for the particles in the lattice in a systematic way. TrackCpp is an open-source code developed in-house and based on Tracy [55]. The code can be accessed in [56].

PyAccel: Python integration between the accelerator modelling in PyModels and the structures and calculations implemented in TrackCpp. The package provides the interface to obtain the optics functions and the results of particle tracking performed in TrackCpp. With PyAccel the equilibrium parameters (emittance, bunch length, beam sizes, lifetime, etc.) are calculated with analytical expressions for a given accelerator model. With this package it is also possible to manipulate the models, setting and getting the elements properties. The open code can be accessed in [57].

Since PyAccel can be seen as a "high-level" interface for the calculations performed in the background by TrackCpp, the accelerator physics simulations are conducted with the combined use of PyModels and PyAccel packages.

3.6.2 Orbit Response Matrix Calculation

LOCO method requirements are basically a simulated model for the accelerator and a framework to perform the ORM calculations in the model. The numerical tools required for LOCO, such as matrix multiplications and SVD, are all covered by NumPy [58], a Python package largely used in scientific computing.

PyModels provides the accelerator modelling for Sirius storage ring and the ORM calculation was already implemented by LNLS APG, where the transfer matrices between

[2] Regarding the linear dynamics, the correspondence between the matrix formalism (linearized maps) and the analytical description presented in Chapter 2 was developed by Courant & Snyder in [48].

Table 3 – Fit parameters used in LOCO for Sirius storage ring.

Fit parameter	# of elements
Normal quadrupole gradient	270
H. BPM gain	160
V. BPM gain	160
H. Corrector gain	120
V. Corrector gain	160
Skew quadrupole gradient	80
BPM roll angle	160
Total	1110

BPMs and correctors are used to obtain the corresponding ORM elements. This approach assumes linearity, which is typically a good approximation for small variations in the correctors kicks and orbit distortions. The ORM calculation from the transfer matrices also has the advantage of being fast: it takes about 500 ms to obtain the Sirius storage ring ORM on the computers used by LNLS APG.

3.6.3 LOCO Implementation in Python

Currently the LOCO code for Sirius is a Python package. This package is imported in a Python script that gathers the necessary input data, starts the fitting process and saves the output. At the time of writing, this script was executed via terminal. The detailed implementation of LOCO Python package is completely open for access in its GitHub Repository website [59]. A functional and tested code version was obtained during this master's work, however the LOCO code is susceptible to changes and improvements based on the experience acquired during the application in Sirius commissioning and machine studies. The upcoming versions will be constantly updated in the website [59], open to the community access.

The LOCO implementation in Python realized by the author follows the pseudo-algorithm described in Algorithm 1 that can be found in Appendix E. When the LM minimization method is used, there is an inner loop to deal with the parameter λ for the case of χ^2 reduction failure. This LM loop is described in Algorithm 2, also in Appendix E.

The fit parameters that have been used in regular LOCO analysis performed in Sirius storage ring are organized in Table 3. The first 5 parameters refer to the fitting of ORM diagonal blocks, related to the linear optics. The remaining 2 fit parameters between horizontal lines are related to ORM off-diagonal blocks adjustment, which correspond to the linear coupling errors. Typically complete matrix is included in the fitting, thus the total number of fit parameters for LOCO in Sirius Storage ring is 1110.

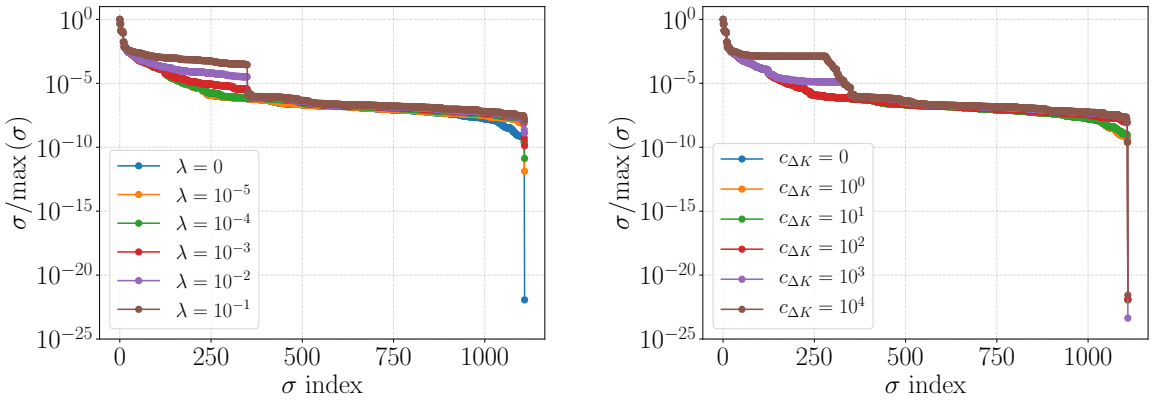

(a) Levenberg-Marquardt. (b) ΔK constraint, $c_{\Delta K} = w_{\Delta K}/\sigma_{\Delta K}$.

Figure 7 – Effect of LM method and ΔK constraint on singular values of LOCO jacobian matrix.

3.6.4 Jacobian Matrix Analysis

Based on the discussion made in Section 3.4, the singular matrix analysis provided by SVD of LOCO jacobian matrix may shed some light on the degeneracies of the problem.

The complete LOCO jacobian matrix was calculated for the Sirius storage ring, producing a 89920×1110 matrix. From Eq. (3.30), given a residue vector $\vec{V}$, one can calculate the fit parameters with

$$\Delta\vec{P} = -\left(\mathbf{J}^{\mathsf{T}}\mathbf{J} + \lambda \mathrm{diag}\left(\mathbf{J}^{\mathsf{T}}\mathbf{J}\right) + \mathrm{diag}\left(\mathbf{J}_{\Delta K}^{\mathsf{T}}\mathbf{J}_{\Delta K}\right)\right)^{-1}\mathbf{J}^{\mathsf{T}}\vec{V}.$$

From this expression, it can be seen that the SVD must be applied in two matrices: $\mathbf{J}$ for the case of singular value selection and $\mathbf{J}^{\mathsf{T}}\mathbf{J} + \lambda \mathrm{diag}\left(\mathbf{J}^{\mathsf{T}}\mathbf{J}\right) + \mathrm{diag}\left(\mathbf{J}_{\Delta K}^{\mathsf{T}}\mathbf{J}_{\Delta K}\right)$ in order to also apply the singular value selection but, most importantly, to obtain its pseudo-inverse. The minimization method to calculate the parameters is controlled by the parameter λ: if $\lambda = 0$ the GN method is used and if $\lambda \neq 0$, the LM is chosen.

The matrix $\mathbf{J}_{\Delta K}$ is a diagonal matrix with elements given by $\vec{c}_{\Delta K} = \vec{w}_{\Delta K}/\sigma_{\Delta K}$, where $\vec{w}_{\Delta K}$ is the weight vector for the ΔK constraint. Controlling the values of $\vec{c}_{\Delta K}$ one controls the constraints importance in the problem. The unconstrained case is obtained with $\vec{c}_{\Delta K} = \vec{0}$.

To study the LOCO jacobian matrix, SVD was applied in the matrix $\mathbf{J}^{\mathsf{T}}\mathbf{J} + \lambda \mathrm{diag}\left(\mathbf{J}^{\mathsf{T}}\mathbf{J}\right) + \mathrm{diag}\left(\mathbf{J}_{\Delta K}^{\mathsf{T}}\mathbf{J}_{\Delta K}\right)$ for several values of λ and $c_{\Delta K}$, independently. The results are shown in Figure 7, where the singular values were normalized by the maximum value and plotted in log scale.

The jacobian matrix in this analysis includes the RF response elements, i.e., the horizontal dispersion function is included, so the very low singular value $\sim 10^{-21}$ for $\lambda = 0$ is related to the degeneracy between the vertical BPMs and correctors gains. With

$\lambda = 10^{-5}$ this low singular value is already increased to $\sim 10^{-12}$ and the decreasing singular values around 10^{-9} in the blue line are also raised.

In the literature [9,43], it is recommended to start the fitting with $\lambda = 10^{-3}$. From Figure 7a it can be seen that this value raises the singular value at the low end. Increasing λ even further raises most of the singular values. Therefore using $\lambda = 10^{-3}$ should prevent the problems related to the low singular values while greater values for λ produce changes in the singular values that may slow the solution convergence.

Figure 7b shows the singular values for several constraint magnitudes. The weight vector was set as unity for every element and the normalization constant $\sigma_{\Delta K}$ was changed from 0 to 10^{-4}. The case $c_{\Delta K} = 0$ coincide with $\lambda = 0$ in the Figure 7a. The normalization $\sigma_{\Delta K}$ can be interpreted as the limit of step variation in ΔK. The typical values for the quadrupole gradients in Sirius storage ring are on the order of 10^{-2}. Then setting the constraint on step size to $\Delta K \sim 10^{-2}$ does not really limits the gradients variations and this can be seen in the similar singular values distributions for $c_{\Delta K}$ from 0 to 10^2. Only with $c_{\Delta K} = 10^3$ the changes in singular values are substantial. Notice that some singular values at low end are also raised with the ΔK constraints, these low singular values are related to the quasi-degeneracies between quadrupoles that may lead to large excursions in quadrupole gradients when no constraints are used.

Limiting too much the ΔK step variation may increase unnecessarily the number of iterations required for LOCO convergence. Hence, in the literature [9, 43] it is recommended to use the maximum value of $\sigma_{\Delta K}$ that still produces a significant change in the singular values, aiming to balance the ΔK constraints and the number of iterations, therefore reducing LOCO running time whenever it is worth it. For Sirius storage ring, the optimum value was determined to be $\sigma_{\Delta K} = 10^{-3}$, thus $c_{\Delta K} = 10^3$.

Notice that with $c_{\Delta K} = 10^3$ the last singular value was relatively smaller compared to the unconstrained case. This can be solved by combining the constrained case with the LM minimization, given that it was seen that the LM contribution raises the singular values. The singular values distribution for the chosen values of λ and $c_{\Delta K}$ compared to the original distribution are shown in Figure 8. The last singular value is associated with the gain degeneracy between vertical BPMs and correctors, so, in principle, it is the only singular value that should be removed.

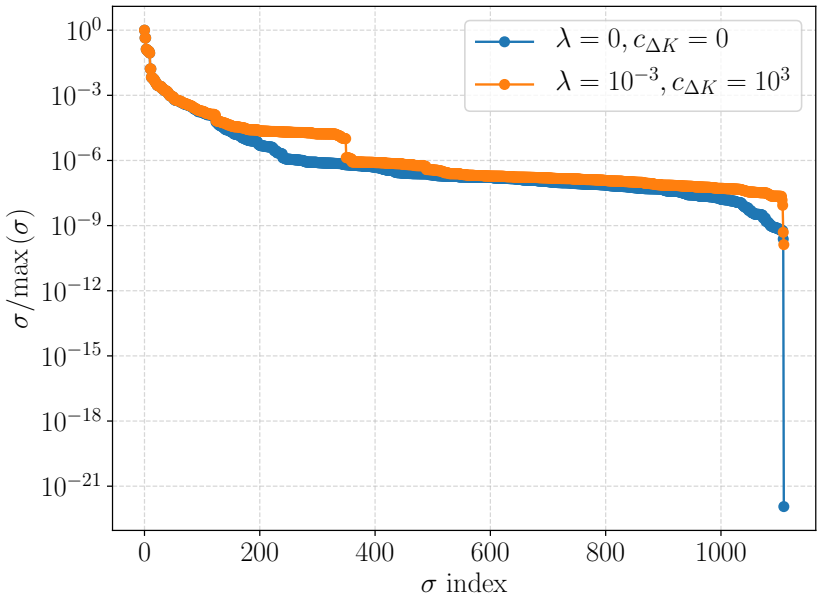

Figure 8 – Singular values distributions between GN unconstrained method and LM constrained method with chosen parameters.

4 Applications on Sirius Storage Ring

This final chapter is dedicated to the application to Sirius storage ring of the theory and the code presented and discussed in the previous chapters.

During the Sirius commissioning in 2020, the implemented LOCO code had already been proven to be useful to correct Sirius linear optics and coupling, improving the machine performance. The optics and coupling corrections obtained with LOCO method also contributed for smooth operation recoveries after five IDs installations. Only the ID installed in a high-beta section required localized gradients compensation of 0.5 % for the defocusing quadrupoles (QDA). The IDs installed in low-beta sections did not perturb the storage ring in a level that could be measured.

A few tests were performed with measured ORMs using the electron beam in the storage ring and they are reported in Section 4.1. The stored current used during the measurements was around 10 mA, which is a value that provides a good accuracy for BPM readings and the beam stability is guaranteed as well.

The studies reported in this chapter were performed in a philosophy of scientific case. The main objective is, starting from a storage ring without any optics and coupling corrections, iteratively perform LOCO procedure and apply the calculated corrections until convergence is reached. The results from this process are presented and discussed in Section 4.2. From this point, independent optics and coupling measurements were performed to characterize the storage ring before and after the corrections to determine how much the study improved Sirius parameters and performance towards the expected values. Section 4.3 is dedicated to this part.

The ORM measurement procedure was controlled by SOFB, the same software that drives the orbit correction. Both horizontal and vertical kicks variations used for the measurements were $\Delta\theta_x = \Delta\theta_y = 15\,\mu\text{rad}$ and the variation in RF frequency was $\Delta f_{\text{rf}} = 80\,\text{Hz}$. These variations are intermediate in the sense that they provide a compromise between sufficient orbit distortion for accurate BPM measurements and also keep variations small enough to avoid non-linear effects. Nominally, the peak orbit distortions at BPMs for these corrector variations are $\Delta x = 196\,\mu\text{m}$ and $\Delta y = 134\,\mu\text{m}$. The peak horizontal distortion for the variation in RF frequency is $\Delta x = 38\,\mu\text{m}$. The ORM typical measurement time for Sirius storage ring is 25 minutes.

Sirius storage ring status when these studies were performed was: four undulators were installed, one in a high-beta section and three in low-beta sections; the BBA procedured was applied to obtain BPMs offsets relative to quadrupoles centers and these offsets

were used as the target orbit for orbit correction. The standard deviation (std) of residual orbit obtained in both planes was around 30 µm. During commissioning, operating the machine with nominal betatron tunes ($\nu_x = 49.096$ and $\nu_y = 14.152$) produced a very low injection efficiency (less than 10%). After scanning the tunes, the values that provided a better injection efficiency were $\nu_x = 49.075$ and $\nu_y = 14.134$. Therefore, tunes close to these values were used throughout the commissioning and this study as well. Nevertheless, without optics and coupling correction the injection efficiency was only 20% on average, with large pulse-by-pulse variations.

4.1 Tests with Measured Data

A few tests were performed with data measured in the actual storage ring to check the method reliability in practice as well. Moreover, some tests allowed to confirm the code setup, related to the minimization method and constraints on quadrupoles variations. The tests also provided information about random errors of fit parameters.

The beam orbit was measured with BPMs during 10 s with a measurement rate of 25 Hz. The average variation obtained for each plane was $\sigma_{\mathrm{BPM},x} = (0.162 \pm 0.006)$ µm and $\sigma_{\mathrm{BPM},y} = (0.233 \pm 0.007)$ µm. These values represent the noise level of positions measurements provided by BPMs in Sirius storage ring. This means that even if the machine matched the model perfectly, this level of discrepancy in the ORM residue is expected.

4.1.1 Relevance of Constraints

From tests with simulated model and jacobian matrix analysis discussed in Subsection 3.6.4, the chosen LOCO configuration was: 1) include the parameters presented in Table 3 in the fitting, 2) use LM method as the minimization algorithm setting initially $\lambda = 10^{-3}$, 3) use the ΔK constraints with weight $c_{\Delta K} = 10^3$, 4) remove only the last singular value for pseudo-inversion of LOCO jacobian matrix.

In order to check if this setup is appropriated for LOCO analysis in the actual Sirius storage ring a simple test was performed. Without any optics or coupling corrections applied in the storage ring, an ORM was measured and it was used to apply LOCO fitting with two setups: without any modification (using GN method and no constraint on ΔK) and with the chosen configuration. The initial χ for the measured ORM was 24.6 µm and for both LOCO fittings, χ converged to values close to 0.9 µm. However there is a great difference between the two calibrated models regarding the quadrupole deviations from the nominal values. As discussed in Chapter 3, without constraints on ΔK, the LOCO process tries to minimize χ without any concern on the quadrupoles deviations magnitudes, which may lead to large excursions in these parameters due to the quasi-degeneracies in LOCO jacobian. With constraints on ΔK, the convergence path for χ is

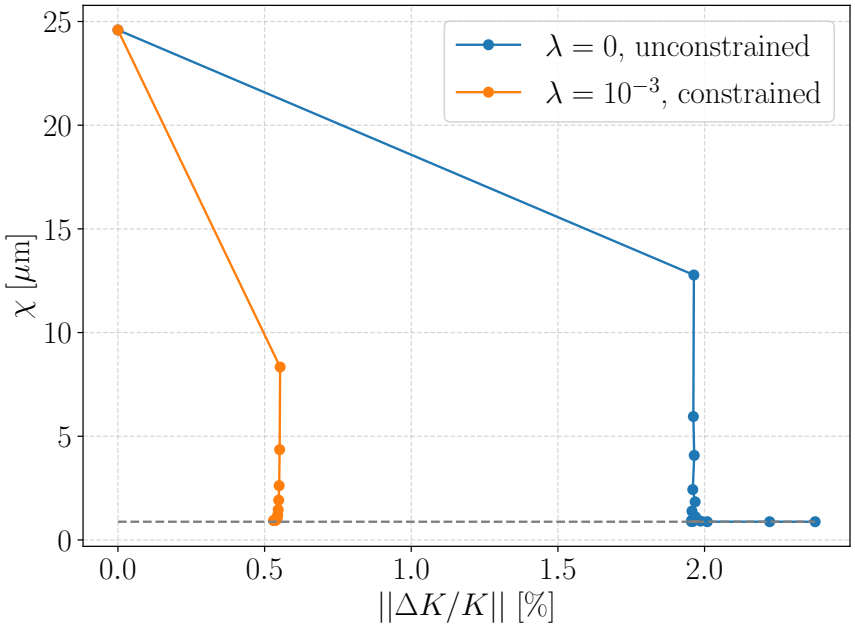

Figure 9 – χ versus $||\Delta K/K||$ throughout 10 LOCO iterations. The gray dashed horizontal line corresponds to $\chi = 0.91$ µm, the value used as reference for convergence.

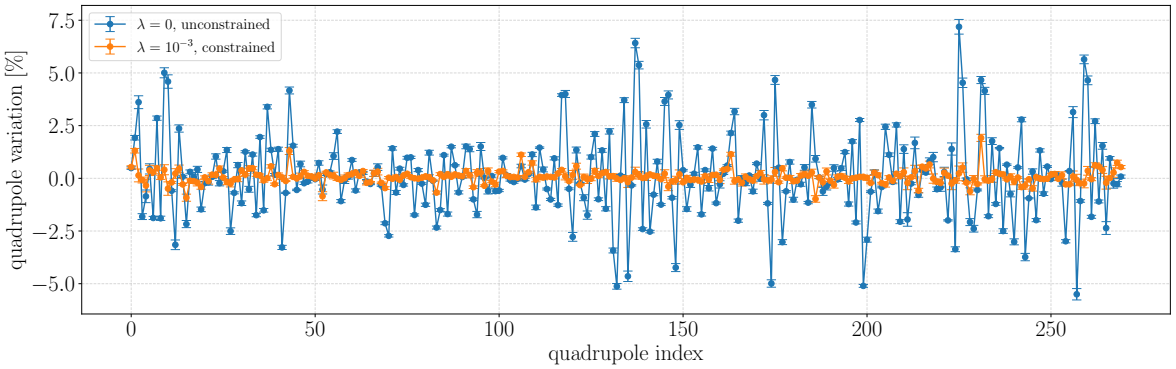

Figure 10 – Comparison of quadrupoles variations obtained from LOCO with two calculation methods.

changed in order to minimize the step size of quadrupole deviations. This difference in the fitting behavior can be revealed with a plot of χ versus the std of quadrupole changes over iterations, as presented in Figure 9. The comparison of final fit variations for the 270 quadrupoles in Sirius storage ring in this test is plotted in Figure 10.

Previous magnetic measurements and characterizations indicate a good gradient field quality for quadrupoles, satisfying the specification of 0.05 % in gradient errors. Moreover, it can be seen that some adjacent quadrupoles have large variations with opposite signs, which are related to the quasi-denegeracies discussed in Section 3.4. Nevertheless, the large quadrupoles variations represented in Figure 10 were applied in the storage ring and, after that, it was observed that the errors of measured optics parameters were

actually increased. This is a strong evidence that the large variations reaching 7.5 % are unrealistic. The solution obtained with constraints demands much less of quadrupole variations and also adjusts the measured ORM in the same level. Applying the quadrupole variations obtained with constraints resulted in positive effects on the storage ring optics. The variations obtained for the other fit parameters included in the fitting agree for the two setups within the error bars, which was expected since basically the major difference is related to the constraints on quadrupoles strengths.

It is important to point out that the convergence criteria for χ should avoid the cases of over-fitting. In addition to spare LOCO running time, the most important reason is to prevent the method from increasing the quadrupoles strengths to produce a negligible reduction in χ. In Figure 9 it can be seen that for the unconstrained case, the last three iterations increased $||\Delta K/K||$ considerably while χ was basically the same. The over-fitting is more serious for the unconstrained case indeed, since each iteration may produce large variations on quadrupoles but it may also be a problem even for the constrained case, since accumulated small step sizes may also produce large and unnecessary variations in the final values. The convergence criteria can be controlled by defining a minimum acceptable change in the residue, given by χ_{step}, and a minimum level for the residue, given by χ_{min}. For LOCO fittings performed in Sirius storage ring, the values used was $\chi_{\text{step}} = 0.01\,\mu\text{m}$ and $\chi_{\text{min}} = 0.25\,\mu\text{m}$, where the value for χ_{min} was defined based on Sirius BPMs accuracy. The final residue of $0.91\,\mu\text{m}$ obtained in these fittings is still 3.6 times larger than the BPM accuracy and a possible explanation for this limit of convergence will be discussed in Section 4.4. Nevertheless, a calibrated model with an ORM that agrees with the measured in the sub-μm level typically corresponds to a good fitting [34].

4.1.2 Random Errors

As mentioned in [34]: "*the easiest way to determine how much the set of fit parameters vary due to random errors in the measurements is simply to measure many ORM, analyze each one separately, and see how much variation there is between fit parameters for the different data sets*". Therefore, to access the random errors associated with the fit parameters presented in Table 3, the aforementioned procedure was applied in Sirius storage ring, where 10 ORMs were measured sequentially.

LOCO analysis was performed in these 10 measured ORMs with the configuration described in Subsection 4.1.1 and the results are organized in Table 4 with the root-mean-square (rms) variations. The average initial residue for these 10 realizations was $\chi_{\text{initial}} = (9.2 \pm 0.4)\,\mu\text{m}$ and after the convergence the average final residue was $\chi_{\text{final}} = (1.04 \pm 0.02)\,\mu\text{m}$. For each fit parameter, the std variation obtained in the set of 10 LOCO realizations was used to define the corresponding error bars. For each calibrated model obtained with LOCO, the lattice functions and its variations in this set of 10 values were

Table 4 – Variations in fit parameters from LOCO analysis of 10 ORM measurements performed in Sirius storage ring.

Parameter	mean rms	rms variation	Unit
Quadrupole Relative Strength	0.17	0.13	%
H. BPM Gain	96.5	0.2	%
H. Corrector Gain	92.4	0.6	%
V. BPM Gain	96	4	%
V. Corrector Gain	94	4	%
Skew Quadrupole Strength	$7.5 \cdot 10^{-4}$	$3.4 \cdot 10^{-4}$	m^{-1}
BPM roll angle	3.1	0.8	mrad

Table 5 – Variations in lattice functions obtained from LOCO calibrated models from 10 ORM measurements performed in Sirius storage ring.

Lattice function error	mean rms	rms variation	Unit
$\Delta\beta_x/\beta_x$	0.8	0.5	%
$\Delta\beta_y/\beta_y$	0.5	0.4	%
$\Delta\eta_x$	2.5	0.5	mm
$\Delta\eta_y$	12.6	1.6	mm

also calculated. The results are organized in Table 5[1].

The variations for dispersion function are calculated as absolute values because η_x is zero in the straight sections, so the division to obtain a finite relative variation is not possible. In the case of betatron functions, which always assume positive values by definition, it is possible to obtain the relative variations.

4.1.3 Initial Condition Dependence

The ORM fitting for Sirius storage ring with LOCO can be viewed as finding a minimum of a function $\chi\left(\vec{P}\right)$ with 1110 variables, the fit parameters. A strategy to explore the topology of local minima in the solution space is beginning the fitting with different initial conditions and then check the final solution obtained. If the final results are fairly independent on the initial guess, one has an indicative that, at least inside the region covered by the initial guesses range, the obtained solution is the best minimum. For a given problem, if the initial guesses cover a broad range of feasible values for fit parameters, this process indicates that, amongst the doable solutions, the found solution is the best one.

The initial condition dependence test was applied in LOCO code. An ORM mea-

[1] The initial χ and the values for normal and skew quadrupoles variations in Table 5 are relatively low because this repeatability test was performed after the LOCO corrections application to the storage ring.

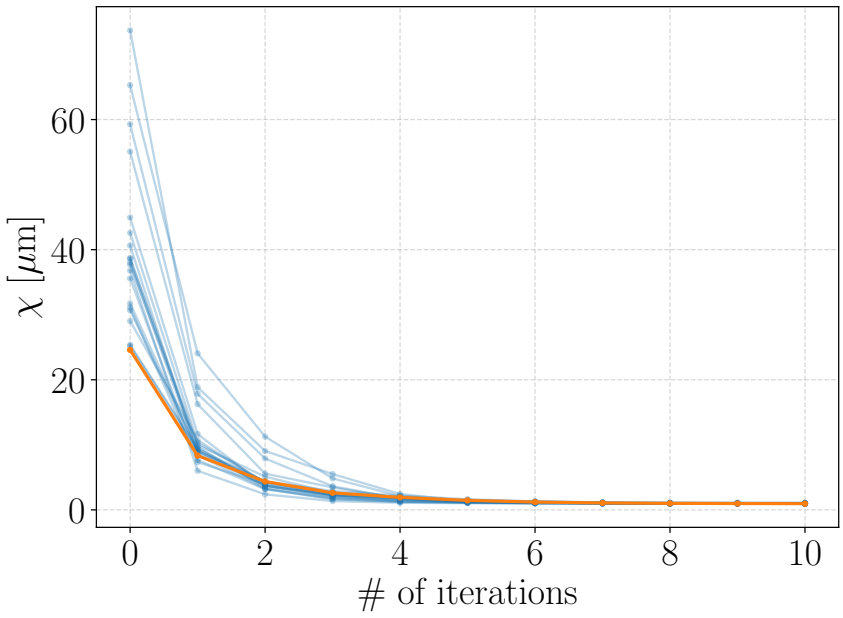

Figure 11 – χ convergence for different initial conditions. The zero initial guess convergence is represented by the orange curve.

sured in Sirius storage ring was used as input for LOCO fitting. Twenty different initial conditions, regarding only the quadrupole strengths, were used to adjust the measured ORM. The initial guesses varied with a random normal distribution with $\sigma = 0.5\%$ and one σ cutoff, with respect to the nominal gradients. Larger values of σ were tested but they produced unstable dynamics in the model or, for the stable cases, the algorithm did not converge. Thus 0.5% was chosen since it allowed for the largest feasible initial conditions.

All the 20 initial conditions produced a greater initial χ as compared to the nominal initial guess. The minimum initial χ was 25.2 µm while with zero initial condition it was 24.6 µm. The χ convergence for all the 20 realizations and the zero initial guess are plotted in Figure 11. The initial χ in this test was (47 ± 28) µm and after 10 iterations, the final was (0.98 ± 0.07) µm. Therefore, all the realizations converged to the same fitting level.

Figure 12 shows the gradient solutions obtained with these 20 different initial conditions and the solution obtained with zero initial guess as well. The relative variations were calculated comparing the final results with the nominal strengths. Although the initial spread in gradients was 0.5%, the final spread in the fitted solutions is 0.2%. The spread in the obtained solution by varying the initial conditions are within the fit parameters error bars. Moreover, the correlation between the mean of solutions and the solution obtained with zero initial guess was 98.5% and the std difference is only 0.06%. For the realizations individually, the maximum and minimum correlations was 90% and 71%, respectively. With this test, one can conclude that the solution obtained with the

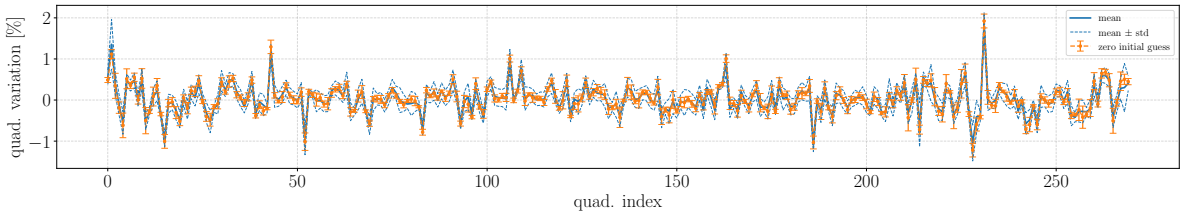

Figure 12 – Quadrupoles variations for 20 different initial guesses compared to zero initial condition.

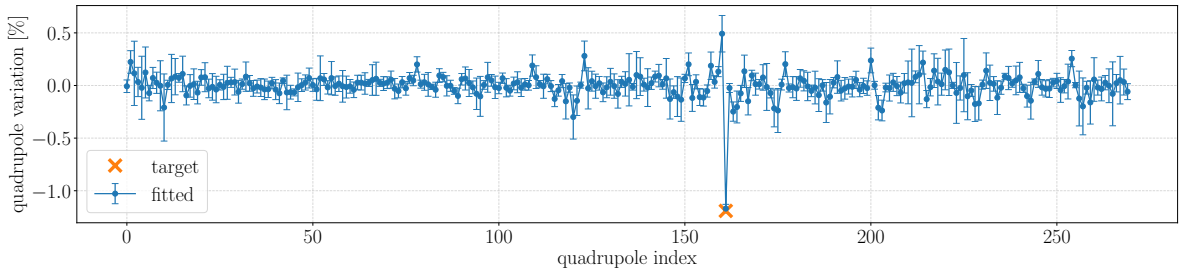

Figure 13 – Difference between quadrupole variations obtained from two ORM fittings, one ORM measured with an intentional change in the 161$^{\text{th}}$ quadrupole and the other ORM measured without it.

nominal model as the starting point (zero initial guess) is fairly independent of initial conditions. Therefore, given the explored range in the solutions space with random initial conditions, this solution is the unique local minimum.

4.1.4 Finding Planted Error

There is another insightful test, suggested and performed in [34], with the goal of showing that quadrupole gradients can be accurately predicted with LOCO method. The test is quite simple: measure an ORM, then change an individual quadrupole strength (in the case of Sirius, change the current of a trim-coil) and re-measure the ORM. Each ORM is adjusted with LOCO and the difference between the two sets of fitted quadrupole gradients should reveal the intentional change.

The test was also performed in Sirius storage ring. The trim-coil current of a QFA quadrupole was varied to produce a -1.19% change in its gradient strength. This quadrupole is placed in a high-beta straight section. Following the quadrupoles ordering around the storage ring, this corresponds to the 161$^{\text{th}}$ quadrupole out of 270. Figure 13 shows the test results.

The target gradient error in the 161$^{\text{th}}$ quadrupole was -1.19%. With LOCO, it was found a $(-1.17 \pm 0.09)\,\%$ variation in this quadrupole. Using the 3σ as the criteria for detecting outliers, one could also state that the 0.5% variation in the 160$^{\text{th}}$ quadrupole

is another possible intentional change. This indicates that there is a residual degeneracy between adjacent quadrupoles that the ΔK constraints could not eliminate completely. Even so, the change in the 161^{th} quadrupole stands out as a 13σ variation. From this test, it can be concluded that LOCO analysis can accurately predict the quadrupole gradient errors in Sirius storage ring.

4.2 Optics Correction with LOCO

After several tests to check the reliability of LOCO code and to define the fitting setup, the method was finally used to fit the measured ORM, calculate the necessary corrections and apply them in Sirius storage ring normal quadrupole trim-coils and skew quadrupoles. The process was repeated until measured and nominal ORM coincide in a satisfactory level.

The first ORM was measured in Sirius storage ring with a 10 mA stored electron beam and the orbit corrected to the BBA orbit. The operation tunes were around $\nu_x = 49.07$ and $\nu_y = 14.13$, the quadrupole trim coils and skew quadrupoles currents were all set to zero. LOCO fitting was performed, starting from the nominal model to obtain the fit parameters presented in Table 3 that best explain the measured ORM. Since the aforementioned tunes provide a better injection efficiency, it was decided that LOCO corrections should not move the measured tunes towards the nominal values. Therefore, the nominal model used as the initial model for LOCO had its betatron tunes shifted to match the measured values. In this way, the gradient variations should keep the tunes unchanged.

Based on previous tests performed with measured data, it was observed that only including the orbit response related to RF frequency variation in the ORM, i.e., including the dispersion function in the fitting, was not sufficient to produce the correspondence between predicted and measured dispersion functions, both horizontal and vertical. The conversion factor of Eq. (3.8) used was $c_{f_{\text{rf}},\theta} = \Delta f_{\text{rf}}/\Delta\theta = 80\,\text{Hz}/15\,\mu\text{rad}$. It was necessary to include a weight factor of 2 in the dispersion term to obtain a better fitting of the measured dispersion. In principle, if optics distortions are caused solely by gradient errors on quadrupoles, once the measured ORM is adjusted with the model, i.e., the beta function and phase advances in BPMs and correctors are fitted, the predicted dispersion function from this model should be very close to the measured dispersion. The need for this weight on dispersion is important and will be further discussed in Section 4.4.

The initial difference between measured and nominal ORM produced $\chi = 24.6\,\mu\text{m}$. After LOCO fitting, the calibrated model produced an ORM whose difference to the measured one was $\chi = 0.9\,\mu\text{m}$. The minimum χ obtained from LOCO fitting was almost 4 times greater than the measured BPM accuracy. Even though the obtained χ around

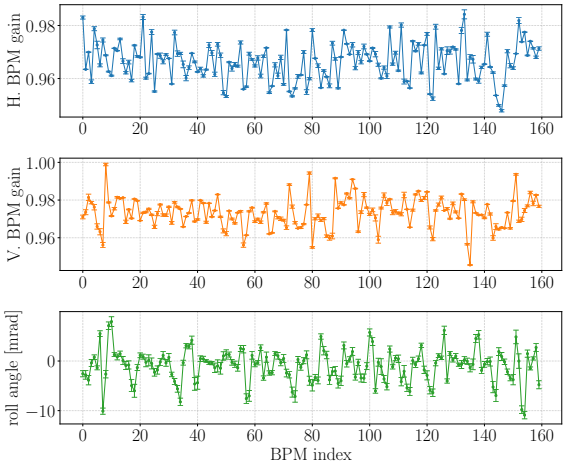

(a) BPM gains and roll angles.

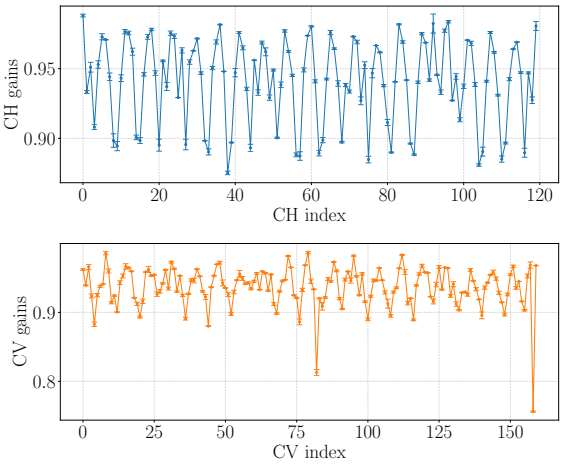

(b) Correctors gains.

Figure 14 – Fitted values for BPM gains, roll errors and correctors (CH and CV) gains.

1 µm represents a good level of fitting, the factor 4 difference from the BPM accuracy values indicates that there are still some systematic errors influencing the measurements, as discussed in [34].

4.2.1 BPM and Corrector Gains

BPMs gains, roll errors and correctors gains are parameters that are related to the correspondent devices, thus it should be independent of the machine optics and coupling. Furthermore, typically these parameters should not vary significantly, especially in a short-term period. Therefore, it is reasonable to include the gains and roll errors as LOCO fit parameters in the first iteration and use these obtained values as initial conditions for the following fittings. It is expected that the gains do not deviate too much from the fit values obtained in the first step. From the first LOCO iteration on Sirius, the BPM gains, roll errors and correctors gains obtained are shown in Figure 14.

The values in format (average $\pm$ std) for each parameter presented in Figure 14 are: 0.966 ± 0.007 for horizontal BPM gain, 0.973 ± 0.008 for vertical BPM gain, 0.94 ± 0.03 for CH gain, 0.94 ± 0.04 for CV gain and (-1 ± 3) mrad for BPM roll error. As discussed in Appendix C, it was defined that the interpretations for BPM and correctors gains are opposite, in the sense that for BPMs the fitted gains represents the corrections factors that should be applied in the measurements to explain correctly the actual orbit distortions, while it is the inverse of correctors gains that should be used in the kicks applied to obtain the actual kicks that affected the beam. Therefore, this fitting indicates that the actual BPMs measurements are around 3% lower than the actual values and the actual kicks that distort the beam orbit are 6% greater than the kicks variations (15 µrad) considered by the control system during ORM measurement. It also can be observed that the spread

between BPM gains is one order of magnitude lower than the spread between correctors and this difference was already expected.

In Figure 14b it can be observed a 20-fold periodic pattern in correctors gains. This signature following the storage ring period is also correlated to the topic of Section 4.4. It also can be seen two outliers in CV gains in 82^{th} and 158^{th} vertical correctors. These correctors were later examined on site but this initial survey did not reveal any anomaly. The cause for these outliers in CV gains is still under investigation and they did not compromise the following results.

As already mentioned, the fitted gains obtained from the first LOCO iteration and presented in Figure 14 were used as initial values for the following iterations. For this study, the obtained values were not used in the control system to correct the BPM measurements nor the correctors excitation curves. This was decided since the fitted gains are close to unity and they do not compromise greatly the orbit correction system and the ORM measurement. For machine studies in the future, when much finer tuning in the storage ring and control system will be performed, the fitted gains and roll errors may also be included as correction factors for BPMs and correctors.

4.2.2 Quadrupoles Gradients

Normal and skew gradients were also included as LOCO fit parameters to adjust the measured ORM. The normal gradients are associated to the corrections that can be applied in 270 quadrupoles trim-coils in Sirius storage ring and skew gradients to the 80 skew quadrupoles coils installed in sextupoles magnets.

The LOCO fitting changes the quadrupole gradients in the model to calibrate the measured ORM, so the integrated gradients are changed by $\text{KL}_{\text{nominal}} \rightarrow \text{KL}_{\text{nominal}} + \Delta\text{KL}_{\text{LOCO}}$. The same is valid for KsL, the skew gradients strength, however the difference is that initially the skew gradients are zero, since in the nominal model the coupling is zero as well. Ideally, $\text{KL}_{\text{actual}} = \text{KL}_{\text{nominal}} + \Delta\text{KL}_{\text{LOCO}}$ represents the actual focusing strengths affecting the electron beam in the actual storage ring. Once the parameters of the real machine are calibrated, we are able to correct it to correspond to the nominal model or any other model of interest. In this way, it is possible to calculate the corrections that change the focusing strengths along the real storage ring to produce a linear optics close to the nominal.

The process of measuring an ORM, fitting it with LOCO and applying the corrections to the machine was realized only twice and the convergence was reached. The corrections distribution history both for normal quadrupoles and skew quadrupoles are shown in Figure 15. The standard deviations of these corrections for each LOCO iteration are organized in Table 6.

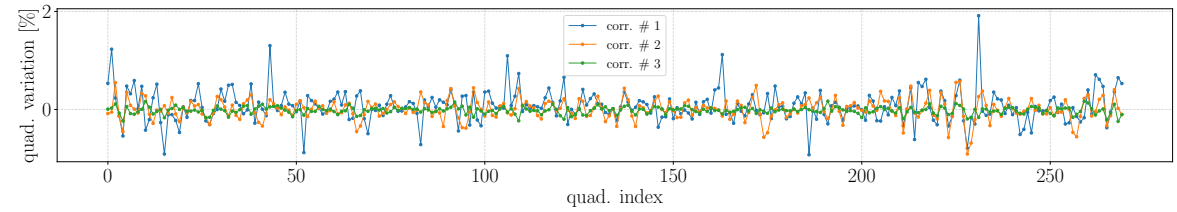

(a) Quadrupoles trim-coils.

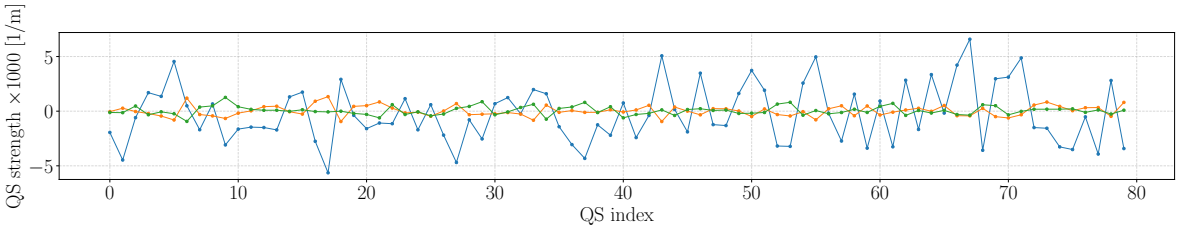

(b) Skew quadrupoles.

Figure 15 – Normal and skew quadrupoles strength variations throughout LOCO iterations.

Table 6 – Corrections strengths variation for each LOCO iteration.

Knobs variation (std)	corr. #1	corr. #2	corr. #3	Unit
Quadrupoles	0.33	0.21	0.07	%
Skew Quadrupoles	$2.7 \cdot 10^{-3}$	$5 \cdot 10^{-4}$	$4 \cdot 10^{-4}$	m^{-1}

From Figure 15 and the values in Table 6 it can be seen that the corrections calculated in the third LOCO iteration and the respective parameters variations obtained, presented in Table 4, are commensurable. Therefore, it was considered that in the third set of corrections the process already converged and this last set was not applied.

4.2.3 Deviations from Nominal

The figure of merit to be minimized with LOCO method is the difference between measured and calculated ORM in each iteration, by changing the storage ring model. As LOCO corrections are applied in the machine elements, it is expected that the measured ORM converges to the nominal ORM. Table 7 shows the progress of ORM differences (represented by χ) throughout LOCO corrections applied to the machine and also the fitting level for each particular iteration.

The LOCO corrections applied to Sirius storage ring decreased the difference between measured and nominal ORM from 24.6 µm to 2.1 µm, which is almost a factor 12 of reduction.

For a global view of measured ORM convergence towards the nominal, Figure 16 shows the histogram of errors for each LOCO iteration. The error histograms are divided

Table 7 – ORM fitting progress.

LOCO iteration	Initial χ [µm]	Final χ [µm]
#1	24.6	0.94
#2	2.7	0.90
#3	2.1	0.92

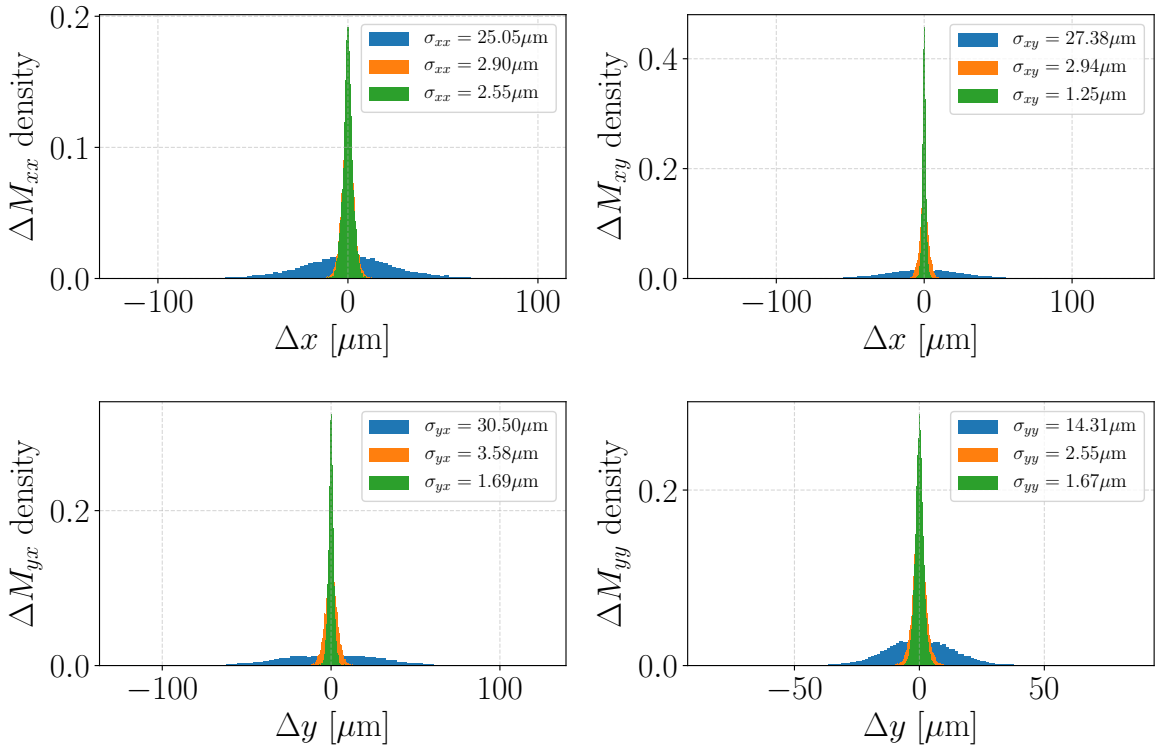

Figure 16 – Histogram for the errors between measured and nominal orbit response matrices for each LOCO iteration. The blue data refers to the measured ORM without corrections applied. The orange data was obtained after the first application of LOCO corrections. The green data is related to the second and last LOCO round applied.

in four parts, following the four ORM blocks: M_{xx}, M_{yy} (diagonal) and M_{xy}, M_{yx} (off-diagonal).

It can be seen that initially the order of magnitude of errors are basically the same for all blocks. The off-diagonal errors (related to coupling errors) are slightly greater than the diagonal errors. After the first correction application in the storage ring, the errors in the four blocks were already greatly reduced. After the second and final corrections the std errors were reduced by the following factors:

$$\sigma_{xx}^{\text{initial}}/\sigma_{xx}^{\text{final}} = 9.8, \qquad \sigma_{xy}^{\text{initial}}/\sigma_{xy}^{\text{final}} = 21.9,$$
$$\sigma_{yx}^{\text{initial}}/\sigma_{yx}^{\text{final}} = 18.0, \qquad \sigma_{yy}^{\text{initial}}/\sigma_{yy}^{\text{final}} = 8.6.$$

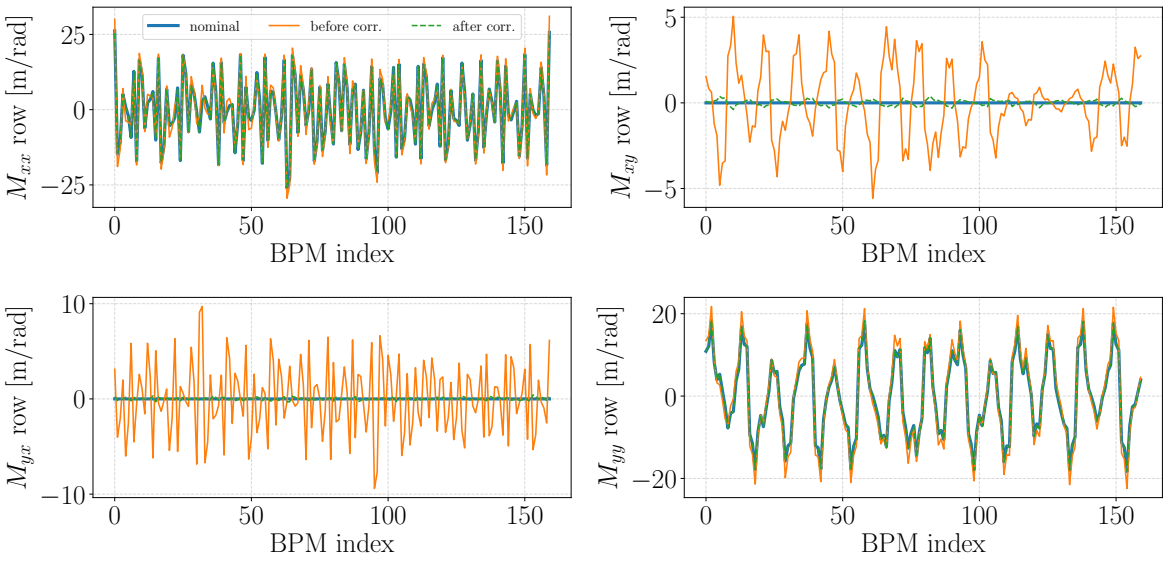

Figure 17 – ORM rows for the first CH and CV. The blue curve is the nominal ORM, the orange curve represents the measured ORM before LOCO corrections and the green curve is from measured ORM after LOCO.

The off-diagonal errors were reduced by a factor of 2 greater than the diagonal errors.

Two ORM columns were taken to exemplify typical differences between measured and nominal matrices, before and after LOCO corrections and the results are presented in Figure 17. The first column is related to a horizontal corrector signature and the second one to a vertical corrector. Multiplying the ORM columns by the kicks $\Delta\theta_x$ and $\Delta\theta_y$, one can obtain the orbit distortion signature Δx and Δy.

In this example it can be seen that the off-diagonal elements are greatly reduced and are close to zero after corrections. The diagonal elements for measured and nominal ORM are practically overlapped.

4.2.4 Final Corrections

Adding up the corrections sets for normal and skew quadruploles gradients in the two LOCO iterations, the total corrections were obtained and plotted in Figure 18.

The final quadrupole gradients variations covers the range of $\pm 2\%$, while the skew quadrupole strengths are between $\pm 5 \cdot 10^{-3}\,\mathrm{m}^{-1}$. Based only on magnetic characterization of quadrupoles fields, variations of 2% are large, since the specifications for gradient errors were 0.05%. On the other hand, it is important to remember that these quadrupole variations are corrections for gradient errors along the whole storage ring. Thus, it is more likely that these corrections are compensating for other sources of gradient errors. The most important contribution is additional fields in quadrupoles and sextupoles caused

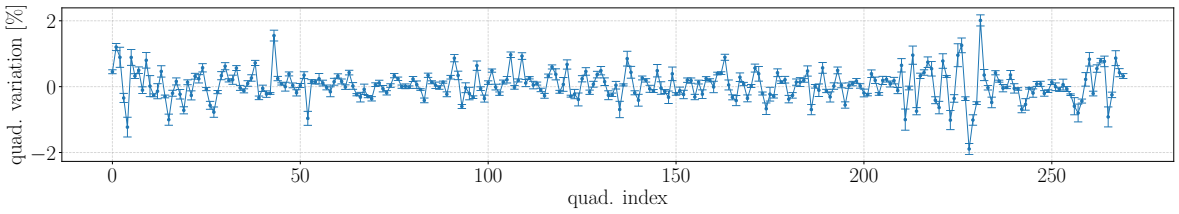

(a) Quadrupoles trim-coils.

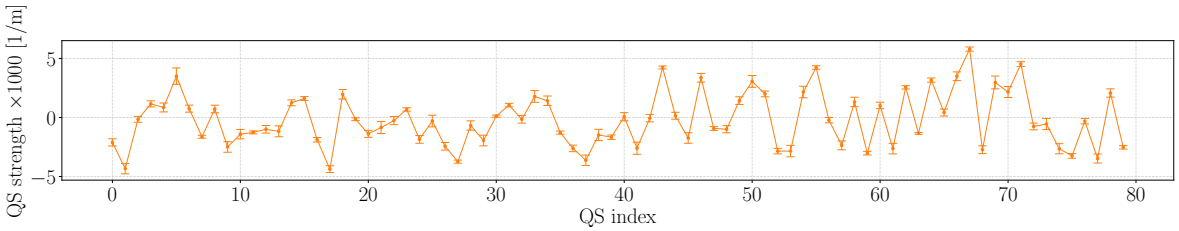

(b) Skew quadrupoles.

Figure 18 – Normal and skew quadrupoles final corrections.

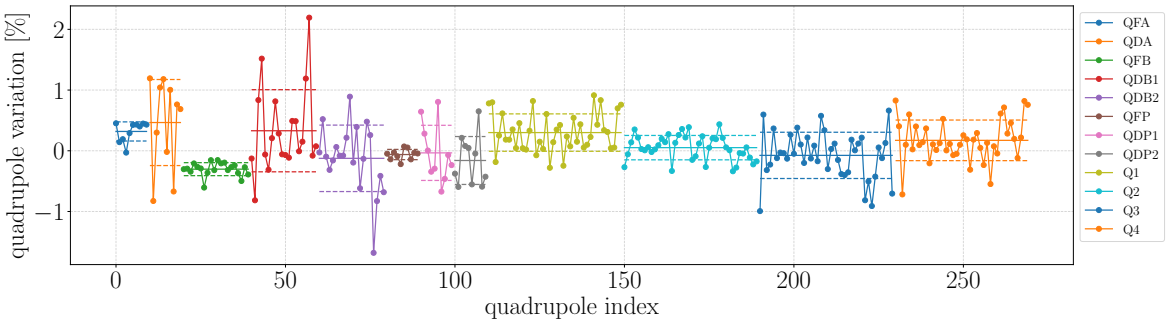

Figure 19 – Quadrupoles families final variations after two LOCO iterations. The continuous lines indicate the family average variation and the dashed lines correspond to ± std.

by the feed-down effect (Appendix A for details) due to magnet misalignment and orbit distortions. These other sources of gradient errors may accumulate in such a way that quadrupole variations on the order of 2% might be necessary for compensation.

An interesting way to visualize the quadrupole variations is dividing them following the 12 quadrupoles families in storage ring. The magnets that make up each family were selected to minimize the spread in gradient strengths within the families and to satisfy the 0.05% specification on gradient errors. The results of this rearrangement in families are shown in Figure 19. The statistics for these quadrupole variations divided by families are organized in Table 8.

Mechanically, three types of quadrupoles were used in Sirius storage ring, namely Q14, Q20 and Q30. The number in the name indicates the magnet length, 14 cm, 20 cm and 30 cm, respectively. The shorter quadrupoles, Q14, were used as defocusing quadrupoles.

Table 8 – Quadrupole families corrections.

Quad. Family	mean [%]	std [%]	peak-to-valley [%]
QDA	0.45	0.71	2.02
QDB1	0.31	0.68	3.00
QDB2	-0.14	0.55	2.57
QDP1	-0.05	0.45	1.48
QDP2	-0.18	0.39	1.25
QFA	0.31	0.16	0.48
Q1	0.30	0.31	1.19
Q2	0.05	0.20	0.77
Q3	-0.08	0.38	1.66
Q4	0.17	0.33	1.55
QFB	-0.31	0.11	0.45
QFP	-0.07	0.08	0.29

Q20 were used as quadrupoles in arc sections and for focusing quadrupoles in high-beta straight sections. The longest quadrupoles, Q30, were used as focusing quadrupoles in low-beta sections, in order to provide a larger integrated gradient field to focus the betatron functions in the straight sections. The quadrupole families information in Table 8 are divided with horizontal line into three groups, following each magnet type to which each corresponding family.

For Sirius quadrupoles, the integrated gradient strength increases with the quadrupole length. Suppose that the variations ΔKL calculated with LOCO are on the same order of magnitude for all quadrupoles. Thus, the relative change ΔKL/KL is smaller as the quadrupole's integrated gradient is larger, as can be confirmed in Table 8. This indicates that there is no systematic problems in specific quadrupoles types and families.

4.2.5 Calibrated Model Parameters

Once the measured ORM is adjusted, with the obtained calibrated model one can calculate lattice functions (beta and dispersion), and global parameters, such as betatron tunes and emittances. If the model describes accurately the real machine, this provides an indirect estimate of corresponding actual parameters.

A function that is related to the storage ring linear optics errors and asymmetries is the betatron function relative error $\Delta\beta(s)/\beta(s)$, called beta-beating. The beta-beating is a s-dependent function but it is common to use its standard deviation value as a characteristic parameter for the optics errors level. The dispersion function std deviation from nominal values is an usual parameter to indicate the optics error as well. In Table 9, the std values for beta-beating and dispersion errors are shown for each of the LOCO fits.

Table 9 – Lattice functions errors from calibrated model throughout LOCO fittings.

Parameter (std)	fitting #1	fitting #2	fitting #3	Unit
$\Delta\beta_x/\beta_x$	11.2	1.3	1.1	%
$\Delta\beta_y/\beta_y$	7.9	0.9	1.6	%
$\Delta\eta_x$	10.1	1.6	1.4	mm
$\Delta\eta_y$	3.1	1.4	0.5	mm

Table 10 – Predicted fractional tunes from calibrated model compared to the measured ones for each LOCO fitting.

Parameter	fitting #1	fitting #2	fitting #3
measured ν_x	0.076	0.076	0.076
model ν_x	0.079	0.075	0.075
measured ν_y	0.134	0.138	0.136
model ν_y	0.135	0.137	0.133

Table 11 – Emittances from calibrated model throughout LOCO fittings.

Parameter	fitting #1	fitting #2	fitting #3	Unit
ϵ_0	283.4	250.4	251.6	pm rad
ϵ_x	280.7	250.0	251.5	pm rad
ϵ_y	2.65	0.37	0.07	pm rad
ϵ_y/ϵ_x	0.94	0.15	0.03	%

The results in Table 9 indicate that $\Delta\beta_x/\beta_x$ in the calibrated models could have been reduced to one tenth of its initial value. $\Delta\beta_y/\beta_y$ was reduced by a factor 5. The reduction factors for horizontal and vertical dispersion errors were 7 and 6, respectively. However, independent measurements performed in the storage ring indicate that the actual error reductions were lower than predicted with LOCO models, as presented in the next section.

From the calibrated model, the calculated fractional tunes agreed quite well with the measured ones as can be seen in Table 10. The differences between the measured and predicted tunes from LOCO are on the order of $1 \cdot 10^{-3}$ for both planes.

Finally, with the calibrated models the emittances were also calculated and the results are presented in Table 11. Initially the model indicated that the natural emittance was 13% higher than the nominal value of 251 pm rad. The vertical emittance generated an emittance coupling ratio of 0.94%. The natural emittance obtained with the final calibrated model was very close to the nominal and the vertical emittance was very close to zero.

4.3 Independent Measurements

Some measurements can be performed to check independently the impact of LOCO corrections on Sirius storage ring. Lattice functions, betatron and dispersion, are measured to verify the machine linear optics and its deviations from the nominal functions. Measuring the closest betatron tunes approximation provides information about the global betatron coupling. To check the performance in beam dynamics, one can measure the dynamic aperture and injection efficiency, two typically correlated quantities. When these studies were performed, the Sirius diagnostic beamline was not installed yet, so it was not possible to perform beam size and emittance measurements.

4.3.1 Dispersion Function

The information about dispersion function is already encoded in one of ORM columns. A column of this matrix is the orbit response due to a variation in RF frequency. From Eq. (3.5), the dispersion function at the BPMs positions can be calculated as:

$$\eta_u(s_i) = -\alpha f_{\mathrm{rf}} \frac{\Delta u_i}{\Delta f_{\mathrm{rf}}}, \tag{4.1}$$

where $u = x, y$ and α is the momentum compaction factor. Thus, given the RF frequency used in ORM measurements, the dispersion is obtained with the corresponding ORM column.

In this case, the dispersion function is not exactly an independent measurement, since it is included in LOCO fitting. For Sirius, it was required to include a weight factor to force the matching between measured and calculated dispersion function. It was verified that if this factor was not used, the measured ORM was adjusted except for the dispersion column. Applying the gradients variations calculated by LOCO actually increased $\eta(s)$ errors, especially in the vertical plane. On the other hand, if the weight factor was further increased, the measured $\eta(s)$ was better explained with the model however the ORM fitting quality was lowered.

With the measured ORMs before and after LOCO corrections, η_x and η_y at BPMs were calculated and compared with the nominal function. The results are shown in Figure 20.

It can be observed that the horizontal dispersion errors were greatly reduced, especially in straight sections, were $\eta_x = 0$ nominally. However, the errors in vertical dispersion could not be reduced with the same effectiveness. This was already expected, since the LOCO calibrated models predicted η_y functions very different from the measured ones. Initially the std error for η_x was 10.2 mm and after the corrections it was reduced to 1.6 mm. For η_y, these errors were 2.8 mm before and 1.9 mm after LOCO. From Table 9, it is seen that LOCO model accurately predicted the values obtained in the actual storage

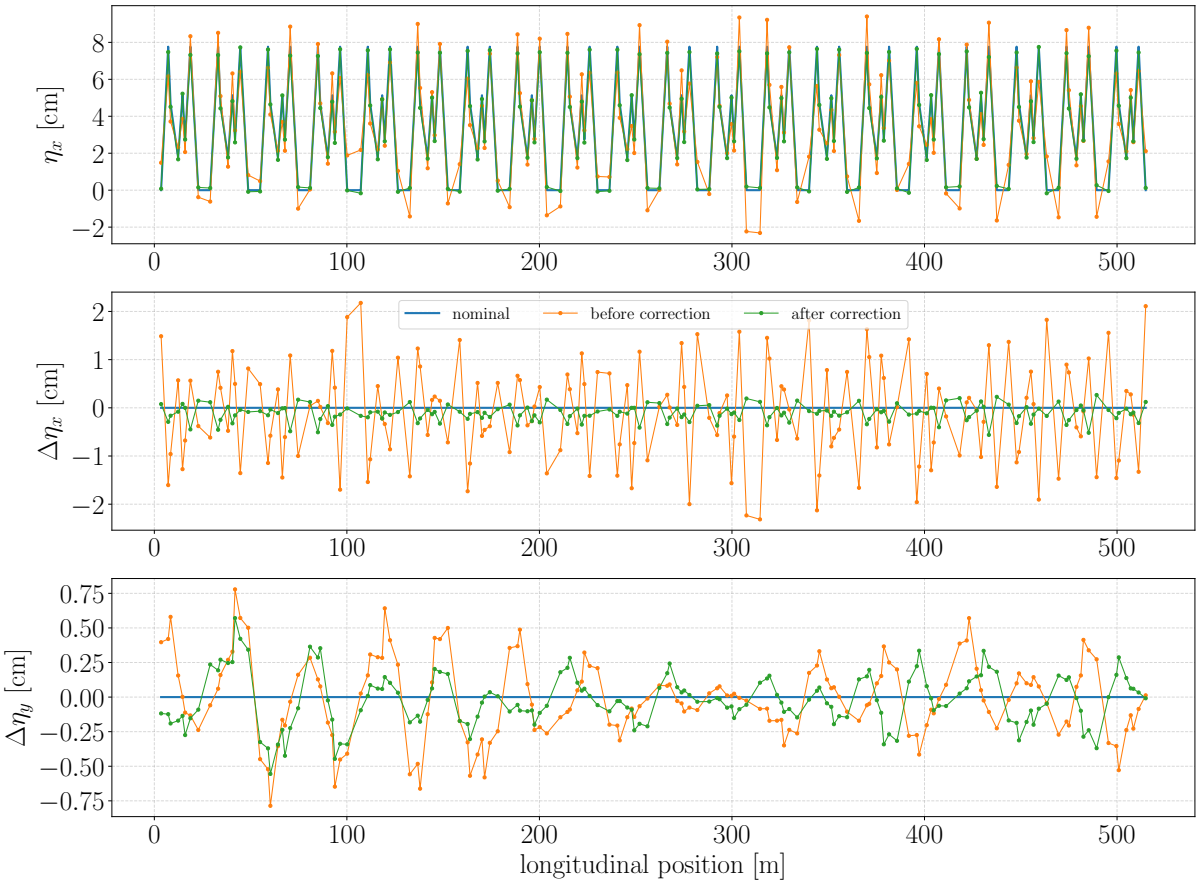

Figure 20 – Measured dispersion functions on BPMs and its differences from nominal values.

ring for η_x. On the other hand, even though the initial predicted and measured η_y are in concordance, the final η_y error calculated with the calibrated model is about 4 times lower than the corresponding measured error. This incompatibility will be further discussed in Section 4.4.

4.3.2 Betatron Function

There is a quite simple method for measuring the betatron function. In Subsection 2.4.2 it is discussed how gradient errors perturb the linear optics on a storage ring. In Appendix F the effect of a single gradient error in a quadrupole of length L on the betatron tunes, given the beta function, is calculated. The process can be reversed: intentionally changing the integrated gradient of a single quadrupole by a small amount ΔKL and measuring the corresponding tune shift, the integral of beta function along the quadrupole is calculated as:

$$\frac{1}{L}\int_0^L \beta_u(s)\mathrm{d}s = 4\pi\frac{\Delta\nu_u}{\Delta\mathrm{KL}}, \tag{4.2}$$

Table 12 – Variations in lattice functions for 10 sequential measurements performed in Sirius storage ring.

Lattice function error	mean rms	rms variation	peak-to-valley rms	Unit
$\Delta\beta_x/\beta_x$	3.9	0.8	4.3	%
$\Delta\beta_y/\beta_y$	4.1	0.5	4.2	%
$\Delta\eta_x$	1.6	0.2	0.9	mm
$\Delta\eta_y$	1.9	0.3	1.3	mm

where $u = x, y$. This method has the disadvantage that the gradient variation ΔKL applied in the quadrupole must be well known, otherwise this introduces systematic errors in beta calculation. Since the tune measurements are typically very precise, the contribution of the error of $\Delta\nu_u$ to the beta function measurement is negligible.

This process, which will be called beta measurement by individual quadrupole variation, can be performed for each quadrupole to measure the betatron functions around the storage ring. Then, the obtained values can be compared to the nominal ones, which is calculated numerically with the model, simulating the described process, or evaluated with analytical expressions, derived in Appendix F.

The author implemented the beta measurement for Sirius storage ring in a Python script and the code can be accessed in its GitHub Repository [60]. The script also performs the data analysis and evaluates the beta integrals for a given Sirius storage ring model, returning both measured and model beta integrals at quadrupoles for comparison.

The measurement process was tested and adjusted several times. After 10 ORMs were measured to obtain the fit parameters variations as discussed in Subsection 4.1.2, 10 sequential beta measurements were performed as well[2]. Calculating the dispersion function from the 10 measured ORMs, the variations for lattice functions measurements in Sirius storage ring were obtained and the results are organized in Table 12.

The std variations for each point were used to define the related error bars, which is this case are related to random errors. Note that dispersion function measurement variations are low, due to the fact that RF frequency changes are precise and well-known. On the other hand, variations in beta measurement are on the order of few percent. The main cause for this is hysteresis in the quadrupoles gradient fields. It is desirable to correct the storage ring linear optics in the level of the measurement's errors. From simulations with random errors in the model, it was possible to obtain beta-beatings std as low as 1%.

The implemented script was applied to obtain the Sirius beta functions before and after the application of LOCO corrections in quadrupole's trim-coils and the results are

[2] Again, the repeatability test for optics function measurements was performed after LOCO corrections.

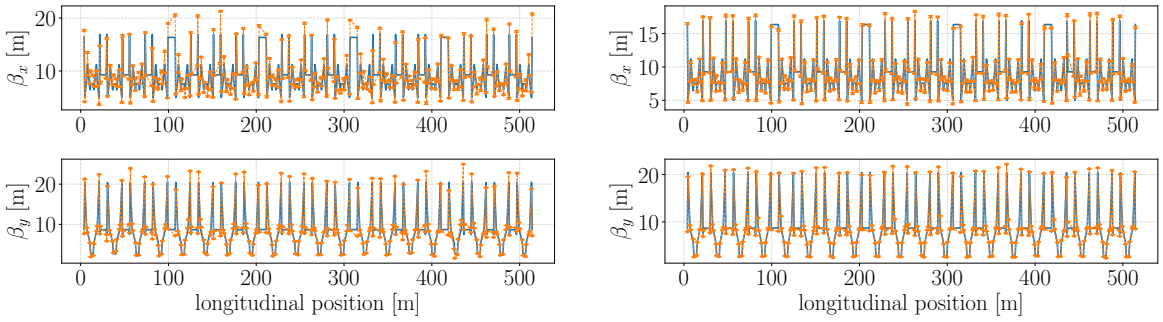

(a) Before. (b) After.

Figure 21 – Nominal (blue) and measured (orange) betatron functions before and after LOCO corrections.

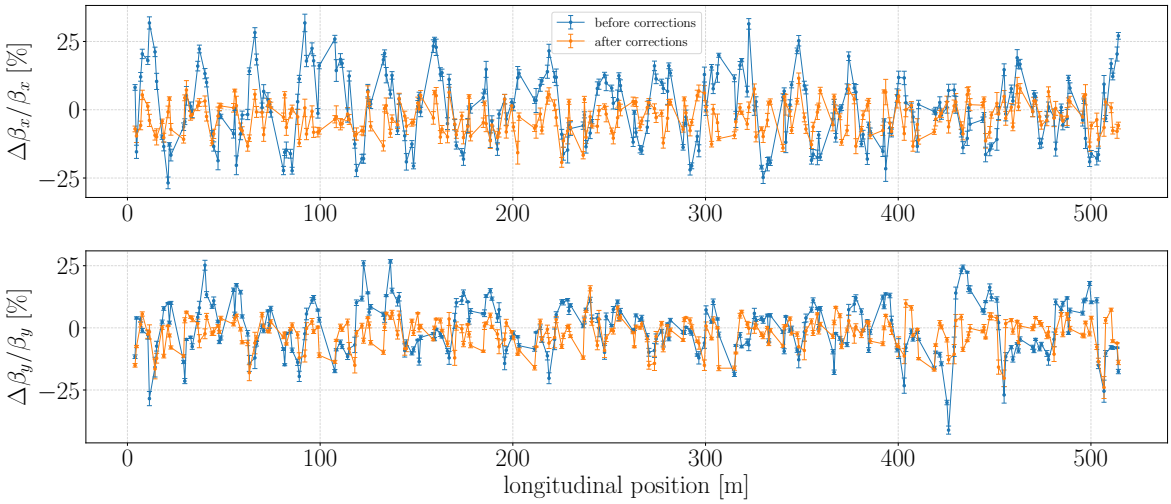

Figure 22 – Comparsion of beta-beating before and after optics corrections.

shown in Figure 21. The corresponding beta-beatings for the measured values are plotted in Figure 22.

Before LOCO corrections, measured horizontal and vertical beta-beatings (std) were $(12.8 \pm 0.8)\,\%$ and $(10.4 \pm 0.5)\,\%$, respectively. With new gradients settings these values were reduced to $(3.9 \pm 0.8)\,\%$ and $(4.1 \pm 0.5)\,\%$.

An alternative method to measure beta functions can be performed by applying Principal Component Analysis (PCA) in TbT position measurements from BPMs. The beam trajectory can be perturbed with a dipolar impulse, applied by an element in the storage ring called pinger, that excites betatron oscillations that can be acquired with BPMs. The oscillation harmonics encoded in the BPM data can be identified and separated with PCA. The two main components for each plane of oscillation are related to the betatron motion and from these two main harmonics it is possible to extract the beta functions and the phase advances in BPMs. For more details about the method, the

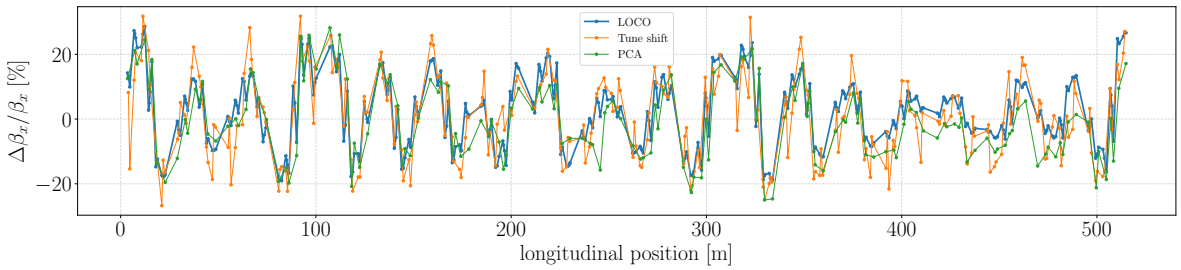

(a) Before correction.

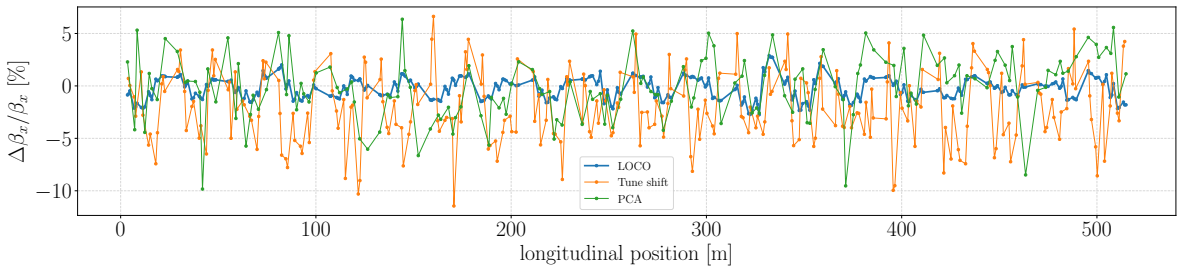

(b) After correction.

Figure 23 – Horizontal beta-beating comparison between predicted beta with LOCO model and beta measurements: at quadrupoles based on tune shifts and at BPMs based on PCA applied on TbT data.

author recommends the reference [1].

In Sirius storage ring, the dipolar kicker, used for on-axis injection, can also be used as a horizontal pinger. When these measurements were conducted, a vertical pinger was not available, so it was possible to measure only the horizontal beta function in BPMs using PCA method. These measurements were done before and after LOCO corrections, using a small kick of 100 µrad and analysing the TbT data for 4000 turns. The horizontal beta-beatings obtained were compared with measurements by individual quadrupole variation and with the predicted beta-beating from LOCO calibrated models. These results are plotted in Figure 23.

Before LOCO corrections, the three measurements agreed quite well. The correlation between LOCO and PCA beta-beating signatures is 91% and between LOCO and tune shifts is 86%. On the other hand, it can be seen that after the corrections, the LOCO model fails to predict the measured beta-beating in storage ring. In this situation, the correlation between LOCO and PCA values is 39% and LOCO and tune shifts it is only 8%. The same is valid for std beta-beating, before corrections the values were; LOCO: 11.3 %, tune shift: 12.8 %, PCA: 11.5 % and after corrections; LOCO: 1.0 %, tune shift: 3.3 %, PCA: 3.0 %. Then, in the latter case, the calibrated model predicted a horizontal beta-beating that is 3 times smaller than the measured values in Sirius storage ring. At this stage, this was an indication that the correspondence between the model and the

actual ring was no longer valid. This will be further discussed in Section 4.4.

4.3.3 Betatron Coupling

In Subection 2.4.3 the effect of skew gradients on betatron coupling was briefly discussed. It was shown that a global parameter $|\kappa|$, called global betatron coupling, can be measured by approximating the betatron tunes, taking advantage on the fact that the tune difference resonance is stable. In the presence of coupling, the transverse tunes ν_x and ν_y are replaced by two normal tunes ν_1 and ν_2, also called eigentunes. This coupling problem can be formulated to be mathematically equivalent to the avoided-crossing problem in a two-level system in quantum mechanics. In this case, the matrix $\mathbf{C} = \begin{bmatrix} \nu_x & \kappa \\ \kappa & \nu_y \end{bmatrix}$ takes the place of the two-state hamiltonian and its eigenvalues are calculated as:

$$\nu_1 = \frac{\nu_x + \nu_y}{2} + \frac{1}{2}\sqrt{\left(\frac{\nu_x - \nu_y}{2}\right)^2 + 4\kappa^2}, \tag{4.3}$$

$$\nu_2 = \frac{\nu_x + \nu_y}{2} - \frac{1}{2}\sqrt{\left(\frac{\nu_x - \nu_y}{2}\right)^2 + 4\kappa^2}. \tag{4.4}$$

The equations above are equivalent to Eq. (2.41). In the limit $\nu_x = \nu_y$, we also obtain that $\nu_1 - \nu_2 = |\kappa|$.

The tunes approximation can be performed by changing the focusing strengths in the storage ring. In Sirius, the fractional horizontal tune is lower than the vertical tune, thus the tunes can be approximated by increasing a focusing quadrupole strength. The QFB family was chosen for this experiment. If the current that feeds this quadrupole family is changed by $\Delta I_{\mathrm{QFB}} > 0$, there is a corresponding change in horizontal tune $\Delta\nu_x > 0$ and vertical tunes $\Delta\nu_y < 0$. In this way, the tune sum and the difference can be viewed as functions of QFB current.

The measurement script and analysis was implemented by the APG and used by the author in Sirius storage ring to obtain the global betatron tunes before and after LOCO corrections. The results are shown in Figure 24. The gray curve presented in Figure 24 was obtained by plugging the measured ν_x, ν_y for each current I_{QFB} in matrix $\mathbf{C}$, diagonalizing it and fitting the parameter κ and the offsets $(\nu_x + \nu_y)/2$ that minimize the quadratic difference to the data.

For LOCO coupling corrections applied on skew quadrupoles, the residues used for minimization were M_{xy} and M_{yx}, the ORM off-diagonal elements, which are related to the local coupling along storage ring. However, the minimum tune difference measurements showed that the global betatron coupling was reduced as well, from the initial value of $(0.78 \pm 0.04)\,\%$ to $(0.07 \pm 0.01)\,\%$.

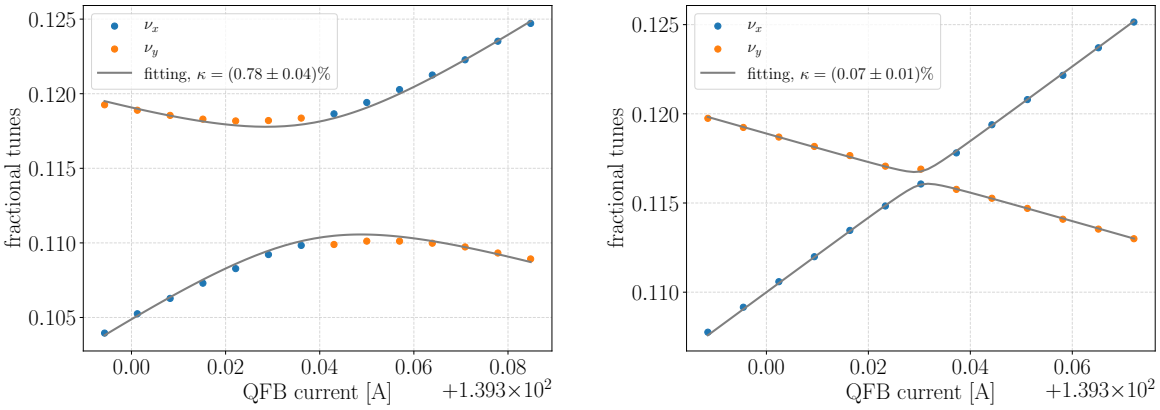

(a) Before. (b) After.

Figure 24 – Global betatron coupling before and after LOCO corrections.

It is important to mention the goal coupling for Sirius storage ring is not necessarily small. The coupling parameter is somewhat a free parameter that can be varied to suit other purposes, for example to increase the beam lifetime or the vertical beam size. Neverthless, a common procedure is to first reduce the betatron coupling as much as possible, then increase the coupling towards the goal value in a controlled manner. With these studies, it was proved that LOCO is a robust method to minimize the off-diagonal ORM elements and in this process the global betatron coupling is consequently reduced. However, even though the measured betatron coupling is near zero, since the vertical dispersion function could not be reduced with LOCO corrections, it is likely that the vertical beam emittance is still about 1% of the horizontal emittance, as calculated with the first LOCO calibrated model.

4.3.4 Horizontal Dynamic Aperture

The horizontal pinger can also be used to apply dipolar impulses in the stored electron beam with increasing amplitudes until the beam is partially or totally lost. Measuring with BPMs the transverse oscillations over the turns, one can obtain how much beam is lost as a function of the transverse positions. This is basically the dynamic aperture measurement. Since only the horizontal pinger was available in Sirius storage ring, only the horizontal dynamic aperture could be measured.

Figure 25 shows the measurement results before and after optics and coupling corrections. Setting 5% as the beam loss limit to estimate the dynamic aperture, after the application of LOCO corrections on linear optics and coupling, the horizontal dynamic aperture was increased from 7.6 mm to 8.3 mm, which is an improvement of approximately 10%.

The horizontal dynamic aperture is important for Sirius injection, given that

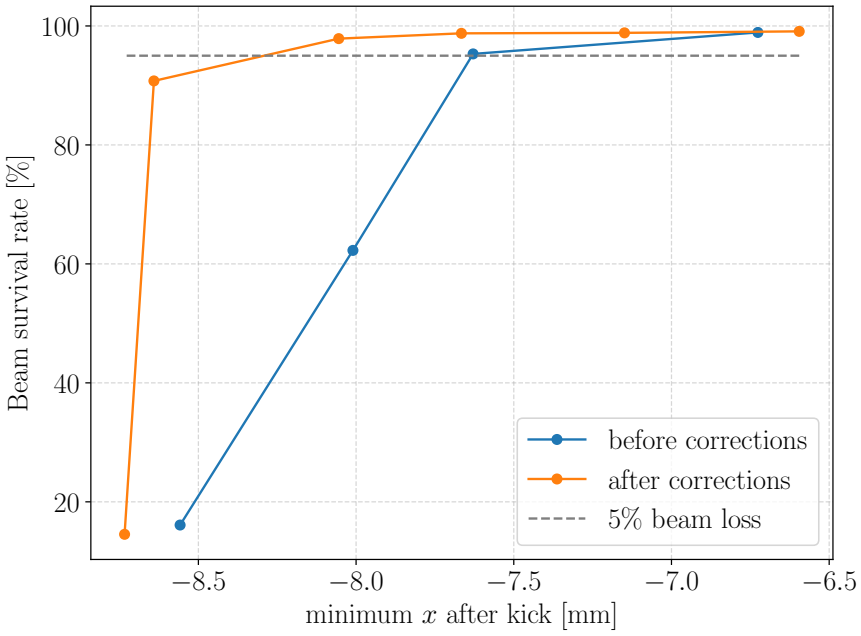

Figure 25 – Comparison of horizontal dynamic aperture measurement before and after LOCO corrections.

a NLK is used to perform the off-axis injection in the storage ring. The off-axis injection occurs at $x = -8\,\text{mm}$ from the vacuum chamber center, because at that location the NLK field is maximum. The NLK field rapidly decays as the position approaches $x = 0$, causing no effect on the stored beam. More information about off-axis injection with NLK can be found in [24, 61].

To efficiently inject electrons from Booster with NLK, the storage ring dynamics at $x = -8\,\text{mm}$ must be stable. From the simulations with Sirius storage ring model, including alignment and field errors (satisfying the specifications), the dynamic aperture obtained was $x = -9.5\,\text{mm}$. Therefore, even with the improvement obtained with LOCO corrections, the measured horizontal dynamic aperture is still about 15% lower than expected from simulations.

It is worth to mention that beam dynamics in Sirius storage ring depends strongly of non-linear effects, which is well-known for 4GSRs. At the time of writing, non-linear optimizations were not carried out in Sirius yet. This kind of optimization is one example of accelerator physics studies that might improve the storage ring dynamic aperture towards design values.

4.3.5 Injection Efficiency

To close this section of independent measurements, the injection efficiency in the storage ring was recorded before and after linear optics and coupling corrections. The data

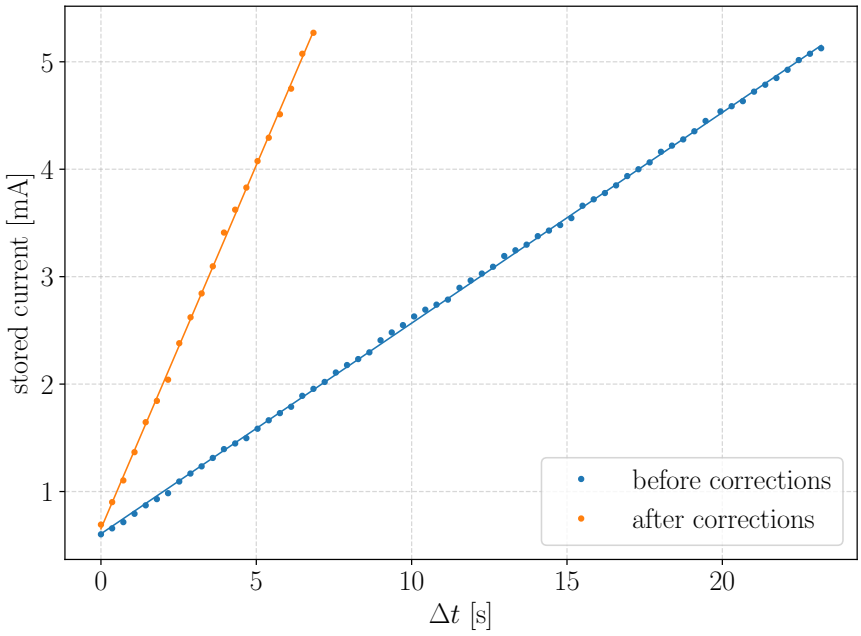

Figure 26 – Beam accumulation before and after LOCO corrections.

is presented in Figure 26. A linear fitting was applied on the data. The angular coefficient increased from 196 µAs^{-1} to 677 µAs^{-1}. The Sirius injection rate is 2 Hz and the current delivered by booster to the storage ring is 500 µA on average, i.e, with an injection without any losses, the accumulation rate would be approximately 1 mAs^{-1}. Therefore, with optics and coupling corrections, the average injection efficiency was increased from 20% to 68%, which is an improvement of a factor 3.4. During the commissioning, large pulse-by-pulse variations on injection efficiency have been observed. The changes in injection efficiency recorded were as high as 20%. This problem might be related to the dynamic aperture, since its measured value indicates that the electron beam had to be injected in the dynamic aperture edge in order to receive the required kick from NLK. In this situation, any change of a few percent in the injection condition leads to electron losses. Leak fields from the injection pulsed magnets were also measured with the stored beam during the commissioning and shielding schemes are being studied to minimize their negative effects on injection. For the top-up injection mode on Sirius, an injection efficiency higher than 95% with small pulse-by-pulse variation is required, so Sirius injection efficiency optimization was a work in progress at the time of writing.

4.4 Orbit Effect on Optics and Coupling

Orbit correction on Sirius storage ring was performed as follows: the BPM offsets with respect to quadrupoles centers were measured to define the BBA orbit, then this orbit was used as the target for orbit correction. In this process, it was not possible to

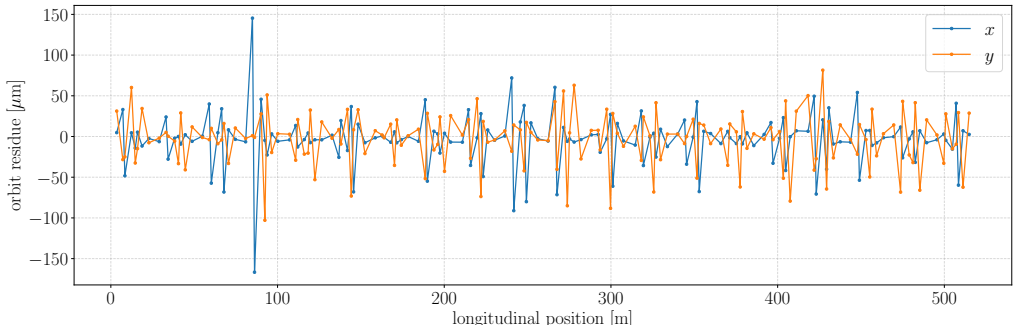

Figure 27 – Residual orbit in Sirius storage ring.

use all 281 singular values available in ORM in the corrections, otherwise the correctors strengths would surpass the kick limits: ±330 µrad. Thus, it was necessary to use only 180 singular values in orbit correction and the final residual orbit, represented in Figure 27, was obtained.

The std values for the distortions in Figure 27 are 31 µm in horizontal plane and 32 µm in vertical. The peak-to-valley values are 312 µm and 184 µm for x and y, respectively. From simulations, with alignment and field errors (within specified tolerances) on storage ring model, the orbit correction performance was better than the obtained in the actual ring, with std of 17 µm in the horizontal plane and nanometric std orbit vertically. This is an indicative that the real alignment errors are greater than the specifications.

It is well-known that the magnetic fields in a storage ring depend on the relative transverse position of the beam with respect to the magnets centers. This is the feed-down effect that was already mentioned throughout this work and it is discussed in Appendix A. Since very strong quadrupoles and sextupoles are used in Sirius MBA lattice, it is expected that the dependencies of linear optics and coupling related to orbit distortions might play an important role.

To study the contribution of orbit distortion on optics and coupling, the residual orbit in the storage ring was reproduced in the nominal model. At this stage, the betatron tunes were $\nu_x = 48.917$ and $\nu_y = 13.961$, and the tunes were corrected to the nominal values. Note that the distorted orbit produced large tune shifts of $\Delta\nu_x = -0.18$ and $\Delta\nu_y = -0.19$. An ORM was calculated with this model and was used as input for a LOCO fitting with the same configuration used for the fitting of measured ORMs. The initial difference between this ORM and the nominal was $\chi = 8.7$ µm. After the fitting, the final difference was $\chi = 0.7$ µm. Considering the measured Sirius BPM accuracy of 0.25 µm approximately, a rough estimate of this noise effect on data would increase the final χ, being closer to the same level obtained in LOCO fittings from measured ORM in the storage ring (about 0.95 µm).

The qualitative behavior of LOCO fitting in this test was very similar to the

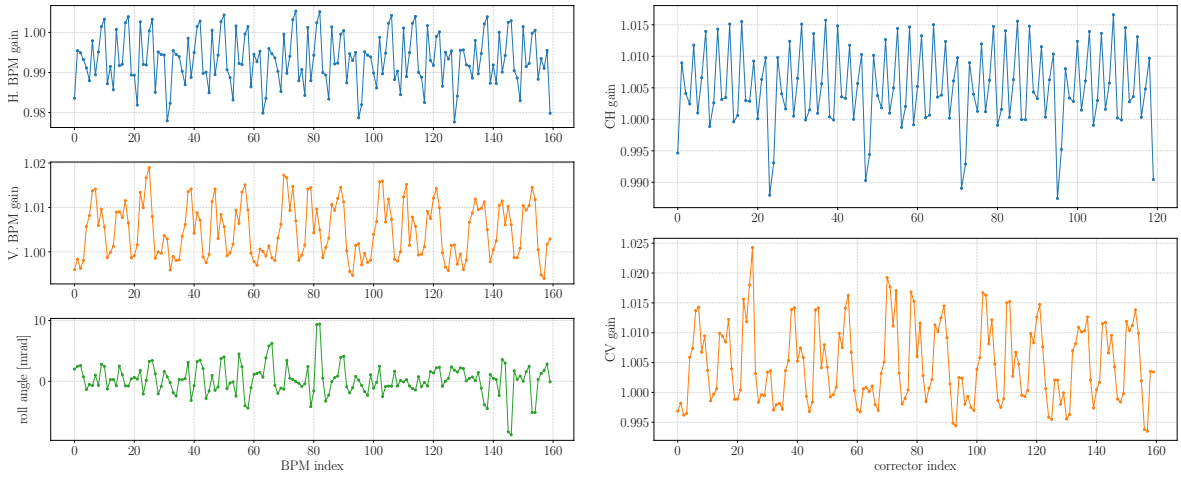

(a) BPM gains and roll angles.

(b) Correctors gains.

Figure 28 – Fitted values for BPM gains, roll errors and correctors (CH and CV) gains for model with perturbed orbit.

fittings performed with the measured ORM. The fitted ORM was adjusted in a very good level, both in diagonal and off-diagonal blocks. It was necessary to include the dispersion function in the fitting with weight 2, otherwise the horizontal dispersion obtained with the calibrated model would not match the dispersion from the perturbed orbit model. The vertical dispersion function could not be reproduced with LOCO model as well.

Although there was no errors in BPM gains and roll angles and correctors gains, during the fitting these parameters were changed to adjust the ORM. The results for these fit parameters are shown in Figure 28.

One can note the periodic signature in the gains. Even though the absolute values are smaller than the gains obtained in the previous fitting (Figure 14), the periodic signature observed previously (especially for correctors) can be related to the ones obtained here. The BPM roll angles adjusted in this test were also on the order of ± 10 mrad. Thus the values obtained previously probably are not related to the BPM roll errors and the major contribution might be from the orbit distortion.

The beta-beatings caused by the residual orbit were also calculated and compared with the first LOCO fitting reported in Section 4.2. The results are presented in Figure 29. The disturbed orbit produced std beta-beatings of 8.6 % in horizontal and 3.0 % in vertical plane. It can be seen that the orbit contributions to the beta-beating in some locations are commensurable to the ones obtained from the calibrated model. The fact that the predicted beta-beating is larger than the one caused by orbit distortion is reasonable, since in the actual storage ring there are other sources of optics perturbations.

Another comparison was performed between the dispersion functions from the perturbed orbit model and the measurements realized on storage ring before LOCO cor-

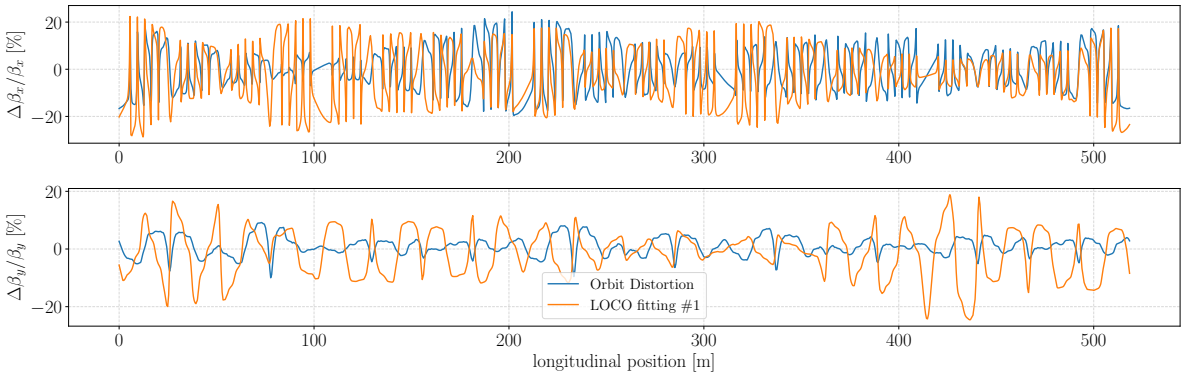

Figure 29 – Beta-beating comparison from perturbed orbit model with first LOCO calibrated model.

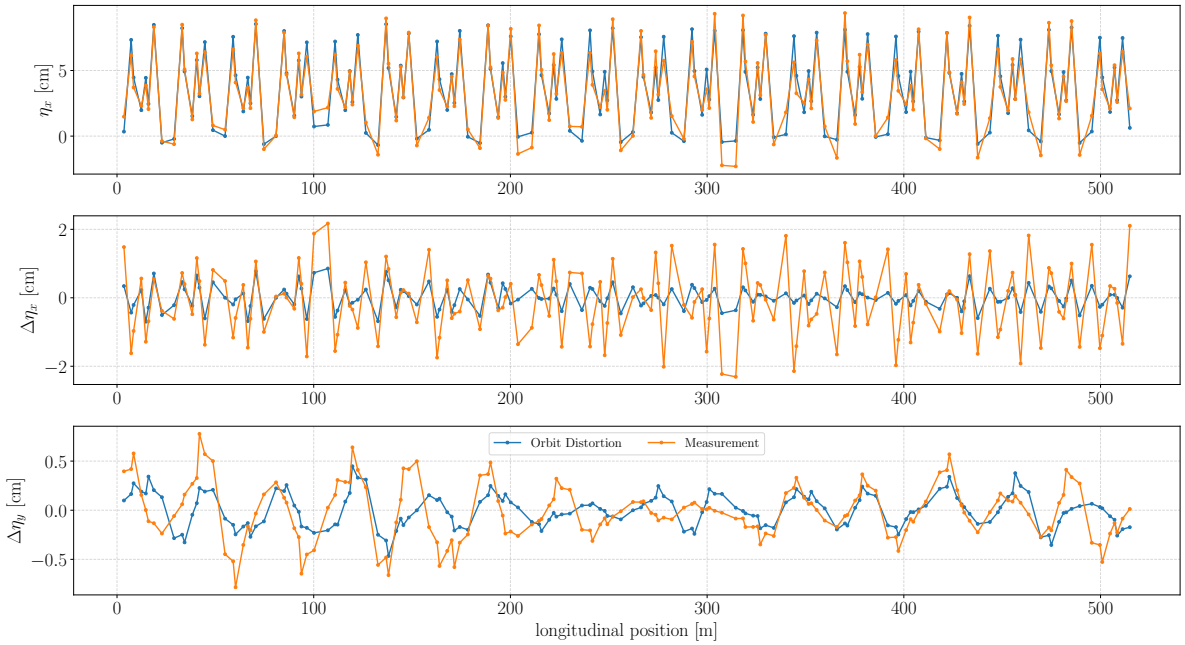

Figure 30 – Comparison between dispersion functions at BPMs obtained perturbed orbit model with measurement before optics corrections.

rections, plotted in Figure 30. Once again, the actual errors are larger than the ones generated by the feed-down effect, as expected. The vertical dispersion signature similarities draw attention. It is clear that the errors in η_y caused by orbit distortion explain a substantial part of the measured η_y. The correlation between measured $\Delta\eta_x$ and the calculated with orbit distortions is 76% and for $\Delta\eta_y$ the correlation is 53%. The main sources of η_y are vertical bendings created by vertical orbit distortions on quadrupoles.

Finally, the variations in normal and skew quadrupoles obtained in this test were compared with LOCO corrections applied in storage ring, as can be seen in Figure 31.

The order of magnitude of variations in both cases are very similiar. For quadrupoles, the std variations are 0.36 % for orbit perturbed model and 0.33 % for LOCO corrections.

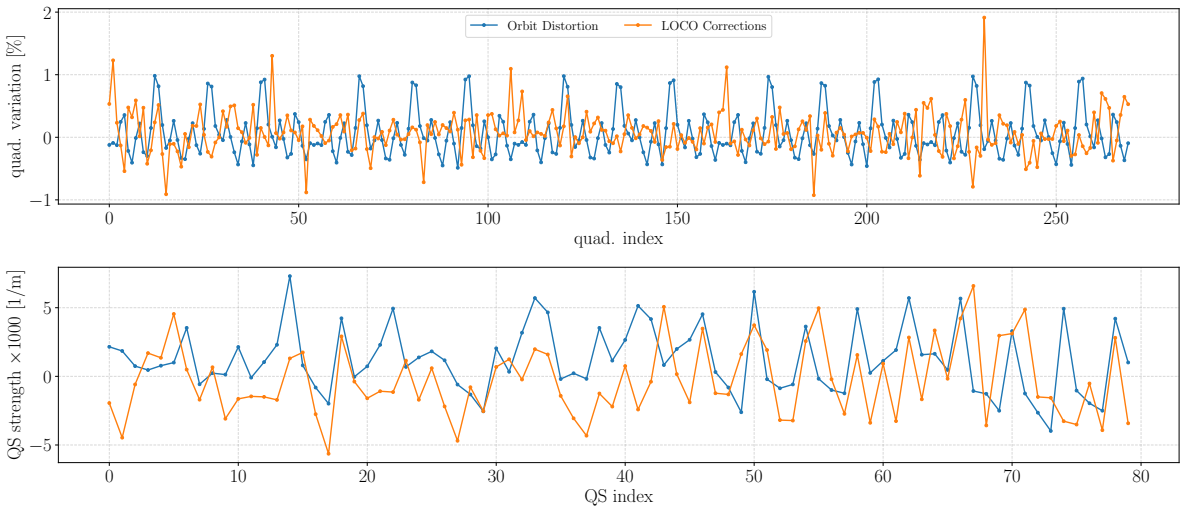

Figure 31 – Normal and skew quadrupoles variation for perturbed orbit model and the first LOCO calibrated model.

Table 13 – Optics errors before and after LOCO corrections applied on perturbed model.

Parameter (std)	before corr.	after corr.	Unit
$\Delta\beta_x/\beta_x$	8.6	1.8	%
$\Delta\beta_y/\beta_y$	3.0	1.5	%
$\Delta\eta_x$	3.3	1.6	mm
$\Delta\eta_y$	1.7	1.9	mm

For skew quadrupoles, the std variations are $2.4 \cdot 10^{-3}\,\mathrm{m}^{-1}$ for orbit perturbed model and $2.7 \cdot 10^{-3}\,\mathrm{m}^{-1}$ for LOCO corrections. When these corrections were applied in the perturbed model, the ORM errors were greatly reduced, the optics errors are reduced (except for η_y) but could not be eliminated, exactly as observed in the actual storage ring. The results of optics corrections on perturbed model is organized on Table 13.

From these results, it can be seen that, even with nominal gradients on the lattice, the linear optics perturbations generated by orbit distortions could be reduced but there is a limitation for this scheme of correction. The off-diagonal elements in ORM can be greatly reduced with skew quadrupoles, however since the vertical dispersion function could not be adjusted with LOCO fitting, it could not be corrected as well (in fact, the error was even increased).

The qualitative behavior of LOCO analysis using an ORM calculated from a model with the same residual orbit as measured in Sirius storage ring reproduces the behavior that is observed with measured ORM. Since in the real machine other errors also perturb the linear optics, it is expected that the minimum level of optics correction with a disturbed orbit is higher than the level obtained in this test.

This test raises a hypotheses for the incapacity of LOCO fitting to predict ac-

curately the storage ring optics. LOCO, as included in the method name, is a process to obtain the linear optics (regarding dipoles and quadrupoles). However, it was verified that the feed-down effects in quadrupoles and sextupoles (due to residual orbits) play an important role in the Sirius optics. An origin for this residual orbit might be the magnets misalignment in the storage ring, which was already confirmed with measurements performed by LNLS Alignment Group. Another explanation for these problems might be the incompatibility between the storage ring model and the actual storage ring regarding the elements longitudinal positions (specially from girders misalignment). In this case, the model would not accurately describe the storage ring.

The betatron function depends basically on the focusing strengths introduced by quadrupoles, while the dispersion function depends both on focusing and deflecting forces. Orbit distortions in quadrupoles introduce additional dipolar fields and in sextupoles extra focusing are introduced by the feed-down effect. With LOCO fitting, only the quadrupoles are varied to fit the linear optics. So, if the quadrupoles are used to compensate the gradients in sextupoles to fix the betatron function, the additional dipolar fields in quadrupole are changed as well, perturbing the dispersion function. On the other hand, if the quadrupoles are used to compensate the dipolar fields in quadrupoles and fix the dispersion function, the focusing strengths along the ring are changed and the betatron functions are perturbed. Therefore, in the presence of large orbit distortions, it is only possible to balance the correction of betatron function without perturbing the dispersion (or vice-versa), reaching a limited level of correction effectiveness.

Furthermore, this type of correction that uses quadrupoles to compensate for perturbations generated by orbit distortion is inadequate. The actual solution is to minimize the alignment problems that limit the residual orbit, so the orbit can be best corrected to the magnetic centers, reducing its effect on linear optics. After that, the LOCO corrections should fix these deviations and the optics errors should be corrected to a better level. A realignment campaign in Sirius is scheduled for January 2021. In this campaign, the devices longitudinal positions will also be measured and will be used to improve the storage ring model. After that, the machine will be re-commissioned and it is expected that LOCO analysis can be performed again to obtain a better level of correction for the storage ring linear optics.

Conclusions

In this work, the Linear Optics from Closed Orbit (LOCO) method was studied and implemented as a Python package for the Sirius storage ring. The code was submitted to several tests, using Orbit Response Matrices (ORM) obtained with simulations and measurements performed in the storage ring as well. The tests validated that the implemented method is robust and reliable. In these tests, the use of Levenberg-Marquardt (LM) minimization algorithm instead of Gauss-Newton (GN) proved to be the best choice to facilitate the singular values selection process required for fit parameters calculations. With this choice, only the last singular value, which is related to the well-known gain degeneracy in the vertical plane, should be removed. The LM algorithm has proved to be a great alternative for the time-consuming process of trial and error to determine the best set of singular values to be used in the fitting with GN algorithm. Another very important feature for the method was the constraints in quadrupole's strengths. Without constraints, the fitting converges to unrealistic solutions with large deviations on the gradients in quasi-degenerated quadrupoles (with similar signatures on ORM). Including constraints in step sizes, the solutions obtained reached the same quality of fitting with the advantage of providing much more realistic and feasible gradients variations.

LOCO method was applied to Sirius storage ring to correct the linear optics and coupling. The fit parameters error bars were obtained by measuring and fitting 10 ORMs. An individual quadrupole gradient in the lattice was intentionally changed, the ORM was measured and adjusted to prove that the method was able to accurately recover the localized variation. The ORM measured without optics and coupling corrections on storage ring were adjusted with LOCO with 20 different initial conditions on the quadrupoles gradients and all solutions obtained virtually converged to the same setting of quadrupoles, within the parameters error bars, indicating that the solution found provides the best ORM fit available. With two LOCO iterations, where the corrections were applied in quadrupoles trim-coils and skew quadrupoles at Sirius storage ring, another ORM was measured and adjusted with the method. The measured and nominal ORM difference was reduced from $\chi = 24.6\,\mu\text{m}$ to $2.1\,\mu\text{m}$. The errors of diagonal ORM blocks were reduced to about $1/9$ from its initial values and the off-diagonal blocks related to the coupling were greatly reduced to approximately $1/20$ of the initial errors. While the measured BPM accuracy was around $0.2\,\mu\text{m}$, the LOCO fitting level for the ORM in these iterations was about $0.9\,\mu\text{m}$. Although a sub-µm level of fitting is already satisfactory, this factor of 4 larger than the BPM accuracy indicates that there are still some systematic errors in the storage ring contributing to the ORM measurement that should be investigated. The dispersion functions had to be included in the fitting with a weight factor, otherwise,

Table 14 – Summary of storage ring parameters before and after LOCO corrections

Parameter	Before Corr.	After Corr.	Unit	Improvement Factor
$\Delta\beta_x/\beta_x$ (std)	12.8 ± 0.8	3.9 ± 0.8	%	3.3
$\Delta\beta_y/\beta_y$ (std)	10.4 ± 0.5	4.1 ± 0.5	%	2.5
$\Delta\eta_x$ (std)	10.2 ± 0.2	1.6 ± 0.2	mm	6.4
$\Delta\eta_y$ (std)	2.8 ± 0.3	1.9 ± 0.3	mm	1.5
H. Dynamic Aperture	7.6	8.3	mm	1.1
Injection Efficiency (mean)	20	68	%	3.4

the differences between measured and fitted horizontal dispersion were very large. The measured vertical dispersion function could not be explained with the calibrated model.

The final corrections applied in Sirius storage ring for normal gradients covered a range of $\pm 2\,\%$ and for skew gradients, the range was $\pm 5 \cdot 10^{-3}\,\mathrm{m}^{-1}$. Some independent measurements were performed to characterize the storage ring optics, coupling and performance before and after corrections. A summary of the obtained results is presented in Table 14.

Regarding the coupling, the measured global betatron coupling was reduced from $(0.78 \pm 0.04)\,\%$ to $(0.07 \pm 0.01)\,\%$, proving that LOCO is a robust tool to minimize both the off-diagonal ORM components and the global coupling as well. Initially, the calibrated LOCO model predicted the optics functions quite well compared to the measured values (except for the vertical dispersion). In the last fitting, after corrections application, this correspondence was not observed anymore.

The orbit contribution to the optics and coupling on Sirius storage ring was also studied. The measured residual orbit with respect to the BBA orbit was reproduced in the model. An ORM was calculated in this perturbed model and adjusted with LOCO. The model behavior, in this case, was similar to the obtained in the first iteration in the actual storage ring. The obtained optics errors caused by the orbit distortion in the model via the feed-down effect were on the same order compared to the errors measured in the storage ring without corrections. The horizontal and vertical dispersion function errors in both cases presented a substantial correlation. It was also necessary to include the dispersion function in the fitting with a weight factor to adjust the perturbed model dispersion. The vertical dispersion also could not be explained with LOCO model. The changes in quadrupole gradients and skew quadrupoles to fit the perturbed ORM were also on the order of magnitude of the corrections applied to the machine. All these results indicate that the residual orbit present in Sirius storage ring was perturbing considerably the optics and coupling by feed-down effect on quadrupoles and sextupoles. Moreover, the corrections calculated with LOCO and applied to the machine might be compensating for these errors generated by the orbit distortion. We concluded that the storage ring

status obtained reached the limit allowed for this kind of compensation. To improve even further the parameters, the feed-down effect must be minimized by reducing the residual orbit. At the time of writing, the orbit correction was limited by the correctors kicks thresholds ±330 µrad, which should be sufficient to correct the orbit at the BPMs in a better level, considering the magnet alignment errors tolerances. Measurements in the storage ring indicated that the actual errors were not meeting specifications and a realignment campaign was scheduled for January 2021. After that, it is expected that the residual orbit can be greatly reduced, consequently the related optics perturbations and, applying the LOCO method implemented in this work, the storage ring linear optics and performance might be further improved towards design values.

Future Activities

The Sirius commissioning is a work in progress and there are many subsequent activities related to this work. As already mentioned, the analysis and corrections of storage ring optics and coupling will be performed after the machine realignment. Once the diagnostic beamline is available, it will be possible to use beam size and emittance measurements as an independent verification for the effect of the corrections on the beam.

The Python code is planned to be generalized in the way of being able to run with any given lattice model, not only for the Sirius storage ring model. There is also an idea of implementing a graphical user interface in Python for the developed LOCO code, compatible with Sirius control system, then facilitating LOCO configuration setup, fitting, analysis, visualization of results and corrections application to the machine. This would make this LOCO Python version an user-friendly helpful tool for regular operations and machine studies on Sirius.

LOCO analysis can be performed with ORM measured with different conditions on Sirius storage ring. Different kicks amplitudes can be used in ORM measurements to check the non-linear contributions to the matrix. The effects of measuring ORMs with different energy deviations (off-energy orbits) may also be studied. The sextupoles setup can be varied to change the betatron tunes dependence with energy deviations (the chromaticity) in the ORM measurements and LOCO fittings.

Since the ORM measurement process takes about 25 minutes, the obtained data is subjected to drifts in the machine which may add errors to the ORM. Other facilities implemented a much faster and accurate ORM measurement, exciting the beam orbit with different known frequencies oscillations on corrector's kicks. Applying Fourier analysis on the data, the ORM elements can be obtained. With this method the ORM can be measured in a few minutes and LOCO analysis can be applied, then reducing the overall time required for Sirius optics studies.

ORM can be measured with different currents per bunch in the electron beam. The corresponding LOCO fitting for each measurement can provide information about the transverse impedance distribution around Sirius storage ring. Another branch of study is to benchmark LOCO results and corrections with other methods, for example, methods based on TbT data acquired from BPMs, such as PCA and Independent Component Analysis (ICA), which also fit optics functions in the lattice model and provides variations in fit parameters that can be applied as corrections on the machine.

A Feed-down Effect

The magnetic fields in a storage ring acting on the electron beam depends on the deviation between the beam position transverse position and the magnet magnetic center. If there this type of deviation is present, for example from magnets misalignment or beam orbit distortions, the so-called feed-down effect takes place. The largest the transverse deviations and the magnetic field strengths in a storage ring, the higher is the feed-down effect that, uncontrolled, spoils the beam dynamics. Since this effect should be mitigated as much as possible, this is one of the main reasons behind the very strict magnets alignment specifications in a storage ring, specially for 4^{th} generation machines. With transverse displacements, when the beam reaches a magnet which the main field order is n (for $n > 1$), the electrons will also be affected by all fields of order $n - 1$. The main contributions to the feed-down effect in a storage ring usually come from quadrupoles and sextupoles.

The effect for quadrupoles can be derived from the hamiltonian in Eq. (2.3), where it is assumed that the reference orbit are localized at $x = y = 0$.

$$H_0 = \frac{x'^2}{2} + \frac{y'^2}{2} + \left(K(s) - G^2(s)\right)\frac{x^2}{2} - K(s)\frac{y^2}{2} - G(s)x\delta. \tag{A.1}$$

If the reference orbit is transformed by $x(s) \to x(s) - x_0(s)$ and $y(s) \to y(s) - y_0(s)$, the corresponding change in the hamiltonian is

$$H_0 \to H_0 - K(s)\left(x_0 x - y_0 y\right) + \frac{K(s)}{2}\left(x_0^2 - y_0^2\right). \tag{A.2}$$

Thus, it can be seen that dipolar contributions both in horizontal and vertical planes appear, whose bending magnitudes are given by $K(s)x_0$ and $K(s)y_0$, respectively. Horizontal displacements in quadrupoles produce additional horizontal bending and the vertical displacement in quadrupoles creates vertical bending in the storage ring. The additional constant terms in the hamiltonian do not contribute to the equations of motion. The additional horizontal bending may perturb the horizontal dispersion function η_x and also distort the closed orbit. The vertical contribution creates a vertical dispersion η_y, which might increase the vertical beam emittance, decrease the light source brightness and disturb the closed orbit as well.

The other important contribution comes from sextupoles. The non-linear transverse hamiltonian in the presence of sextupoles is given by [47]:

$$H_S = H_0 + \frac{S(s)}{6}\left(x^3 - 3xy^2\right), \tag{A.3}$$

where $S(s)$ is the sextupolar function around the storage ring.

Applying the coordinate transformation $x(s) \rightarrow x(s) - x_0(s)$, one can calculate that the related change in the hamiltonian is

$$H_S \rightarrow H_S - \frac{S(s)x_0}{2}\left(x^2 - y^2\right) + \frac{S(s)x_0^2}{2}x - \frac{S(s)x_0^3}{6}. \tag{A.4}$$

Therefore, horizontal displacements in sextupoles produce additional focusing forces, changing the focusing function by $K(s) \rightarrow K(s) - S(s)x_0(s)$ and perturbing the storage ring linear optics, i.e., betatron and dispersion functions. These deviations in sextupoles also create dipolar contributions but its strength depends on $x_0^2(s)$, so this is a second order effect. Again, the additional constant term does not affect the dynamics.

With the transformation in the vertical plane $y(s) \rightarrow y(s) - y_0(s)$, the change in the non-linear hamiltonian is

$$H_S \rightarrow H_S + S(s)y_0xy - \frac{S(s)y_0^2}{2}x, \tag{A.5}$$

which allows us to conclude that vertical deviations in sextupole produce coupled terms that add skew gradients in the storage ring, introducing perturbations in the lattice related to the transverse betatron coupling. Once again, there is a dipolar perturbation, which depends on $y_0^2(s)$ and is typically less important.

B Singular Value Decomposition - SVD

Let $\mathbf{M}$ be a real $m \times n$ matrix. The Singular Value Decomposition (SVD) is a factorization that generalizes the eigenvalues decomposition and it states that every matrix can be decomposed in the following form:

$$\mathbf{M} = \mathbf{U}\Sigma\mathbf{V}^{\mathsf{T}}, \tag{B.1}$$

where $\mathbf{U}$ is a $m \times m$ matrix, $\mathbf{V}$ is a $n \times n$ matrix and Σ is a $m \times n$ positive-definite rectangular diagonal matrix. $\mathbf{U}$ and $\mathbf{V}$ are orthogonal matrices:

$$\mathbf{U}\mathbf{U}^{\mathsf{T}} = \mathbf{U}^{\mathsf{T}}\mathbf{U} = \mathbf{I}_m \tag{B.2}$$

$$\mathbf{V}\mathbf{V}^{\mathsf{T}} = \mathbf{V}^{\mathsf{T}}\mathbf{V} = \mathbf{I}_n. \tag{B.3}$$

Manipulating the equation (B.1) and using the matrices properties we obtain

$$\mathbf{M}\mathbf{M}^{\mathsf{T}} = \mathbf{U}\Sigma^2\mathbf{U}^{\mathsf{T}} \tag{B.4}$$

$$\mathbf{M}^{\mathsf{T}}\mathbf{M} = \mathbf{V}\Sigma^2\mathbf{V}^{\mathsf{T}}. \tag{B.5}$$

From this, we observe that the diagonal elements of Σ^2 are eigenvalues of $\mathbf{M}\mathbf{M}^{\mathsf{T}}$ and $\mathbf{M}^{\mathsf{T}}\mathbf{M}$, which are called row-wise correlation and column-wise correlation matrices, respectively. Since $\mathbf{U}^{\mathsf{T}} = \mathbf{U}^{-1}$ and $\mathbf{V}^{\mathsf{T}} = \mathbf{V}^{-1}$, the columns of $\mathbf{U}$ are the eigenvectors of $\mathbf{M}\mathbf{M}^{\mathsf{T}}$ and the columns of $\mathbf{V}$ are the eigenvectors of $\mathbf{M}^{\mathsf{T}}\mathbf{M}$.

The diagonal elements $\sigma_i := \Sigma_{ii} \geq 0$ are called singular values. The SVD of a matrix is unique up to permutations and a default choice is to arrange the decomposition in such a way that the singular values are sorted in descending order, $\sigma_i \geq \sigma_j$ for $i < j$. The number of non-zero singular values is exactly the rank of matrix $\mathbf{M}$. Thus, the SVD of a rank deficient matrix will result in zero or numerically very small singular values.

A common procedure to avoid degeneracies in the calculations is the singular values selection. This can be done by setting explicitly the unwanted singular values to zero. This can be done in a more insightful way by defining a minimum threshold Δ and setting to zero the singular values that satisfy $\dfrac{\sigma_i}{\max(\sigma_i)} < \Delta$. This methods eliminates the less important directions defined by the columns of $\mathbf{U}$ and $\mathbf{V}$ as compared to the direction with higher singular values.

Since Σ is a diagonal matrix, its inverse is obtained simply by $\Sigma_{ii}^{-1} = 1/\sigma_i$. For the case that $\sigma_i = 0$, one can define $\Sigma_{ii}^{-1} = 0$. Hence, the matrix $n \times m$

$$\mathbf{M}^{-1} = \mathbf{V}\Sigma^{-1}\mathbf{U}^{\mathsf{T}}, \tag{B.6}$$

is a pseudo-inverse of $\mathbf{M}$ as can be checked by

$$\mathbf{M}^{-1}\mathbf{M} = \left(\mathbf{V}\Sigma^{-1}\mathbf{U}^{\mathsf{T}}\right)\left(\mathbf{U}\Sigma\mathbf{V}^{\mathsf{T}}\right) = \mathbf{I}_n \tag{B.7}$$

$$\mathbf{M}\mathbf{M}^{-1} = \left(\mathbf{U}\Sigma\mathbf{V}^{\mathsf{T}}\right)\left(\mathbf{V}\Sigma^{-1}\mathbf{U}^{\mathsf{T}}\right) = \mathbf{I}_m. \tag{B.8}$$

The matrix $\mathbf{M}^{-1}$ is also known as Moore-Penrose pseudo-inverse [51].

A useful version of SVD is the so-called "economy SVD". Let $r = \min(m, n)$, then one can observe that $\Sigma_{ij} = 0$ for $i > r$ or $j > r$. In this way, all these zero rows or columns in the rectangular $m \times n$ matrix Σ can be removed to build a smaller square matrix $\hat{\Sigma}$ with dimension $r \times r$. If $m > n$, then $r = n$ and this allows for reducing the dimension of $\mathbf{U}$ as well, obtaining a rectangular $m \times r$ matrix $\hat{\mathbf{U}}$ and the matrix $\mathbf{V}$ is unchanged. If $m < n$, then $r = m$ and the transpose case occurs, so $\mathbf{V}$ can be reduced to a $r \times n$ matrix and $\mathbf{U}$ is unchanged. Let's assume $m > n$, which is the case for the matrices in this work. In this situation, the new matrix $\hat{\mathbf{U}}$ is semi-orthogonal, i.e., $\hat{\mathbf{U}}^{\mathsf{T}}\hat{\mathbf{U}} = \mathbf{I}_r$ but $\hat{\mathbf{U}}\hat{\mathbf{U}}^{\mathsf{T}} \neq \mathbf{I}_m$ in general. The economy SVD is very interesting for numerical purposes, since it is common that $m \gg n$ or $m \ll n$, then using only the minimum useful data contained in the SVD matrices is very computationally beneficial.

The SVD pseudo-inversion is a powerful tool to solve generic linear systems of equations given by

$$\mathbf{A}\vec{x} = \vec{b}, \tag{B.9}$$

where $\mathbf{A}$ is a $m \times n$ matrix, $\vec{x}$ a $n \times 1$ column vector and $\vec{b}$ a $m \times 1$ column vector. The case that $m = n$ may be exactly solvable, if $\det(\mathbf{A}) \neq 0$ the exact solution is obtained by normal inversion. Other two cases that may not have an exact solution occur:

- Underdeterminated: $m < n$ and the system has infinitely many solutions, given a generic vector $\vec{b}$. The system does not have enough information given by the elements of $\vec{b}$ to obtain the exact unknowns $\vec{x}$. With the pseudo-inversion it is possible to obtain a solution $\vec{x}_s$ to the linear system such that $|\vec{x}_s|^2 = \sum_{i=1}^{n} x_{s,i}^2$ is minimized. This is called the minimum-norm solution.

- Overdeterminated: $m > n$ and the system has no solution, given a generic vector $\vec{b}$. The system has more equations than unknowns, so the system is overconstrained and it is not possible to satisfy exactly and simultaneously all the equations. In this case, with the pseudo-inversion it is obtained an approximate solution $\vec{x}_s$ that minimizes the difference $|\mathbf{A}\vec{x}_s - \vec{b}|$. This is called the least squares solution.

The idea in LOCO algorithm is applying linear approximations to convert a least squared minimization problem in a linear algebra problem, obtaining a linear system of equations. In this process there is much more data points than unkowns to be determined, thus LOCO algorithm is characterized as an overdetermined problem.

C BPMs and Correctors Gains

The starting point to obtain LOCO jacobian matrix for the BPMs gains and rolls is the linear transformation:

$$\vec{u}_{i,\text{real}} = \mathbf{R}^{\text{BPM}}(\alpha_i)\,\mathbf{G}_i^{\text{BPM}}\vec{u}_{i,\text{meas.}}. \tag{C.1}$$

If the orbit vector is viewed as a function $\vec{u}_i = \vec{u}_i(\theta_j, \alpha_i, g_{i,x}, g_{i,y})$, the ORM is $\vec{M}_{ij} = \dfrac{\partial \vec{u}_i}{\partial \theta_j}$. The vector is just a notation to use $\vec{u}_i = (x_i, y_i)$ and $\vec{M}_{ij} = \left(M_{ij}^x, M_{ij}^y\right)$. Moreover, the matrices $\mathbf{R}(\alpha_i)$ and $\mathbf{G}_i^{\text{BPM}}$ satisfies

$$\frac{\partial \mathbf{R}^{\text{BPM}}(\alpha_i)}{\partial \theta_j} = \frac{\partial \mathbf{G}_i^{\text{BPM}}}{\partial \theta_j} = 0.$$

Thus it is possible to obtain from (C.1) that

$$\vec{M}_{ij}^{\text{real}} = \mathbf{R}^{\text{BPM}}(\alpha_i)\,\mathbf{G}_i^{\text{BPM}}\vec{M}_{ij}^{\text{meas.}}. \tag{C.2}$$

The transformation represented in equation (C.2) must be applied in the measured ORM as LOCO algorithm updates the values of $(\alpha_i, g_{x,i}, g_{y,i})$.

The residue vector is defined as $\vec{V} = \text{vec}\left(\mathbf{M}^{\text{meas.}} - \mathbf{M}^{\text{model}}\right)$. Since $\mathbf{M}^{\text{measured}}$ must be corrected by the transformation that includes BPM gains and rolls, the new residue vector is elements are

$$V_k^{\text{real}} = \mathbf{R}^{\text{BPM}}(\alpha_i)\,\mathbf{G}_i^{\text{BPM}}M_{ij}^{\text{meas.}} - \mathbf{M}_{ij}^{\text{model}}, \tag{C.3}$$

where the index k is obtained from i and j by the vectorization.

To calculate LOCO jacobian matrix one needs to calculate the derivatives of $\vec{V}^{\text{real}}$ relative to the fit parameters $(\alpha_i, g_{x,i}, g_{y,i})$, which are assumed to be independent parameters, obtaining:

$$J_{kl}^{\text{BPMroll}} = \frac{\partial V_k^{\text{real}}}{\partial \alpha_l} = \delta_{il}\frac{\mathrm{d}\mathbf{R}^{\text{BPM}}(\alpha_i)}{\mathrm{d}\alpha_l}\mathbf{G}_i^{\text{BPM}}M_{ij}^{\text{meas.}}, \tag{C.4}$$

$$J_{kl}^{\text{BPMgain}} = \frac{\partial V_k^{\text{real}}}{\partial g_{l,u}} = \delta_{il}\mathbf{R}^{\text{BPM}}(\alpha_i)\,M_{ij}^{\text{meas.}}, \tag{C.5}$$

where δ_{il} is the Kronecker delta and

$$\frac{\mathrm{d}\mathbf{R}^{\text{BPM}}(\alpha_i)}{\mathrm{d}\alpha_i} = \begin{bmatrix} -\sin\alpha_i & \cos\alpha_i \\ -\cos\alpha_i & -\sin\alpha_i \end{bmatrix}.$$

Due to the sorting used in the ORM that the horizontal measurements are in the upper blocks and the vertical measurements are in the lower blocks, the transformation matrices of gains and rolls are reorganized as

$$\mathbf{R}_{\alpha}^{\mathrm{BPM}} = \begin{bmatrix} \mathbf{C}^{\alpha} & \mathbf{S}^{\alpha} \\ -\mathbf{S}^{\alpha} & \mathbf{C}^{\alpha} \end{bmatrix},$$
$$\frac{\mathrm{d}\mathbf{R}_{\alpha}^{\mathrm{BPM}}}{\mathrm{d}\alpha} = \begin{bmatrix} -\mathbf{S}^{\alpha} & \mathbf{C}^{\alpha} \\ -\mathbf{C}^{\alpha} & -\mathbf{S}^{\alpha} \end{bmatrix},$$
$$\mathbf{G}^{\mathrm{BPM}} = \begin{bmatrix} \mathbf{G}^{x} & \mathbf{G}^{y} \\ \mathbf{G}^{x} & \mathbf{G}^{y} \end{bmatrix},$$

formed with diagonal sub-matrices $C_{ii}^{\alpha} = \cos\alpha_i$, $S_{ii}^{\alpha} = \sin\alpha_i$, $G_{ii}^{x} = g_{i,x}$, $G_{ii}^{y} = g_{i,y}$. The transformation in this form is very useful to be applied directly in the measured ORM and to calculate the jacobian matrix elements:

$$\mathbf{M}^{\mathrm{real}} = \mathbf{R}_{\alpha}^{\mathrm{BPM}}\mathbf{G}^{\mathrm{BPM}}\mathbf{M}^{\mathrm{meas.}}, \tag{C.6}$$
$$J_{kl}^{\mathrm{BPMroll}} = \delta_{il}\left(\frac{\mathrm{d}\mathbf{R}_{\alpha}^{\mathrm{BPM}}}{\mathrm{d}\alpha}\mathbf{G}^{\mathrm{BPM}}\mathbf{M}^{\mathrm{meas.}}\right)_{ij}, \tag{C.7}$$
$$J_{kl}^{\mathrm{BPMgain}} = \delta_{il}\left(\mathbf{R}_{\alpha}^{\mathrm{BPM}}\mathbf{M}^{\mathrm{meas.}}\right)_{ij}, \tag{C.8}$$

the index i is related to BPM index (rows of ORM) and it is used to be compared with the index l of the jacobian matrix columns. Again, i and j are converted by vectorization to obtain the index k.

For the steering magnets gain the analysis is straightforward. The transformation is

$$\theta_{j,\mathrm{applied}}^{u} = g_{j,u}^{\mathrm{corr}}\theta_{j,\mathrm{real}}^{u}, \tag{C.9}$$

where the "applied" sub-index is the equivalent for the "measured" in BPMs.

This transformation can be also cast in a matrix form, with diagonal gain matrices. However, since the kicks are in the denominator of the ORM with $M_{ij} = \dfrac{\Delta u_i}{\Delta\theta_j}$, the correct way to implement the corrector gain transformation in the ORM is by its inverse

$$\mathbf{M}^{\mathrm{real}} = \mathbf{G}_{\mathrm{corr}}^{-1}\mathbf{M}^{\mathrm{meas.}}. \tag{C.10}$$

Since the steering magnet gain was defined by equation (C.9), the diagonal elements of $\mathbf{G}_{\mathrm{corr}}$ are $G_{ii}^{\mathrm{corr}} = 1/g_i$ so the inverse elements are g_i. This is convenient to obtain the jacobian matrix elements in a linear form, in the same manner that was obtained for the BPMs gains:

$$J_{kl}^{\mathrm{corr-gain}} = \delta_{jl}M_{ij}^{\mathrm{meas.}}. \tag{C.11}$$

The index j is related to correctors index (columns of ORM) and it is used to be compared with the index l of the jacobian matrix columns. Once again, i and j are

converted by vectorization to obtain the index k. Since the correctors is sorted column-wise in the ORM, the related gains blocks are organized as $\mathbf{G}_{\text{corr}} = \begin{bmatrix} \mathbf{G}^x & \mathbf{G}^x \\ \mathbf{G}^y & \mathbf{G}^y \end{bmatrix}$.

If the corrector gain was defined alternatively as $\theta^u_{j,\text{real}} = g^{\text{corr}}_{j,u}\theta^u_{j,\text{applied}}$, the jacobian matrix would contain non-linear elements like $-1/g_i^2$, obtained from the derivative of $1/g_i$.

The final transformation, containing the BPMs and correctors gains and also the BPM roll is

$$\mathbf{M}^{\text{real}} = \mathbf{R}^{\text{BPM}}_{\alpha}\mathbf{G}^{\text{BPM}}\mathbf{M}^{\text{meas.}}\mathbf{G}^{-1}_{\text{corr}}. \tag{C.12}$$

In each iteration of LOCO algorithm, the gains and rolls parameters are updated and the transformation described in equation (C.12) must be applied.

The matrix multiplication order is important, since the ORM dimension is $2\text{N}_{\text{BPM}} \times \text{N}_{\text{corr}}$, the BPM-related matrices dimensions are $2\text{N}_{\text{BPM}} \times 2\text{N}_{\text{BPM}}$ and the correctors-related matrix dimension is $\text{N}_{\text{corr}} \times \text{N}_{\text{corr}}$.

D Code Validation

In order to check the reliability of the implemented LOCO code and also to develop an intuition on the method behavior for the Sirius storage ring (before actual applications), a series of tests were performed. In this appendix these tests and the results obtained are reported.

D.1 Detecting Distributed Errors

The first test to check the implemented code consists in perturbing the simulated storage ring model, obtain the corresponding ORM and then trying to determine the input errors from the fit parameters with LOCO analysis.

It is important to point out that this test should work properly if the errors are included in the elements that are used as fit parameters in LOCO method. For example, if gradient errors are added in the sextupoles but only quadrupoles strengths are fitted, the quadrupoles will be changed to best fit the ORM. Thus, even if the χ^2 is reduced, the final quadrupoles variations will not match the planted gradient errors in the sextupoles, since these elements are in different positions around the ring, with different phase advances. In this case, the fitted values must be interpreted only as the gradient changes in quadrupoles that best explain the perturbed ORM. Clearly this type of compensation should reach a limit of fitting effectiveness. Therefore, whenever it is possible, the most appropriated approach is to identify and then to minimize the errors sources not covered by LOCO and, only after that, apply LOCO analysis to obtain appropriated corrections.

A hundred sets of errors were generated following a random normal distribution with 3σ cutoff. These errors were included in the simulated model and then the corresponding hundred ORMs were calculated. LOCO analysis were performed for these ORMs, fitting all the parameters described in Table 3. The std σ used in the normal distribution to generate random errors for each parameter are presented in Table 15.

Table 15 – Random errors included in the simulated model (3σ cutoff).

Parameter	σ of distribution	Unit
Normal quadrupole gradient	0.1	%
H. and V. BPM gain	2.5	%
H. and V. Corrector gain	5.0	%
Skew quadrupole gradient	10^{-3}	m^{-1}
BPM roll angle	10	mrad

Table 16 – Differences (normalized by σ) between planted errors and fitted variations obtained from LOCO analysis for 100 sets of random errors.

Parameter	std difference/σ	peak-to-valley difference/σ
Normal quadrupole gradient	$1.1 \cdot 10^{-2}$	$5.9 \cdot 10^{-2}$
H. BPM gain	$2.8 \cdot 10^{-4}$	$1.6 \cdot 10^{-3}$
H. Corrector gain	$1.0 \cdot 10^{-4}$	$5.5 \cdot 10^{-4}$
V. BPM gain	$7.8 \cdot 10^{-4}$	$3.2 \cdot 10^{-3}$
V. Corrector gain	$7.9 \cdot 10^{-4}$	$3.2 \cdot 10^{-3}$
Skew quadrupole gradient	$4.9 \cdot 10^{-3}$	$2.3 \cdot 10^{-2}$
BPM roll angle	$4.7 \cdot 10^{-3}$	$2.2 \cdot 10^{-2}$

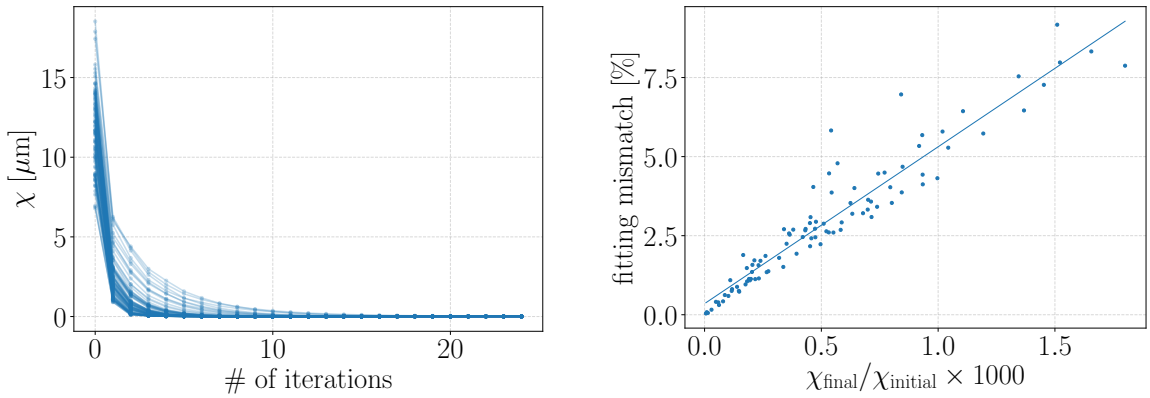

(a) χ convergence.

(b) Fitting mismatch versus fitting level.

Figure 32 – Fitting over 100 random ORM obtained from the simulated model.

The goal of this test is to compare the fitted variations determined from LOCO with the random errors included in the model. The statistics related to the differences between these two sets of values are presented in Table 16, where the difference was normalized by the std σ used to generate the random errors.

From the results in Table 16 it can be seen that for the normal quadrupoles, skew quadrupoles and BPM roll angles, target and obtained errors normalized by σ agrees to within a few percent. For the gains of horizontal correctors and BPM, the difference is a few parts in ten thousand and for the vertical ones, it is a few parts in a thousand. The dispersion function was included in the fitting to break the horizontal gains degeneracy, which explains the fact that the gains determination for the horizontal plane was more efficient than the obtained in the vertical plane. The average initial χ for these 100 sets of random errors was 11.6 µm and after the fitting, the average final χ was 6.2 nm. Such level of fitting is only possible because in these tests the ORM was obtained without any noise in the data and the process is not subjected to measurement errors. For real measurements, it is desired to achieve a final value for χ that is close to the BPM accuracy, which with the current technology is typically from hundreds of nanometers to a few micrometers.

In Figure 32a the convergence of χ for the 100 fittings is presented. The maximum number of iterations was limited to 25. It can be seen that at about 15 iterations χ already converged for all the 100 cases. Figure 32b shows the relation between the fitting level, represented by the ratio $\chi_{\text{final}}/\chi_{\text{initial}}$, and the fitting mismatch for each realization, obtained by $\sqrt{\sum_p d_p^2}$, where d_p is the difference between target and fitted errors normalized by σ for the parameter p covering all the 7 fit parameters used in LOCO runs. The mismatch in the fitting grows linearly with the fitting level, with a proportionality factor of about 50. The code would be unreliable if the fitting level was good but the corresponding mismatch was large. Such cases were not observed in the 100 random realizations.

D.2 Detecting Localized Errors

Detecting single errors is very useful to identify, in a more specific way, malfunctioning elements or a problematic region in the storage ring. A functional diagnostic tool that provides this localized detection can spare a considerable amount of time in the investigation of problems that are degrading the machine performance, thus being a helpful tool for the commissioning stage and regular operation of a synchrotron light source as well, since installation and maintenance intervention occurs several times during the machine lifetime. The goal of the tests reported in the present subsection is to check LOCO ability to identify localized errors on quadrupoles, BPMs and correctors.

D.2.1 Single Gradient

Suppose that amongst random gradient errors in quadrupoles, there is a single quadrupole with a large deviation from its nominal value. Single quadrupole errors are not naturally expected, since magnetic measurements are performed before the assembly in storage ring to guarantee that mechanical and magnetic properties meet the specifications for all magnets. However, after the magnets assembly some kind of problem in a specific magnet coils or in its power supply may appear and lead to localized errors.

The following error distribution was generated and applied in Sirius storage ring model: gaussian random errors in gradient strengths with std $\sigma = 0.25\,\%$ and $2.0\,\%$ of error in the 215^{th} quadrupole. Errors in others parameters were not included. An ORM was calculated with this perturbed model and it was used as input for LOCO analysis, including all fit parameters. The results for variations in quadrupoles fitted by LOCO compared to the target errors are in Figure 33.

From Figure 33 it can be seen that the input errors were accurately determined, including the single large gradient error. The maximum difference between fitted and target error for quadrupoles was $1 \cdot 10^{-8}$. The final value of χ in this fitting was very low, around $1 \cdot 10^{-6}\,\mu\text{m}$. The variations on the remaining fit were in a much lower level, the

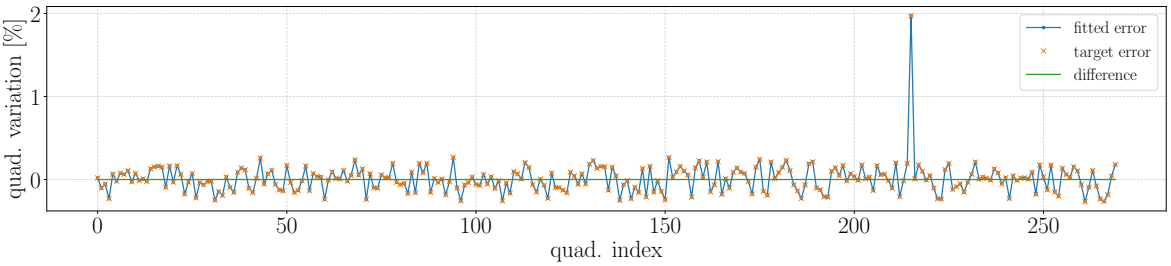

Figure 33 – Fitted and target quadrupoles variations, including a higher error of 2% in the 215$^{\text{th}}$ quadrupole.

maximum variation of BPM gains and correctors was $3 \cdot 10^{-6}$ and for skew quadrupoles strengths $1 \cdot 10^{-16}\,\text{m}^{-1}$, on the order of computer numeric precision.

It is clear that this level of error determination is only possible for tests in the simulated model, when the goal ORM was obtained without noise and measurement errors. Nevertheless, in the limit that these practical limitations are set as low as possible in real measurements, it would still be possible to identify single errors with reasonable accuracy.

D.2.2 Single Gain

The same tests were performed with BPMs and correctors gains. Such type of error in gains may be associated with malfunctioning in BPMs antennas, electrical interference or software issues. For correctors the outliers in gains may indicate problems in the magnet coils or in its power supplies. For BPMs, the problems are typically easier to detect since they can be identified directly from unrealistic position measurements. For correctors, the effect on the beam produced by localized problems may be more subtle to identify directly. Measuring the ORM and performing LOCO analysis is usually a good indirect procedure to detect the aforementioned errors.

Gaussian random errors with std $\sigma = 10\,\%$ were applied both for horizontal and vertical gains. BPM roll angle errors were included following a gaussian random distribution with std $\sigma = 1\,\text{mrad}$. The corresponding gains for 7$^{\text{th}}$ BPM, CH and CV were increased by a 1.5 factor. This means that the nominal ORM, after applying the random gains errors, had the 7$^{\text{th}}$ and 167$^{\text{th}}$ rows (for the 7$^{\text{th}}$ BPM) and 7$^{\text{th}}$ and 127$^{\text{th}}$ columns (for the 7$^{\text{th}}$ CH and CV) multiplied by 1.5. This altered ORM were set as the goal matrix for LOCO fitting, where all fit parameters were included again. The fitting results for this test are shown in Figure 34.

Once again, the input errors were determined precisely and the larger planted gains were identified, both for BPM and correctors. The maximum difference between fitted and target error for horizontal gains (BPM and CH) was 0.2 % and for vertical gains (BPM and

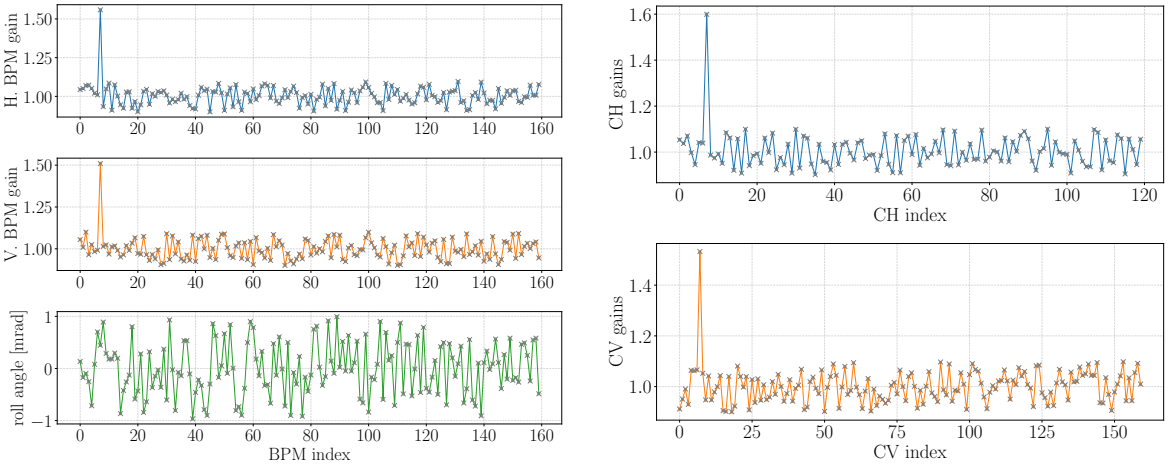

(a) BPM gains and roll angles.

(b) Correctors gains.

Figure 34 – Fitted values for BPM gains, roll errors and correctors (CH and CV) gains, where the 7$^{\text{th}}$ BPM, CH and CV gains are greater by a 1.5 factor. Gray $\times$ represents the target errors.

CV) was 0.1 %. The other parameters were changed again in a lower level, the maximum variation for quadrupoles was $2 \cdot 10^{-6}$ and for skew quadrupoles $4 \cdot 10^{-9}\,\mathrm{m}^{-1}$.

E LOCO pseudo-algorithm

The pseudo-algorithm for LOCO fitting is presented in this appendix. For the Python implementation, the GitHub Repository [59] should be consulted.

Algorithm 1: LOCO pseudo-algorithm

Result: Fitted model, χ^2 at each step
Get LOCOInput: measured ORM, $\Delta\theta_x$, $\Delta\theta_y$, Δf_{rf}, ν_x, ν_y and σ_{BPM}.
Define LOCOConfig: fit parameters, minimization method, singular values selection, constraints, weights, n_{steps}, χ^2_{min}, χ^2_{step}, initial λ, λ_{min}, λ_{max}.
Change model tunes to match the measured values.
Obtain initial model ORM.
Calculate or load LOCO jacobian matrix.
Perform SVD and singular values filtering on jacobian matrix to obtain its pseudo-inverse.
Calculate initial reference residue vector $\vec{V}_0$ and χ^2_0.
$n \leftarrow 0$
while $n \leq n_{\text{steps}}$ **do**
  With $\vec{V}_0$, calculate parameters variations $\Delta\vec{P}$.
  Apply $\Delta\vec{P}$ to the model and obtain new ORM.
  Calculate new residue vector $\vec{V}$ and χ^2.
  if $\chi^2 > \chi^2_0$ *or* $\chi^2 < \chi^2_{\text{min}}$ **then**
    if $\chi^2 > \chi^2_{\text{min}}$ *and LM method* **then**
      LM Fail $\leftarrow$ LM Loop().
      if *LM Fail* **then**
        Stop
      end
    else
      Stop
    end
  else
    if $\chi^2_0 - \chi^2 < \chi^2_{\text{step}}$ **then**
      Stop
    else
      Update parameters $\vec{P} \leftarrow \vec{P} + \Delta\vec{P}$.
      Update model.
      Update references $\vec{V}_0 \leftarrow \vec{V}$ and $\chi^2_0 \leftarrow \chi^2$.
      if *LM method* **then**
        Decrease λ and recalculate the jacobian pseudo-inverse
      end
    end
  end
  $n \leftarrow n + 1$
end
Save output.

The additional loop for the case of Levenberg-Marquardt minimization algorithm usage in LOCO fitting is presented in the Algorithm 2 below.

Algorithm 2: LM Loop pseudo-algorithm

```
Result: LM Fail
LM Fail ← True
while λ > λ_min and λ < λ_max do
    Increase λ.
    Recalculate the jacobian pseudo-inverse.
    Recalculate parameters variations ΔP⃗.
    Apply ΔP⃗ to the model and obtain new ORM.
    Calculate new residue vector V⃗ and χ².
    if χ² < χ₀² then
        Update parameters P⃗ ← P⃗ + ΔP⃗
        Update model
        Update references V⃗₀ ← V⃗ and χ₀² ← χ²
        LM Fail ← False.
        Stop.
    end
end
```

F Integral of Beta in Quadrupoles

The tune shift caused by a gradient error distribution $k(s)$ is, from Eq. (2.36):

$$\Delta\nu_u = \frac{1}{4\pi}\oint \beta_u(s)k(s)\mathrm{d}s. \tag{F.1}$$

A gradient error distributed along a quadrupole can be modeled as

$$k(s) = \begin{cases} \Delta\mathrm{K} \ \text{ for } s \in [0, L], \\ 0 \ \text{ for } s \notin [0, L] \end{cases}, \tag{F.2}$$

where L is the quadrupole length. The tune shift in this case is

$$\Delta\nu_u = \frac{\Delta\mathrm{K}}{4\pi}\int_0^L \beta_u(s)\mathrm{d}s. \tag{F.3}$$

If a quadrupole strength is intentionally changed by the amount ΔK and the corresponding tune shift is measured with the beam, the integral of beta function in the quadrupole can be calculated:

$$\int_0^L \beta_u(s)\mathrm{d}s = 4\pi\frac{\Delta\nu_u}{\Delta\mathrm{K}}. \tag{F.4}$$

Typically it is convenient to use the integrate quadrupole strength ΔKL, in this way, the quantity that is calculated is the integral of beta function along the quadrupole normalized by the quadrupole length:

$$\frac{1}{L}\int_0^L \beta_u(s)\mathrm{d}s = 4\pi\frac{\Delta\nu_u}{\Delta\mathrm{KL}}. \tag{F.5}$$

In the approximated case when the beta function is considered constant along the quadrupole, we obtain that $\beta_u(s_q) = 4\pi\dfrac{\Delta\nu_u}{\Delta\mathrm{KL}}$, where s_q is the varied quadrupole longitudinal position.

It is important to notice that considering $\Delta\mathrm{KL} > 0$ increases the focusing forces in the horizontal plane, thus necessarily decreases the focusing forces in the vertical plane. With this strength change we will obtain $\Delta\nu_x > 0$ and $\Delta\nu_y < 0$. Since the beta function is always positive, in this case the ΔKL sign must be negative for the vertical betatron function calculation to cancel the $\Delta\nu_y$ sign.

The tune-shift approach is used for the measurement of the integral of betatron functions in the quadrupoles in a storage ring.

To calculate the same quantities in the storage ring model there are a numerical and an analytical approach. The numerical approach basically reproduces the measurement procedure performed in the real storage ring. It may include non-linear effects due

to the gradient variation but it also has the disadvantage of computing time. For every quadrupole in the storage ring, the Twiss functions after the gradient variation must be calculated, depending on the time required to calculate the storage ring Twiss functions and on the number of quadrupoles in the lattice, the calculation time may be an inconvenient for a practical use of this numerical approach.

It is also possible to calculate an analytical expression for the beta integral along the quadrupole. Let the Twiss parameters be $(\beta_0, \alpha_0, \gamma_0)$ at the quadrupole entrance. The beta function in a position s along the quadrupole can be propagated as

$$\beta(s) = \beta_0 C^2(s) - 2\alpha_0 C(s)S(s) + \gamma_0 S^2(s), \tag{F.6}$$

where the functions $C(s)$ and $S(s)$ are

$$C(s) = \begin{cases} \cos(\sqrt{K}s) \text{ for } K > 0, \\ \cosh(\sqrt{|K|}s) \text{ for } K < 0, \end{cases}$$

$$S(s) = \begin{cases} \frac{1}{\sqrt{K}} \sin(\sqrt{K}s) \text{ for } K > 0, \\ \frac{1}{\sqrt{|K|}} \sinh(\sqrt{|K|}s) \text{ for } K < 0. \end{cases}$$

Therefore, calculating the $\beta(s)$ integral, we obtain the following results.

For $K > 0$:

$$\begin{aligned} \int_0^L \beta(s)\mathrm{d}s = & \frac{L}{2}\left(\beta_0 + \gamma_0/K\right) \\ & + \frac{\sin\left(2\sqrt{K}L\right)}{4\sqrt{K}}\left(\beta_0 - \gamma_0/K\right) \\ & - \frac{\alpha_0}{K}\sin^2\left(\sqrt{K}\right). \end{aligned}$$

For $K < 0$:

$$\begin{aligned} \int_0^L \beta(s)\mathrm{d}s = & \frac{L}{2}\left(\beta_0 + \gamma_0/K\right) \\ & + \frac{\sinh\left(2\sqrt{|K|}L\right)}{4\sqrt{|K|}}\left(\beta_0 - \gamma_0/K\right) \\ & - \frac{\alpha_0}{|K|L}\sinh^2\left(\sqrt{|K|}\right). \end{aligned}$$

It is worth to mention again that $K > 0$ for the x plane corresponds to $K < 0$ for the y plane.

With the analytical approach, the Twiss parameters calculation is required only once to obtain $(\beta_0, \alpha_0, \gamma_0)$ at the quadrupoles entrances, and with the quadrupole strength K and length L, the integrals are calculated with the above presented formulae.

Bibliography

[1] Huang, X. *Beam-based Correction and Optimization for Accelerators* (CRC Press, 2019). URL https://books.google.com.br/books?id=rzKkwwEACAAJ. 8, 19, 28, 53, 61, 88

[2] LNLS. Wiki-Sirius. https://wiki-sirius.lnls.br (2020). 8, 22, 23, 25

[3] Deniau, G. R. L., Grote, H. & Schmidt, F. MAD-X: User's reference manual version. http://madx.web.cern.ch/madx/webguide/manual.html (2019). 8, 32

[4] de Sá, F. H. *Estudo de Impedâncias e Instabilidades Coletivas aplicado ao Sirius. Study of Impedances and Collective Instabilities applied to Sirius.* Ph.D. thesis (2018). URL http://www.repositorio.unicamp.br/handle/REPOSIP/331867. 10, 26

[5] LNLS. LNLS official webpage: about LNLS. https://www.lnls.cnpem.br/the-lnls/about/ (2020). 14

[6] CNPEM. CNPEM official webpage. https://cnpem.br/cnpem/ (2020). 14

[7] Liu, L., Neuenschwander, R. T. & Rodrigues, A. R. D. Synchrotron radiation sources in Brazil. *Philosophical Transactions of the Royal Society A: Mathematical, Physical and Engineering Sciences* **377**, 20180235 (2019). URL https://royalsocietypublishing.org/doi/abs/10.1098/rsta.2018.0235. https://royalsocietypublishing.org/doi/pdf/10.1098/rsta.2018.0235. 14, 21

[8] Jackson, J. D. *Classical electrodynamics* (Wiley, New York, NY, 1999), 3rd ed. edn. URL http://cdsweb.cern.ch/record/490457. 15

[9] Huang, Z. Brightness and Coherence of Synchrotron Radiation and FELs. In *Proceedings of IPAC 2013*, vol. 02-A06 of *MOYCB101*, 16–20 (IEEE, Shanghai, China, 2013). URL http://epaper.kek.jp/IPAC2013/papers/moycb101.pdf. 16, 66

[10] Eriksson, M., van der Veen, J. F. & Quitmann, C. Diffraction-limited storage rings – a window to the science of tomorrow. *Journal of Synchrotron Radiation* **21**, 837–842 (2014). URL https://doi.org/10.1107/S1600577514019286. 17

[11] Liu, L. & Westfahl Jr., H. Towards Diffraction Limited Storage Ring Based Light Sources. In *8th International Particle Accelerator Conference*, TUXA1 (2017). 17

[12] Eriksson, M. *et al.* Commissioning of the MAX IV Light Source. In *7th International Particle Accelerator Conference*, MOYAA01 (2016). 17

[13] LNLS. Wiki-Sirius: Beam Position Calculation. `https://wiki-sirius.lnls.br/mediawiki/index.php/DIG:Beam_Position_Calculation` (2020). 19

[14] Einfeld, D. & Plesko, M. A modified qba optics for low emittance storage rings. *Nuclear Instruments and Methods in Physics Research Section A: Accelerators, Spectrometers, Detectors and Associated Equipment* **335**, 402 – 416 (1993). URL `http://www.sciencedirect.com/science/article/pii/016890029391224B`. 21

[15] Hettel, R. Challenges in the design of diffraction-limited storage rings. *IPAC 2014: Proceedings of the 5th International Particle Accelerator Conference* 7–11 (2014). 21

[16] Benvenuti, C. A new pumping approach for the large electron positron collider (lep). *Nuclear Instruments and Methods in Physics Research* **205**, 391 – 401 (1983). URL `http://www.sciencedirect.com/science/article/pii/0167508783900030`. 21

[17] Neuenschwander, R., Liu, L., S.R.Marques, A.R.D.Rodrigues & Seraphim, R. Engineering challenges of future light sources (2015). 21

[18] Tavares, P. F., Leemann, S. C., Sjöström, M. & Andersson, Å. The MAXIV storage ring project. *Journal of Synchrotron Radiation* **21**, 862–877 (2014). URL `https://doi.org/10.1107/S1600577514011503`. 21

[19] Liu, L., Milas, N., Mukai, A. H. C., Resende, X. R. & de Sá, F. H. The sirius project. *Journal of Synchrotron Radiation* **21**, 904–911 (2014). URL `https://onlinelibrary.wiley.com/doi/abs/10.1107/S1600577514011928`. 21, 22

[20] Raimondi, P. The ESRF Low-emittance Upgrade. In *7th International Particle Accelerator Conference*, WEXA01 (2016). 21

[21] Liu, L., Neuenschwander, R. T. & Rodrigues, A. R. D. Synchrotron radiation sources in brazil. *Philosophical Transactions of the Royal Society A: Mathematical, Physical and Engineering Sciences* **377**, 20180235 (2019). URL `https://royalsocietypublishing.org/doi/abs/10.1098/rsta.2018.0235`. 21, 23

[22] Craievich, A. F. Synchrotron radiation in brazil. past, present and future. *Radiation Physics and Chemistry* **167**, 108253 (2020). URL `http://www.sciencedirect.com/science/article/pii/S0969806X18311733`. Special issue dedicated to the 14th International Symposium on Radiation Physics. 21

[23] de Sá, F. H., Liu, L., Resende, X. R. & Rodrigues, A. R. D. A New Booster Synchrotron for the Sirius Project. In *Proceedings of IPAC 2014*, vol. 02-T12 of *WEPRO009*, 1959–1962 (IEEE, Dresden, Germany, 2014). 22

[24] Liu, L., de Sá, F. H., Resende, X. R. & Rodrigues, A. R. D. Injection Dynamics for Sirius Using a Nonlinear Kicker. In *Proceedings of IPAC 2016*, vol. 05-D02 of *THPMR011*, 3406–3408 (IEEE, Busan, Korea, 2016). 22, 91

[25] Liu, L., Resende, X. & de Sá, F. A New Optics for Sirius. In *7th International Particle Accelerator Conference*, THPMR013 (2016). 23

[26] Sajaev, V. & Borland, M. Commissioning Simulations for the APS Upgrade Lattice. In *6th International Particle Accelerator Conference*, MOPMA010 (2015). 26

[27] Liuzzo, S., Carmignani, N., Farvacque, L. & Nash, B. Lattice Tuning and Error Setting in Accelerator Toolbox. In *8th International Particle Accelerator Conference*, WEPIK061 (2017). 26

[28] Ghasem, H., Apollonio, M., Bartolini, R., Kennedy, J. & Martin, I. Early Commissioning Simulation of the Diamond Storage Ring Upgrade. In *10th International Particle Accelerator Conference*, TUPGW076 (2019). 26

[29] Sajaev, V. Commissioning simulations for the argonne advanced photon source upgrade lattice. *Phys. Rev. Accel. Beams* **22**, 040102 (2019). URL `https://link.aps.org/doi/10.1103/PhysRevAccelBeams.22.040102`. 26

[30] Hellert, T., Amstutz, P., Steier, C. & Venturini, M. Toolkit for simulated commissioning of storage-ring light sources and application to the advanced light source upgrade accumulator. *Phys. Rev. Accel. Beams* **22**, 100702 (2019). 26

[31] Alves, M., Liu, L. & de Sá, F. Simulation of Sirius Booster Commissioning. In *10th International Particle Accelerator Conference*, WEPTS105 (2019). 26

[32] Safranek, J. & Lee, M. Calibration of the x-ray ring quadrupoles, bpms, and orbit correctors using the measured orbit response matrix. *AIP Conference Proceedings* **315**, 128–136 (1994). URL `https://aip.scitation.org/doi/abs/10.1063/1.46761`. 28

[33] Safranek, J. Experimental determination of linear optics including quadrupole rotations. In *Proceedings Particle Accelerator Conference*, vol. 5, 2817–2819 vol.5 (1995). 28

[34] Safranek, J. Experimental determination of storage ring optics using orbit response measurements. *Nuclear Instruments and Methods in Physics Research Section A: Accelerators, Spectrometers, Detectors and Associated Equipment* **388**, 27 – 36 (1997). URL `http://www.sciencedirect.com/science/article/pii/S0168900297003094`. 28, 48, 62, 71, 74, 76

[35] Lee, M. Accelerator simulation using computers. In *SLAC-PUB-5701A* (1992). 28

[36] Corbett, W. J., Lee, M. J. & Ziemann, V. A fast model calibration procedure for storage rings. In *Proceedings of International Conference on Particle Accelerators*, 108–110 vol.1 (1993). 28

[37] Safranek, J. Linear optics from closed orbits (LOCO) – an introduction. *ICFA - Beam Dynamics Newsletter* **44** (2007). 28, 29

[38] Robin, D., Safranek, J., Portmann, G. & Nishimura, H. Model calibration and symmetry restoration of the advanced light source (1996). 28

[39] Safranek, J., Portmann, G. & Terebilo, A. Matlab-based LOCO. 1184–1186 (2002). 28

[40] Portmann, G., Safranek, J. & Huand, X. Matlab based LOCO. *ICFA - Beam Dynamics Newsletter* **44** (2007). 28

[41] Terebilo, A. Accelerator modeling with matlab accelerator toolbox. vol. 4, 3203 – 3205 vol.4 (2001). 29

[42] Resende, X., Farias, R., Liu, L., Plotegher, M. & Tavares, P. Analysis of the LNLS Storage Ring Optics Using LOCO. In *Particle Accelerator Conference (PAC 09)*, TH6PFP012 (2010). 29

[43] Huang, X., Safranek, J. & Portmann, G. LOCO with constraints and improved fitting technique. *ICFA - Beam Dynamics Newsletter* **44** (2007). 29, 53, 66

[44] JACoW. Joint accelerator conferences website. `https://jacow.org/` (2020). 29

[45] Leemann, S., Sjöström, M. & Andersson, A. First optics and beam dynamics studies on the max iv 3 gev storage ring. *Nuclear Instruments and Methods in Physics Research Section A: Accelerators, Spectrometers, Detectors and Associated Equipment* **883** (2017). 29

[46] Sands, M. *The physics of electron storage rings: an introduction* (Stanford Linear Accelerator Center Stanford, 1970). 31

[47] Wiedemann, H. *Particle accelerator physics* (Springer, 2007). 31, 43, 46, 102

[48] Courant, E. D. & Snyder, H. S. Theory of the alternating-gradient synchrotron. *Annals of physics* **3**, 1–48 (1958). URL `http://www.sciencedirect.com/science/article/pii/0003491658900125`. 34, 63

[49] Nadolski, L. S. LOCO fitting challenges and results for SOLEIL. *ICFA - Beam Dynamics Newsletter* **44** (2007). 48, 59

[50] Spencer, M. LOCO at the Australian synchrotron. *ICFA - Beam Dynamics Newsletter* **44** (2007). 48

[51] Press, W. H., Teukolsky, S. A., Vetterling, W. T. & Flannery, B. P. *Numerical Recipes 3rd Edition: The Art of Scientific Computing* (Cambridge University Press, USA, 2007), 3 edn. 52, 53, 105

[52] Levenberg, K. A method for the solution of certain non-linear problems in least squares. *Quart. Appl. Math* **2**, 64–168 (1944). 53

[53] Marquardt, D. An algorithm for least-squares estimation of nonlinear parameters. *Journal of the Society for Industrial and Applied Mathematics* **11(2)**, 431–441 (1963). 53

[54] LNLS Accelerator Physics Group. Pymodels, GitHub repository. `https://github.com/lnls-fac/pymodels` (2020). 63

[55] Nishimura, H. TRACY: A tool for accelerator design and analysis (1988). 63

[56] LNLS Accelerator Physics Group. Trackcpp, GitHub repository. `https://github.com/lnls-fac/trackcpp` (2020). 63

[57] LNLS Accelerator Physics Group. Pyaccel, GitHub repository. `https://github.com/lnls-fac/pyaccel` (2020). 63

[58] NumPy. NumPy webpage. `https://numpy.org/` (2020). 63

[59] Alves, M. B. LOCO for Sirius, GitHub repository. `https://github.com/lnls-fac/apsuite/apsuite/loco` (2020). 64, 114

[60] Alves, M. B. Beta measurement script for Sirius, GitHub repository. `https://github.com/lnls-fac/apsuite/blob/master/apsuite/commissioning_scripts/measure_beta.py` (2020). 86

[61] LNLS. Wiki-Sirius: Injection with Nonlinear Kicker. `https://wiki-sirius.lnls.br/mediawiki/index.php/Machine:Injection_System#Injection_with_Nonlinear_Kicker_.28InjNLKckr.29` (2020). 91